Hazards at the production of titanium alloys in the electric arc furnace

Slokar Benić, Ljerka; Ivec, Ivan; Čačić, Katarina

Source / Izvornik: **Machines, Technologies, Materials, 2023, 17, 113 - 116**

Journal article, Published version
Rad u časopisu, Objavljena verzija rada (izdavačev PDF)

Permanent link / Trajna poveznica: https://urn.nsk.hr/urn:nbn:hr:115:609674

International journal
for science, technics and
innovations for the industry

MACHINES TECHNOLOGIES MATERIALS

YEAR XVII Issue 3 / 2023 ISSN PRINT 1313-0226
ISSN WEB 1314-507X

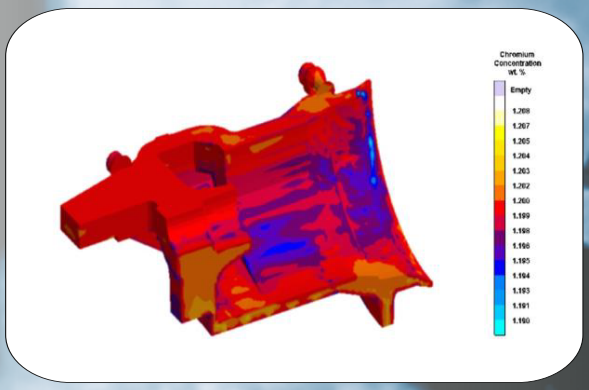

Published by
Scientific technical
Union of Mechanical Engineering

MACHINES. TECHNOLOGIES. MATERIALS

INTERNATIONAL SCIENTIFIC JOURNAL

ISSN PRINT 1313-0226, ISSN WEB 1314-507X, YEAR XVII, ISSUE 3 / 2023

Scientific and technical union of mechanical engineering
108 R. S. Rakovski str., Sofia, Bulgaria
www.stumejournals.com, office@stumejournals.com

C O N T E N T S

MACHINES

TECHNOLOGIES

MATERIALS

Exergy analysis of steam turbine from ultra-supercritical power plant

Mrzljak Vedran[1], Marjanović Danijel[1], Prpić-Oršić Jasna[1], Glažar Vladimir[1]
[1]Faculty of Engineering, University of Rijeka, Vukovarska 58, 51000 Rijeka, Croatia
E-mail: vedran.mrzljak@riteh.hr, danijel_marjanovic@hotmail.com, jasna.prpic-orsic@riteh.hr, vladimir.glazar@riteh.hr

Abstract: *In this paper is presented an exergy analysis of steam turbine (along with analysis of each cylinder and cylinder part) from ultra-supercritical power plant. Observation of all the cylinders shows that IPC (Intermediate Pressure Cylinder) is the dominant mechanical power producer (it produces mechanical power equal to 394.44 MW), it has the lowest exergy loss and simultaneously the highest exergy efficiency (equal to 95.84%). HPC (High Pressure Cylinder) has a very high exergy efficiency equal to 92.37% what confirms that ultra-supercritical steam process is very beneficial for the HPC (and whole steam turbine) operation. LPC (Low Pressure Cylinder) is a dissymmetrical dual flow cylinder, so both of its parts (left and right part) did not produce the same mechanical power, did not have the same exergy loss, but their exergy efficiency is very similar and in a range of entire LPC exergy efficiency (around 82.5%). Whole observed steam turbine produces mechanical power equal to 928.03 MW, has exergy loss equal to 93.45 MW and has exergy efficiency equal to 90.85%. The exergy efficiency of the whole analyzed steam turbine is much higher in comparison to other steam turbines from various conventional power plants.*

KEYWORDS*: EXERGY ANALYSIS, STEAM TURBINE, TURBINE CYLINDERS, ULTRA-SUPERCRITICAL PROCESS*

1. Introduction

Steam power plants are nowadays the dominant producers of the mechanical power which is directly converted to electrical energy by using electric generators [1, 2]. In such power plants the dominant mechanical power producers are complex steam turbines, which are usually composed of several cylinders connected to the same shaft [3, 4]. Low power steam turbines can be composed of one cylinder, but such turbines produce mechanical power sufficient for the auxiliary purposes only [5, 6].

Conventional and nuclear steam power plants improve its operation each day with an aim to increase efficiency and reduce losses [7, 8]. A new type of steam power plants are built more and more each day around the world – these are supercritical and ultra-supercritical steam power plants [9, 10]. This kind of steam power plants has maximum steam pressures notably higher than critical ones [11]. According to already published literature, supercritical and ultra-supercritical steam power plants have various benefits in comparison to conventional or nuclear steam power plants [12]. The most important benefit is fuel savings in steam generator due to the high pressure process, but the interesting question arises – are such high pressures beneficial to other components of these power plants?

In this paper is performed an exergy analysis of one randomly selected steam turbine from ultra-supercritical power plant. It is analyzed how high pressure steam influences whole turbine, turbine cylinders and parts of dissymmetrical cylinders. It is presented which cylinder of observed turbine show the best performance (the highest efficiency and the lowest losses). Finally, the overall performance of analyzed steam turbine is compared to steam turbines from conventional power plants.

2. Description and operation details of the analyzed steam turbine

General scheme of the analyzed steam turbine from ultra-supercritical power plant is presented in Fig. 1.

The observed steam turbine has three cylinders (HPC = High Pressure Cylinder, IPC = Intermediate Pressure Cylinder, LPC = Low Pressure Cylinder) connected to the same shaft which drives an electric generator. Steam produced in steam generator is firstly delivered to the HPC which has three steam extractions. After HPC, steam is delivered to reheater (mounted inside steam generator) which increases steam temperature before its expansion in IPC. IPC has two steam extractions and after IPC, steam is delivered to the LPC. Both HPC and IPC are single flow turbine cylinders. On the steam pipeline between IPC and the LPC is mounted one more steam extraction (operating point 8a, Fig. 1). LPC is a dissymmetrical dual flow turbine cylinder which means that through each LPC part (left and right) are extracted different steam mass flow rates. Dissymmetrical dual flow turbine cylinders should be carefully designed and maintained due to axial force imbalance [13]. Left LPC part has two, while right LPC part has only one steam extraction. Entire steam mass flow rate extracted through all presented steam extractions (from the turbine cylinders and from the steam pipeline) is delivered to condensation/feedwater heating system which increases condensate/water temperature before its return to the steam generator [14]. After expansion in all turbine cylinders, remaining steam mass flow rate at the LPC outlet (operating point 12, Fig. 1) is delivered to the main steam condenser for condensation [15].

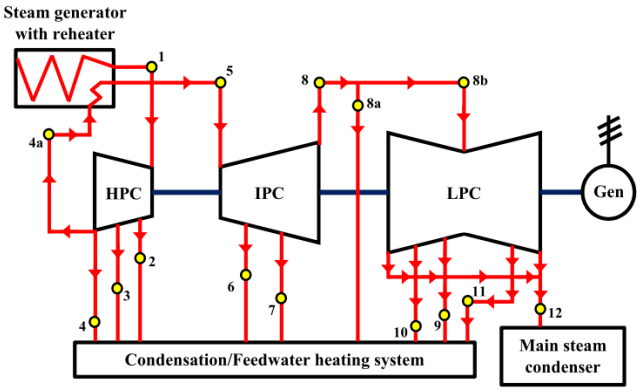

Fig. 1. *General scheme of the analyzed steam turbine from ultra-supercritical power plant along with operating points required for the exergy analysis*

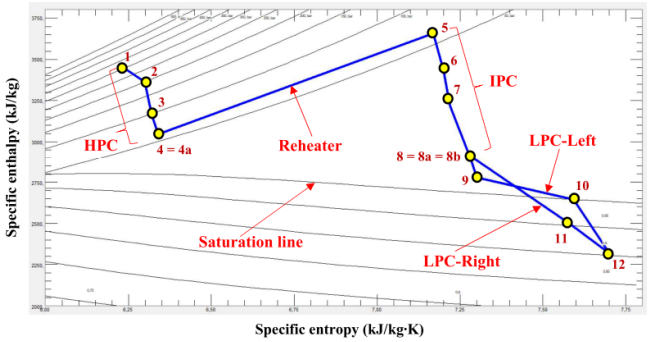

Fig. 2. *Steam expansion process in h-s diagram throughout all the cylinders of the analyzed turbine from ultra-supercritical power plant*

In Fig. 2 is presented steam expansion process in *h-s* diagram through all the cylinders of the observed steam turbine. The main characteristic of the steam turbine from ultra-supercritical power plant is that at the HPC entrance (operating point 1, Fig. 1 and Fig. 2) steam pressure is notably higher than the pressure at fluid critical point (for water, critical point pressure is equal to 220.64 bar). The steam reheating process is clearly visible in Fig. 2 between operating points 4 and 5 – increase in steam temperature results with simultaneous increase in steam specific enthalpy and specific

entropy. Steam expansion process in Fig. 2 is presented separately for the left and right LPC part – a clear difference in the expansion process between left and right LPC part is another confirmation of the fact that the LPC is dissymmetrical dual flow turbine cylinder.

3. Equations for the steam turbine exergy analysis

3.1. Overall exergy equations and balances

Regardless of the analyzed component, component part or the entire system, in the exergy analysis exists several equations and balances which should always be satisfied [16]. These equations and balances will be presented in this paper part. The main exergy balance equation, according to [17] is:

$$\dot{X}_{\text{in}} + P_{\text{in}} + \sum \dot{E}x_{\text{in}} - \dot{X}_{\text{out}} - P_{\text{out}} - \sum \dot{E}x_{\text{out}} - \dot{E}x_{\text{L}} = 0, \quad (1)$$

where P is mechanical power, index in is related to the inlet (input), index out is related to outlet (output) and index L is related to exergy loss. Exergy transfer by heat at the temperature T ($\dot{X}$) is defined according to [18] by the equation:

$$\dot{X} = \sum(1 - \frac{T_0}{T}) \cdot \dot{Q}, \quad (2)$$

where $\dot{Q}$ is an energy transfer by heat and index 0 is related to the ambient state. The last undefined variable from the exergy balance equation is a total exergy flow of any fluid stream ($\dot{E}x$) which definition can be found in [19]:

$$\dot{E}x = \dot{m} \cdot \varepsilon, \quad (3)$$

where $\dot{m}$ is a fluid mass flow rate and ε is specific exergy of any fluid stream, which is defined by an equation [20]:

$$\varepsilon = (h - h_0) - T_0 \cdot (s - s_0), \quad (4)$$

where h is fluid specific enthalpy and s is fluid specific entropy. If there is no fluid leakage, always valid mass flow rate balance is:

$$\sum \dot{m}_{\text{in}} = \sum \dot{m}_{\text{out}}. \quad (5)$$

Overall and general definition of the exergy efficiency is [19]:

$$\eta_{\text{ex}} = \frac{\text{cumulative exergy output}}{\text{cumulative exergy input}}. \quad (6)$$

3.2. Equations for the exergy analysis of observed turbine

Equations for the exergy analysis of the observed steam turbine, its cylinders and cylinder parts are composed according to recommendations from the literature [21] and by using operating points from Fig. 1. Equations for the produced mechanical power calculation of each cylinder, cylinder part and whole analyzed turbine are presented in Table 1.

Table 1. *Equations for the produced mechanical power calculation in each cylinder, cylinder part and whole observed turbine*

Component	Produced mechanical power	Eq.
HPC	$P_{\text{HPC}} = \dot{m}_1 \cdot (h_1 - h_2) + (\dot{m}_1 - \dot{m}_2) \cdot (h_2 - h_3) + (\dot{m}_1 - \dot{m}_2 - \dot{m}_3) \cdot (h_3 - h_4)$	(7)
IPC	$P_{\text{IPC}} = \dot{m}_5 \cdot (h_5 - h_6) + (\dot{m}_5 - \dot{m}_6) \cdot (h_6 - h_7) + (\dot{m}_5 - \dot{m}_6 - \dot{m}_7) \cdot (h_7 - h_8)$	(8)
LPC-Left	$P_{\text{LPC,Left}} = \frac{\dot{m}_{8b}}{2} \cdot (h_8 - h_9) + \left(\frac{\dot{m}_{8b}}{2} - \dot{m}_9\right) \cdot (h_9 - h_{10}) + \left(\frac{\dot{m}_{8b}}{2} - \dot{m}_9 - \dot{m}_{10}\right) \cdot (h_{10} - h_{12})$	(9)
LPC-Right	$P_{\text{LPC,Right}} = \frac{\dot{m}_{8b}}{2} \cdot (h_8 - h_{11}) + \left(\frac{\dot{m}_{8b}}{2} - \dot{m}_{11}\right) \cdot (h_{11} - h_{12})$	(10)
LPC-Cumul.	$P_{\text{LPC,Cumulative}} = P_{\text{LPC,Left}} + P_{\text{LPC,Right}}$	(11)
WT	$P_{\text{WT}} = P_{\text{HPC}} + P_{\text{IPC}} + P_{\text{LPC,Cumulative}}$	(12)

A total exergy flow of any fluid stream (in each operating point from Fig. 1) is calculated by using Eq. 3. Equations for the exergy loss calculation are presented in Table 2, while equations for the exergy efficiency calculation are presented in Table 3 (for each cylinder, cylinder part and whole analyzed turbine).

Table 2. *Equations for the exergy loss calculation in each cylinder, cylinder part and whole observed turbine*

Component	Exergy loss	Eq.
HPC	$\dot{E}x_{\text{L,HPC}} = \dot{E}x_1 - \dot{E}x_2 - \dot{E}x_3 - \dot{E}x_4 - \dot{E}x_{4a} - P_{\text{HPC}}$	(13)
IPC	$\dot{E}x_{\text{L,IPC}} = \dot{E}x_5 - \dot{E}x_6 - \dot{E}x_7 - \dot{E}x_8 - P_{\text{IPC}}$	(14)
LPC-Left	$\dot{E}x_{\text{L,LPC,Left}} = \frac{\dot{E}x_{8b}}{2} - \dot{E}x_9 - \dot{E}x_{10} - \left(\frac{\dot{m}_{8b}}{2} - \dot{m}_9 - \dot{m}_{10}\right) \cdot \varepsilon_{12} - P_{\text{LPC,Left}}$	(15)
LPC-Right	$\dot{E}x_{\text{L,LPC,Right}} = \frac{\dot{E}x_{8b}}{2} - \dot{E}x_{11} - \left(\frac{\dot{m}_{8b}}{2} - \dot{m}_{11}\right) \cdot \varepsilon_{12} - P_{\text{LPC,Right}}$	(16)
LPC-Cumul.	$\dot{E}x_{\text{L,LPC,Cumulative}} = \dot{E}x_{\text{L,LPC,Left}} + \dot{E}x_{\text{L,LPC,Right}}$	(17)
WT	$\dot{E}x_{\text{L,WT}} = \dot{E}x_{\text{L,HPC}} + \dot{E}x_{\text{L,IPC}} + \dot{E}x_{\text{L,LPC,Cumulative}}$	(18)

Table 3. *Equations for the exergy efficiency calculation in each cylinder, cylinder part and whole observed turbine*

Component	Exergy efficiency	Eq.
HPC	$\eta_{\text{ex,HPC}} = \frac{P_{\text{HPC}}}{\dot{E}x_{\text{L,HPC}} + P_{\text{HPC}}}$	(19)
IPC	$\eta_{\text{ex,IPC}} = \frac{P_{\text{IPC}}}{\dot{E}x_{\text{L,IPC}} + P_{\text{IPC}}}$	(20)
LPC-Left	$\eta_{\text{ex,LPC,Left}} = \frac{P_{\text{LPC,Left}}}{\dot{E}x_{\text{L,LPC,Left}} + P_{\text{LPC,Left}}}$	(21)
LPC-Right	$\eta_{\text{ex,LPC,Right}} = \frac{P_{\text{LPC,Right}}}{\dot{E}x_{\text{L,LPC,Right}} + P_{\text{LPC,Right}}}$	(22)
LPC-Cumul.	$\eta_{\text{ex,LPC,Cumulative}} = \frac{P_{\text{LPC,Cumul.}}}{\dot{E}x_{\text{L,LPC,Cumul.}} + P_{\text{LPC,Cumul.}}}$	(23)
WT	$\eta_{\text{ex,WT}} = \frac{P_{\text{WT}}}{\dot{E}x_{\text{L,WT}} + P_{\text{WT}}}$	(24)

4. Steam operating parameters required for the observed turbine exergy analysis

Steam operating parameters in each operating point from Fig. 1 are found in [22] and presented in Table 4. It should be highlighted that in [22] are not found all steam operating parameters, missing ones which are required for the exergy analysis of observed turbine and its cylinders are additionally calculated by using NIST-Refprop 9.0 software [23].

Steam specific exergies (according to Eq. 4) are dependable on the state of the ambient in which analyzed turbine and its cylinders operate. Therefore, in each exergy analysis should be defined base ambient state. According to the recommendations from the literature [24], in this analysis the base ambient state is defined with ambient pressure of 1 bar and ambient temperature of 25 °C.

Table 4. *Steam parameters in each operating point of the analyzed turbine*

O. P.*	Temperature (°C)	Pressure (bar)	Mass flow rate (kg/s)	Specific enthalpy (kJ/kg)	Specific entropy (kJ/kg·K)	Specific exergy (kJ/kg)**
1	600.00	300.00	822.36	3446.7	6.2373	1591.60
2	539.00	200.00	122.00	3363.4	6.2988	1489.90
3	424.00	100.00	78.26	3169.1	6.3188	1289.80
4	351.00	60.00	43.18	3046.7	6.3402	1161.00
4a	351.00	60.00	578.92	3046.7	6.3402	1161.00
5	600.00	60.00	578.92	3658.7	7.1693	1525.80
6	488.00	30.00	35.88	3430.3	7.2007	1287.90
7	384.00	15.00	60.57	3221.8	7.2189	1074.10
8	225.00	4.00	482.47	2913.0	7.2795	747.14
8a	225.00	4.00	17.78	2913.0	7.2795	747.14
8b	225.00	4.00	464.69	2913.0	7.2795	747.14
9	154.00	2.00	34.18	2777.3	7.3004	605.29
10	81.35	0.50	11.65	2645.3	7.5932	385.93
11	60.06	0.20	18.18	2499.9	7.5800	244.49
12	28.96	0.04	400.68	2320.0	7.7000	28.84

* O. P. = Operating Point (refers to Fig. 1)

** Specific exergies in each operating point are calculated for the base ambient state

5. Results of the analysis and discussion

Produced mechanical power in each cylinder, each LPC part and in the whole analyzed turbine is presented in Fig. 3.

The dominant mechanical power producer in the analyzed steam turbine is IPC, which produces 394.44 MW of mechanical power. HPC produces 280.73 MW of mechanical power, while the whole LPC produces the lowest mechanical power of all cylinders equal to 252.87 MW. LPC is dissymmetrical dual flow turbine cylinder which means that both turbine parts (due to different extracted steam mass flow rates in each part) will not produce the same mechanical power. Due to more extracted steam through two steam extractions in the left part of the LPC, it produces lower mechanical power in comparison to right LPC part (118.36 MW in comparison to 134.51 MW). In dissymmetrical dual flow turbine cylinders a special attention should be placed on the axial force balancing [13].

According to steam operating parameters presented in Table 4, whole analyzed steam turbine produces mechanical power equal to 928.03 MW, which is completely used for the electric generator drive (if all auxiliary mechanical power consumers are neglected because they use relatively small amounts of cumulatively produced mechanical power).

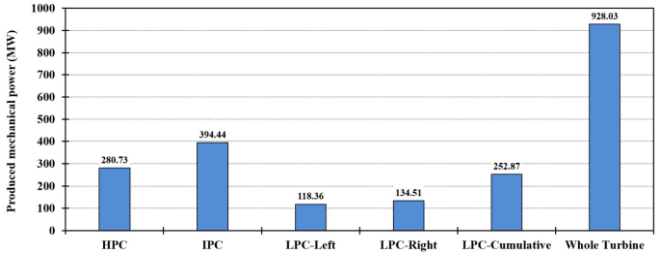

Fig. 3. *Produced mechanical power in all cylinders, cylinder parts and whole analyzed turbine from ultra-supercritical power plant*

The total exergy flow of each fluid stream (in each operating point from Fig. 1) is presented in Fig. 4.

From Fig. 4 is obvious that the highest total exergy flows occur at each turbine cylinder inlet and outlet. The only exception from this conclusion can be seen at the LPC outlet where the steam temperature is very close to the temperature of the ambient, what results with the small total exergy flow (operating point 12). Between operating points 4a and 5 total exergy flow increases due to steam reheating process. As expected and considering all operating points, the highest total exergy flow occurs at the HPC inlet (equal to 1308.87 MW).

If considering all steam extractions from all turbine cylinders, it can be seen that the highest total exergy flows are in the HPC, following by IPC, while the lowest total exergy flows are observed in LPC. Total exergy flows in steam extractions define arrangement of the condensation/feedwater heating system – heaters which operate with the highest temperatures must get steam from HPC and heaters which operate with the lowest temperatures must get steam from LPC.

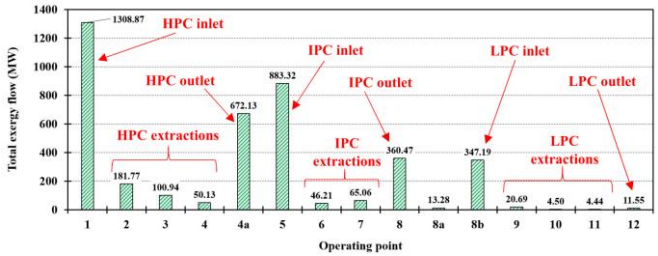

Fig. 4. *Total exergy flows in each operating point related to the observed steam turbine from ultra-supercritical power plant*

Observation of turbine cylinders shows that IPC is not only the dominant mechanical power producer in this turbine, Fig. 3, it also has the lowest exergy loss (equal to 17.14 MW), much lower in comparison to other turbine cylinders, Fig. 5.

As expected, the highest exergy loss can be found in LPC (approximately three times higher than the exergy loss of IPC and more than two times higher than the exergy loss of the HPC). Also, each LPC part (left and right) has higher exergy loss than IPC or HPC by itself, while LPC right part has a higher exergy loss in comparison to left LPC part (28.46 MW in comparison to 24.67 MW). Such high exergy loss in LPC (and each LPC part) can be expected because LPC operates with steam of much lower pressure and temperature in comparison to steam which expands in other turbine cylinders.

Whole observed steam turbine from ultra-supercritical power plant has cumulative exergy loss equal to 93.45 MW, Fig. 5.

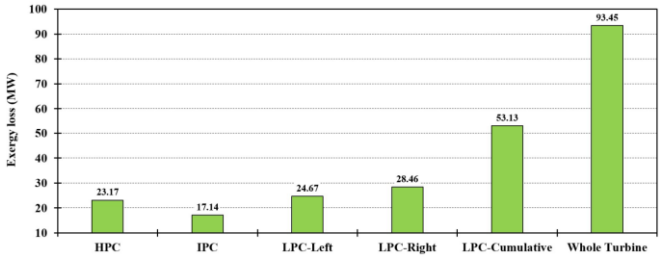

Fig. 5. *Exergy loss in all cylinders, cylinder parts and whole analyzed turbine from ultra-supercritical power plant*

The exergy efficiency of each cylinder, each LPC part and whole observed turbine is presented in Fig. 6.

IPC of the observed steam turbine is not only the dominant mechanical power producer, it also has the lowest exergy loss and the highest exergy efficiency (equal to 95.84%) in comparison to all other cylinders, Fig. 5 and Fig. 6. HPC has a very high exergy efficiency equal to 92.37%, regardless of the highest steam pressures and temperatures which occur in that cylinder. Very high exergy efficiency of HPC is one more confirmation that ultra-supercritical steam process is very beneficial for the HPC (and whole steam turbine) operation. The lowest exergy efficiency is observed in LPC and is equal to 82.64%. The exergy efficiency of each LPC part (both left and right) is very close to exergy efficiency of the whole LPC, so it can be concluded that exergy efficiency of the LPC parts did not deviate much between each other.

Whole observed steam turbine has exergy efficiency equal to 90.85%, what is much higher in comparison to other steam turbines from various conventional power plants. Ultra-supercritical steam process is obviously not beneficial only in reducing the amount of heat which should be delivered by fuel in steam generator, it is also beneficial for the steam turbine process.

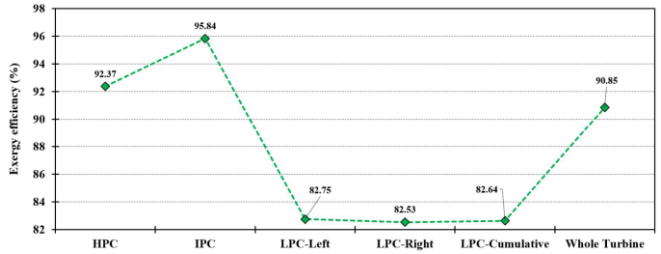

Fig. 6. *Exergy efficiency in all cylinders, cylinder parts and whole analyzed turbine from ultra-supercritical power plant*

Further research related to the observed steam turbine and its cylinders will be based on various Artificial Intelligence (AI) methods and processes [25-27] with an aim of more detail analysis and possible optimization.

6. Conclusions

This paper presents an exergy analysis of steam turbine (as well as all turbine cylinders and its parts) from ultra-supercritical power plant. Performed analysis allows detection of the cylinder with the lowest exergy efficiency (and the highest exergy loss) and can be used as a baseline in further research of ultra-supercritical steam

processes and their turbines. The most important conclusions obtained in this analysis are:

- By observing all the cylinders of the analyzed turbine, it can be stated that IPC is the dominant mechanical power producer (it produces mechanical power equal to 394.44 MW), it has the lowest exergy loss and simultaneously the highest exergy efficiency (equal to 95.84%). The best IPC performance of all cylinders can be explained by the fact that it operates in optimal regime (it did not operate with the highest steam pressure and temperature – which are the reason of increased losses in HPC and it did not operate with wet steam – which is the reason of increased losses in LPC).
- HPC has a very high exergy efficiency equal to 92.37%, regardless of the highest steam pressures and temperatures which occur in that cylinder. Very high exergy efficiency of HPC is confirmation that ultra-supercritical steam process is very beneficial for the HPC (and whole steam turbine) operation.
- LPC is a dissymmetrical dual flow cylinder, so both of its parts (left and right part) did not produce the same mechanical power, did not have the same exergy loss, but their exergy efficiency is very similar and in a range of entire LPC exergy efficiency (around 82.5%).
- The highest total exergy flows occur at each turbine cylinder inlet and outlet. The only exception from this conclusion is LPC outlet where the steam temperature is very close to the temperature of the ambient, what results with the small total exergy flow. Considering all operating points, the highest total exergy flow occurs at the HPC inlet (equal to 1308.87 MW).
- Whole observed steam turbine produces mechanical power equal to 928.03 MW, has exergy loss equal to 93.45 MW and has exergy efficiency equal to 90.85%. The exergy efficiency of the whole analyzed steam turbine is much higher in comparison to other steam turbines from various conventional power plants.

7. Acknowledgment

This research has been supported by the Croatian Science Foundation under the project IP-2018-01-3739, University of Rijeka scientific grant uniri-tehnic-18-18-1146 and University of Rijeka scientific grant uniri-tehnic-18-14.

8. References

[1] Sutton, I. (2017). Plant design and operations. Gulf Professional Publishing

[2] Tanuma, T. (Ed.). (2017). Advances in steam turbines for modern power plants. Woodhead Publishing.

[3] Mrzljak, V., Anđelić, N., Lorencin, I., & Sandi Baressi Šegota, S. (2021). The influence of various optimization algorithms on nuclear power plant steam turbine exergy efficiency and destruction. Pomorstvo, 35(1), 69-86. (doi:10.31217/p.35.1.8)

[4] Elhelw, M., & Al Dahma, K. S. (2019). Utilizing exergy analysis in studying the performance of steam power plant at two different operation mode. Applied Thermal Engineering, 150, 285-293. (doi:10.1016/j.applthermaleng.2019.01.003)

[5] Mrzljak, V., Poljak, I., & Mrakovčić, T. (2017). Energy and exergy analysis of the turbo-generators and steam turbine for the main feed water pump drive on LNG carrier. Energy conversion and management, 140, 307-323. (doi:10.1016/j.enconman.2017.03.007)

[6] Behrendt, C., & Stoyanov, R. (2018). Operational characteristic of selected marine turbounits powered by steam from auxiliary oil-fired boilers. New Trends in Production Engineering, 1(1), 495-501. (doi:10.2478/ntpe-2018-0061)

[7] Ahmadi, G. R., & Toghraie, D. (2016). Energy and exergy analysis of Montazeri steam power plant in Iran. Renewable and Sustainable Energy Reviews, 56, 454-463. (doi:10.1016/j.rser.2015.11.074)

[8] Ebrahimgol, H., Aghaie, M., Zolfaghari, A., & Naserbegi, A. (2020). A novel approach in exergy optimization of a WWER1000 nuclear power plant using whale optimization algorithm. Annals of Nuclear Energy, 145, 107540. (doi:10.1016/j.anucene.2020.107540)

[9] Adibhatla, S., & Kaushik, S. C. (2014). Energy and exergy analysis of a super critical thermal power plant at various load conditions under constant and pure sliding pressure operation. Applied thermal engineering, 73(1), 51-65. (doi:10.1016/j.applthermaleng.2014.07.030)

[10] Lin, X., Li, Q., Wang, L., Guo, Y., & Liu, Y. (2020). Thermo-economic analysis of typical thermal systems and corresponding novel system for a 1000 MW single reheat ultra-supercritical thermal power plant. Energy, 201, 117560. (doi:10.1016/j.energy.2020.117560)

[11] Rocha, D. H., & Silva, R. J. (2019). Exergoenvironmental analysis of a ultra-supercritical coal-fired power plant. Journal of cleaner production, 231, 671-682. (doi:10.1016/j.jclepro.2019.05.214)

[12] Mohamed, O., Khalil, A., & Wang, J. (2020). Modeling and control of supercritical and ultra-supercritical power plants: a review. Energies, 13(11), 2935. (doi:10.3390/en13112935)

[13] Kostyuk, A., & Frolov, V. (1988). Steam and gas turbines. Mir Publishers.

[14] Mrzljak, V., Lorencin, I., Anđelić, N., & Car, Z. (2021). Thermodynamic Analysis of a Condensate Heating System from a Marine Steam Propulsion Plant with Steam Reheating. Journal of Marine Science and Application, 20(1), 117-127. (doi:10.1007/s11804-021-00191-5)

[15] Medica-Viola, V., Pavković, B., & Mrzljak, V. (2018). Numerical model for on-condition monitoring of condenser in coal-fired power plants. International Journal of Heat and Mass Transfer, 117, 912-923. (doi:10.1016/j.ijheatmasstransfer.2017.10.047)

[16] Aljundi, I. H. (2009). Energy and exergy analysis of a steam power plant in Jordan. Applied thermal engineering, 29(2-3), 324-328. (doi:10.1016/j.applthermaleng.2008.02.029)

[17] Mrzljak, V., Poljak, I., & Medica-Viola, V. (2017). Dual fuel consumption and efficiency of marine steam generators for the propulsion of LNG carrier. Applied Thermal Engineering, 119, 331-346. (doi:10.1016/j.applthermaleng.2017.03.078)

[18] Mrzljak, V., Poljak, I., & Prpić-Oršić, J. (2019). Exergy analysis of the main propulsion steam turbine from marine propulsion plant. Brodogradnja: Teorija i praksa brodogradnje i pomorske tehnike, 70(1), 59-77. (doi:10.21278/brod70105)

[19] Poljak, I., Bielić, T., Mrzljak, V., & Orović, J. (2020). Analysis and Optimization of Atmospheric Drain Tank of Lng Carrier Steam Power Plant. Journal of Marine Science and Engineering, 8(8), 568. (doi:10.3390/jmse8080568)

[20] Tan, H., Shan, S., Nie, Y., & Zhao, Q. (2018). A new boil-off gas re-liquefaction system for LNG carriers based on dual mixed refrigerant cycle. Cryogenics, 92, 84-92. (doi:10.1016/j.cryogenics.2018.04.009)

[21] Mrzljak, V., Senčić, T., & Žarković, B. (2018). Turbogenerator steam turbine variation in developed power: Analysis of exergy efficiency and exergy destruction change. Modelling and Simulation in Engineering, 2018. (doi:10.1155/2018/2945325)

[22] Marjanović, D. (2022). Energy and exergy analysis of ultra-supercritical steam power plant. Graduation thesis, Faculty of engineering, University of Rijeka, Rijeka.

[23] Lemmon, E. W., Huber, M. L., & McLinden, M. O. (2010). NIST Standard Reference Database 23, Reference Fluid Thermodynamic and Transport Properties (REFPROP), version 9.0, National Institute of Standards and Technology. R1234yf. fld file dated December, 22, 2010.

[24] Mrzljak, V., Prpić-Oršić, J., & Poljak, I. (2018). Energy power losses and efficiency of low power steam turbine for the main feed water pump drive in the marine steam propulsion system. Pomorski zbornik, 54(1), 37-51. (doi:10.18048/2018.54.03)

[25] Baressi Šegota, S., Lorencin, I., Anđelić, N., Mrzljak, V., & Car, Z. (2020). Improvement of marine steam turbine conventional exergy analysis by neural network application. Journal of Marine Science and Engineering, 8(11), 884. (doi:10.3390/jmse8110884)

[26] Anđelić, N., Baressi Šegota, S., Lorencin, I., Poljak, I., Mrzljak, V., & Car, Z. (2021). Use of Genetic Programming for the Estimation of CODLAG Propulsion System Parameters. Journal of Marine Science and Engineering, 9(6), 612. (doi:10.3390/jmse9060612)

[27] Lorencin, I., Anđelić, N., Mrzljak, V., & Car, Z. (2019). Genetic algorithm approach to design of multi-layer perceptron for combined cycle power plant electrical power output estimation. Energies, 12(22), 4352. (doi:10.3390/en12224352)

Dynamic stability of a fluid-immersed, cracked pipe conveying fluid and resting on a Winkler elastic foundation

Svetlana Lilkova-Markova[1,*], Dimitar Lolov[2]
University of Architecture, Civil Engineering and Geodesy, Sofia, Bulgaria[1]
University of Architecture, Civil Engineering and Geodesy, Sofia, Bulgaria[2]
lilkova_fhe@uacg.bg, dlolov@yahoo.com

Abstract: *The dynamic stability of a cracked pipeline resting on a Winkler elastic foundation and immersed in fluid that is moving with a particular velocity is investigated. The Galerkin method is employed to approach numerically the problem. Conclusions are drawn on the influence of the rigidity of the Winkler elastic foundation on the critical flow velocity of the pipe.*
Keywords*: STABILITY, FLUID, CRITICAL VELOCITY, IMMERSED PIPE, WINKLER ELASTIC FOUNDATION*

1. Introduction

Fluid-immersed pipes, conveying fluid are used in many areas of the industry. They are widely used in the petroleum industry for transportation of oil and gas.

Numerous articles nowadays analyze the linear and nonlinear dynamics of the fluid-immersed pipes conveying fluid, proving the actuality of the problem.

Deng and Yang [1] studied the dynamics of pipes with different types of flowing fluid. The tubes are immersed in fluid. The pipe is considered as a cylindrical shell.

In [2] is presented an investigation about the dynamic stability of a pipe with a flowing fluid immersed in a non-viscous fluid moving at a constant speed. It is also given an analytical solution for the same type of pipe with a rigid body attached at one of its ends.

Pipelines often rest with its entire length or with part of it on an elastic medium. The first suggested model of that medium is the Winkler elastic foundation. Although it has some shortcomings it is still being widely used in civil engineering since its introduction in 1867. According to the model, any point deflection at the surface of an elastic medium is proportional to the applied load in the point and is independent on the applied loads at other points of the surface. Thus, the mechanical model of the elastic medium consists of a series of closely spaced and mutually independent linear elastic springs with rigidity k .

Cracks are the most encountered damages in the structures. They reduce the stiffness of the structural element which causes decrease in its natural frequencies and change in the mode shapes. In pipes conveying fluid, cracks lead to decrease in the critical flow velocity. The cracks could be hazardous for the system. They might lead to loss of stability if the reduced, due to the crack, critical velocity of the transported fluid is exceeded. That's why crack detection is a topic of much interest in the scientific community. Some of the studies for crack detection deal with change in the natural frequencies and Eigen forms, other with dynamic response to harmonic loads.

The present paper investigates the dynamic stability of a cracked, fluid-immersed pipe resting on a Winkler elastic foundation. The results obtained reflect the dependence of the critical fluid velocity on the rigidity of the Winkler elastic foundation. The results also show the effect of an open crack on the critical velocity of the fluid.

2. Problem formulation

The present paper uses the Euler-Bernoulli beam theory to investigate the dynamic stability of a fluid-immersed pipe of length l , conveying fluid and resting on a Winkler elastic foundation. The pipe, shown in Fig.1, is hinged at both ends. The pipe is supposed to have an open edge crack, which dimensions (θ_c and b) are shown in (Fig.1). b is the length of the crack. θ_c is the half central angle corresponding to the chord b . The crack severity is usually measured by the ratio θ_c / π . The crack position along the length of the tube is fixed through the coordinate x_c . The crack is modeled as a rotational spring with a lumped stiffness k_r [3] (Fig.2).

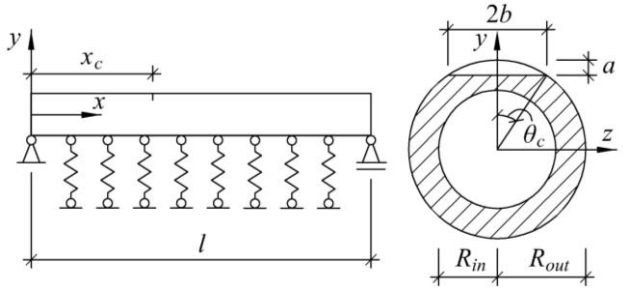

Fig. 1 *Static scheme of the investigated pipe*

The pipe is divided into two segments. The first segment is the left-hand side of the crack, and the second – is the right-hand side of the crack.

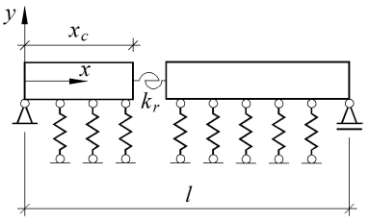

Fig. 2 *Mechanical model of the crack*

The transverse vibration of a fluid-immersed straight pipe conveying inviscid fluid and lying on a Winkler elastic foundation, with rigidity k , is governed by the following differential equation.

$$(1)\quad EI\frac{\partial^4 w}{\partial x^4}+\left(m_f V^2+m_e V_e^2\right)\frac{\partial^2 w}{\partial x^2}+2\left(m_f V+m_e V_e\right)\frac{\partial^2 w}{\partial x\partial t}+$$

$$+\left(m_f+m_p+m_e\right)\frac{\partial^2 w}{\partial t^2}+kw=0\,,$$

where t is the time, $w(x,t)$ is the lateral displacement of the pipe axis, x is the coordinate along the axis, EI is the rigidity of the pipe. The mass of the pipe per unit length is denoted by m_p , the mass of the fluid per unit length of the pipe by m_f and m_e is the added mass of the external fluid. V is the flow velocity of the fluid in the pipe and V_e is the velocity of the external fluid.

The added mass of the external fluid per unit length of the pipe m_e in the case when the pipe is close to a horizontal plane (Fig.3) is calculated by the following formula, given in [4]:

$$(2)\quad m_e=\pi\rho_e r^2\left(1+\frac{r^2}{2h^2}\right),$$

where ρ_e is the density of the external fluid.

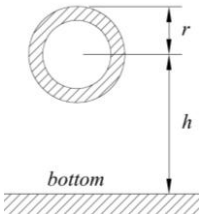

Fig. 3 *A scheme for obtaining the added mass of the external fluid*

The spectral Galerkin method is applied to approximate the solution of the boundary value problem (1). According to this method, an approximate solution is sought in the form [5]:

$$(3)\ w(x,t)=\sum_{i=1}^{n} y_i(x) z_i(t),$$

where:

$z_i(t)$ are unknown functions;

$y_i(x)$ are basic functions that satisfy the boundary conditions of the pipe. Such functions are the functions describing the *i*-th mode of vibration of a beam with the same static scheme as the immersed pipe.

On the basis of the differential equation, describing the lateral vibrations of an immersed tubular beam, filled with stationary fluid ($V=0$) is obtained [5]:

$$(4)\ y_i^{IV}(x)=\gamma_i^4\, y_i(x),$$

where:

$$(5)\ \gamma_i=\sqrt[4]{\frac{\left(m_f+m_p+m_e\right)\omega_i^2}{EI}},$$

where ω_i is the circular frequency of the beam.

Substituting equation (3) into equation (1), one obtains the residual function:

$$(6)\ R(x,t)=\sum_{i=1}^{n}\left\{\left(m_f+m_p+m_e\right)y_i\ddot{z}_i+2\left(m_fV+m_eV_e\right)y_i'\,\dot{z}_i+\right.$$
$$\left.+\left[\left(EI\gamma^4+k\right)y_i+\left(m_fV^2+m_eV_e^2\right)y_i''\right]z_i\right\}$$

In (6) and in the sequel, primes denote derivatives with respect to x and dots with respect to the time t.

The Galerkin method requires the residual function $R(x,t)$ to be orthogonal to the basic functions in the interval $x\in[0;l]$:

$$(7)\int_0^l R(x,t)\,y_k(x)\,dx=0,\ \text{for}\ k=1,...,n$$

Equation (6) is rewritten in the following form:

$$(8)\sum_{i=1}^{n}\int_0^l\left\{\left(m_f+m_p+m_e\right)y_i\ddot{z}_i+2\left(m_fV+m_eV_e\right)y_i'\,\dot{z}_i+\right.$$
$$\left.\left[\left(EI\gamma^4+k_w\right)y_i+\left(m_fV^2+m_eV_e^2\right)y_i''\right]z_i\right\}y_k\,dx=0\ \text{for}\ k=1,...,n.$$

Equation (8) represents a system of n differential equations with n unknown functions $z_i(t)$. In order to solve the system, the described in [5] method is applied. According to it the pipe is divided to sections with length Δx. The following relationships are taken into account:

$$(9)\int_0^l y_i\,y_k\,dx=\{y_i\}^T\{y_k\}\Delta x$$

$$(10)\int_0^l y_i'\,y_k\,dx=\{y_i'\}^T\{y_k\}\Delta x$$

$$(11)\int_0^l y_i''\,y_k\,dx=\frac{1}{EI}\{M_i\}^T\{y_k\}\Delta x$$

where in (9),(10) and (11):

$\{y_i\}$ - is a column vector consisting of the lateral displacements of the stations on the axis of the pipe, corresponding to the i-th Eigen form in the case of stationary fluid ($V=0$);

$\{y_i'\}$- is a column vector consisting of the rotations of the cross-sections in the stations on the axis of the pipe, corresponding to the i-th Eigen form in the case of stationary fluid ($V=0$);

$\{M_i\}$ - is a column vector consisting of the bending moments in the stations on the axis of the pipe, corresponding to the i-th eigen form in the case of stationary fluid ($V=0$).

Substituting (9),(10) and (11) in (8) the following system of n differential equations with n unknown functions $z_i(t)$ is obtained:

$$(12)\sum_{i=1}^{n}\left\{\left(m_f+m_p+m_e\right)\{y_i\}^T\{y_k\}\ddot{z}_i+\left[2\left(m_fV+m_eV_e\right)\{y_i'\}^T\{y_k\}_i\right]\dot{z}_i+\right.$$
$$\left.+\left[\left(EI\gamma^4+k_w\right)\{y_i\}^T\{y_k\}+\left(m_fV^2+m_eV_e^2\right)\frac{1}{EI}\{M_i\}^T\{y_k\}\right]z_i\right\}\Delta x=0$$

The system (12) could be rewritten in matrix form:

$$(13)\ M\,\ddot{z}+C\,\dot{z}+K\,z=0$$

The general solution of the system (12) is expressed through the roots ($\lambda_1,...,\lambda_{2n}$) of the equation:

$$(14)\ \det X=0$$

The elements of the matrix X are given by:

$$(15)\ X_{ik}=\lambda^2M_{ik}+\lambda C_{ik}+K_{ik}$$

$$(16)\ M_{ik}=\left(m_f+m_p+m_e\right)\{y_i\}^T\{y_k\}\Delta x,\quad M_{ik}=0\ (\text{when}\ i\neq k)$$

$$(17)\ C_{ik}=2\left(m_fV+m_eV_e\right)\{y_i'\}^T\{y_k\}_i\Delta x$$

$$(18)\ K_{ik}=\left[k_w\{y_i\}^T\{y_k\}+\left(m_fV^2+m_eV_e^2\right)\frac{1}{EI}\{M_i\}^T\{y_k\}\right]\Delta x+E_{ik}$$

$$(19)\ E_{ik}=EI\gamma^4\Delta x,\quad E_{ik}=0\ (\text{when}\ i\neq k).$$

On the basis of obtained roots ($\lambda_1,...,\lambda_{2n}$) could be drawn conclusions about the stability of the system. The system is stable if the real part of all the roots of the characteristic equation (14) is negative.

The roots ($\lambda_1,...,\lambda_{2n}$) depend on all the parameters of the system. If all of them are fixed except the velocity of the conveyed fluid V or the velocity of the external fluid V_e, one could obtain the corresponding critical velocities.

3. Crack modeling

It is considered that the bending vibrations of the Euler-Bernoulli beam is in the plane $x-y$ (Fig.1), which is also a plane of symmetry for the cross-section. The crack is assumed to be open. Castigliano's theorem is used to obtain the local flexibility in the presence of the crack [6]

(20) $c = \frac{\partial^2 U}{\partial M^2} = \frac{1-\nu^2}{E} \int_{-b}^{b} \int_{0}^{a} \frac{\partial^2 \left(K_I^2\right)}{\partial M^2} dx\, dy$,

where E and ν are respectively Young's module and Poisson's ratio. K_I is the stress intensity factor of bending. a and b are the crack dimensions as shown in (Fig.1). M is the bending moment.

(21) $K_I = \frac{M}{\pi R^2 t_p} \sqrt{\pi R \theta_c}\, F(\theta_c)$,

where $R = 0{,}5(R_{in} + R_{out})$, t_p and θ_c are respectively thickness of the pipe and the half central angle of the crack (Fig.1). $F(\theta_c)$ is calculated from the following formula [7]

(22) $F(\theta_c) = 1 + A_t \left[4{,}5967 \left(\frac{\theta_c}{\pi} \right)^{1,5} + 2{,}6422 \left(\frac{\theta_c}{\pi} \right)^{4,24} \right]$

(23) $A_t = \sqrt[4]{\frac{1}{8} \frac{R}{t_p} - \frac{1}{4}}$ for $5 \le \frac{R}{t_p} \le 10$

(24) $A_t = \sqrt[4]{\frac{2}{5} \frac{R}{t_p} - 3}$ for $10 \le \frac{R}{t_p} \le 20$.

The equivalent rotational spring stiffness

(25) $k_r = \frac{1}{c}$.

4. Numerical results

Numerical studies have been carried out for the system in Fig. 1.

The geometric and the material characteristics of the pipe are: the inner and the outer radii of the cross-section of the pipe are $R_{in} = 0.012m$ and $R_{out} = 0.014m$, Young's modulus $E = 210GPa$, the density of the material of the pipe $\rho = 7800 kg/m^3$. The density of the flowing fluid in the pipe is $\rho_f = 900 kg/m^3$. The density of the external fluid is $\rho_e = 1000 kg/m^3$.

The dimensions of the crack are $a = 0.001m$, $b = 0.005m$. The position of the crack is fixed with the coordinate $x_c = 1{,}1m$.

In the present paper 16 eigenfunctions $y_i(x)$ are used in the approximate solution (3).

For the pipe in Fig.1 is obtained the critical value of the flowing fluid V_{cr} for different rigidity of the Winkler elastic foundation. The velocity of the external fluid is assumed to be $V_e = 2m/s$ The results are shown in Fig.4.

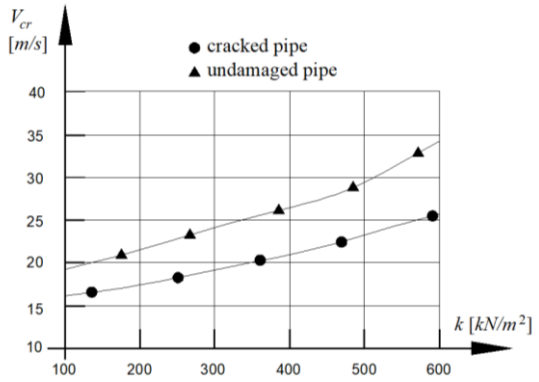

Fig. 4 *Critical value of the fluid velocity versus the rigidity of the Winkler elastic foundation*

4. Conclusions

The obtained results show that the Winkler elastic foundation has a stabilizing effect on the pipe - with increasing the rigidity of the foundation the critical velocity of the conveyed fluid increases. The crack has a destabilizing effect on the system, leading to decreasing of the critical velocity of the pipe flow.

5. References

1. Q. Deng, Z. Yang, Wave propagation in Submerged Pipe Conveying Fluid, Acta Mechanica Solida Sinica, Volume **32**, No.4, pp. 483 – 498 (2019)
2. A. Hellum, R. Mukherjee, A. Hull, Flutter instability of a fluid-conveying fluid-immersed pipe affixed to a rigid body, Journal of Fluids and Structures, Volume **27** , pp. 1086-1096 (2011)
3. O. Sadettin, Analysis of free and forced vibration of a cracked cantilever beam, NDT&E International, Volume **40**, pp.443-450, (2007)
4. C. Brennan, A review of added mass and fluid internal forces, Technical Report, Naval Civil Engineering Laboratory, (1982)
5. J. Wu, P. Shih, The dynamic analysis of a multispan fluid-conveying pipe subjected to external load, Journal of sound and vibration, Volume **239(2)**, pp. 201-215, (2001)
6. G. Eslami, et al., Effect of open crack on vibration behaviour of a fluid-conveying pipe embedded in a visco-elastic medium, Latin American Journal of Solids and Structures, Volume **13**, pp. 136-154, (2016)
7. S. In-Soo, et al., Dynamic behaviour of forced vibration of elastically restrained pipe conveying fluid with crack and concentrated mass, 9-th international Conference on Fracture & Strenght of Solids, Jeju, Korea, (2013)

Investigation of the influence of deformation temperature on the radial shear rolling mill on the microstructure evolution of copper

Abdrakhman Naizabekov[1], Kadyrgali Dzamanbalin[2], Irina Volokitina[1], Alexandr Arbuz[3], Sergey Lezhnev[1], Evgeniy Panin[4], Andrey Tolkushkin[1]

[1]Rudny Industrial Institute, Rudny, Kazakhstan
[2]Kostanay Social-Technical University named after academician Zulkharnai Aldamzhar, Kostanay, Kazakhstan
[3]Nazarbayev University, Astana, Kazakhstan
[4]Karaganda Industrial University, Temirtau, Kazakhstan
naizabekov57@mail.ru

Abstract: *One of the effective ways to control the properties of copper is to refine its structure to a nano- or ultrafine-grained level, and primarily with the help of severe plastic deformation. At the same time, radial-shear rolling is one of the promising methods for obtaining long-length rods with a gradient ultra-fine-grained structure. It is known from a number of scientific works that one of the main factors influencing the possibility of obtaining an ultrafine-grained structure in various ferrous and non-ferrous metals and alloys is the deformation temperature of these metals and alloys. The aim of the work is to study the influence of the deformation temperature at the radial-shear rolling mill on the microstructure evolution of copper. The following deformation temperatures of copper rods were selected for the planned studies: 20°C, 100°C and 200°C. The conducted studies have shown that the implementation of radial-shear rolling at ambient temperature compared with rolling at temperatures of 100°C and 200°C made it possible to achieve more intensive refinement of the initial structure. And first of all, this is due to the fact that with radial-shear rolling of copper, realized at ambient temperature, there are no dynamic return processes.*

KEYWORDS: *RADIAL-SHEAR ROLLING, TEMPERATURE, COPPER, MICROSTRUCTURE, GRAIN SIZE.*

1. Introduction

Copper is one of the most common non-ferrous metals. It has high anti-corrosion properties, both under normal atmospheric conditions, and in fresh and sea water and other aggressive environments. In the presence of atmospheric oxygen, a patina film forms on the surface of the copper product, which protects the metal from corrosion.

Copper is easy to process by pressure and soldering. Having low casting properties, copper is hard to cut and poorly welded. In practice, copper is used in the form of rods, sheets, wire, tires and pipes.

Due to its high thermal conductivity, copper is used for the production of current conductors and electrical products, refrigerating units, elements of thermal pipelines, heating and gas supply systems, as well as CCM crystallizers. Since copper is resistant to the influence of aggressive chemicals, rolled products from it are used in the oil, gas and chemical industries and for the manufacture of cryogenic equipment. Copper products have a very long service life, and throughout this period the products retain their appearance, strength and physical integrity.

Impurities have a great influence on the properties of copper, which are divided into three groups according to the method of exposure:

1) Impurities forming solid solutions with copper – nickel, antimony, aluminum, zinc, iron, tin, etc. Reduce the electrical and thermal conductivity of copper. In this regard, copper with a limited content of arsenic and antimony (0.002 As and 0.002 Sb) is used as current conductors. Antimony also reduces the ability of the alloy to hot plastic deformation.

2) Impurities that practically do not dissolve in copper – bismuth, lead, etc. Practically do not affect the electrical conductivity of copper, but worsen its pressure treatment.

3) Impurities forming brittle chemical compounds (sulfur, oxygen). Oxygen significantly reduces the strength of copper and reduces electrical conductivity. Sulfur improves the machinability of copper by cutting.

Another effective way to control the properties of copper, as well as other ferrous and non-ferrous metals, is to refine its structure to a nano- or ultrafine-grained level, and primarily with the help of severe plastic deformation [1]. Radial-shear rolling is one of the promising methods for obtaining long-length bars with a gradient ultrafine-grained structure [2-3]. At the same time, it is known from a number of scientific papers, including [4-7], that one of the main factors influencing the possibility of obtaining an ultrafine-grained structure in various ferrous and non-ferrous metals and alloys is the deformation temperature of these metals and alloys. To obtain an ultrafine-grained structure, the deformation process must be carried out at a temperature not exceeding the threshold for the beginning of recrystallization, since with an increase in the temperature of the deformation beginning, the probability of dynamic collective recrystallization during hot deformation increases, leading to undesirable grain enlargement. Therefore, the choice of the temperature regime is based on the fact that in the process of hot deformation, the primary recrystallization takes place completely, and the collective one is suppressed.

Since within the framework of the grant topic "Development of technology for obtaining ultrafine-grained structure in copper and its alloys by radial-shear rolling and structure control by ultrasonic processing", at the first stage we are faced with the task of obtaining ultrafine-grained structure by radial shear rolling in copper and its alloys, the purpose of these studies is to study the influence of such a technological factor deformations on the radial-shear rolling mill, as the rolling temperature, on the microstructure evolution of copper.

2. Experimental part

For the laboratory experiment, rods with a diameter of 25 mm and a length of 300 mm made of M1 grade copper were used. The choice of M1 grade copper as the starting materials is justified by its wide application in various industries, including medicine, mechanical engineering, instrumentation, cable industry, etc.

The following bar deformation temperatures were selected for the planned studies: 20°C, 100°C and 200°C.

At the first stage, a 25 mm diameter copper rod was deformed at room temperature on the SVP-08 radial shear rolling mill according to the reverse scheme shown in Figure 1. Rolling was carried out in four passes, up to diameters of 23 mm, 21 mm, 19 mm and 17 mm. At the second and third stages, copper rods with a diameter of 25 mm were heated in a Nabertherm tubular furnace to a temperature of 100°C and 200°C, respectively, with an exposure time of 25 minutes before deformation on the SVP-08 radial-shear rolling mill. After that, these bars were deformed on a radial shear rolling mill to a diameter of 17 mm also in four passes with an absolute compression step of 2 mm in diameter according to the above scheme.

Samples were cut from the initial bar and bars after the 2nd and 4th passes using the BRILLANT 230 cutting machine and slots were made for metallographic studies in the longitudinal section.

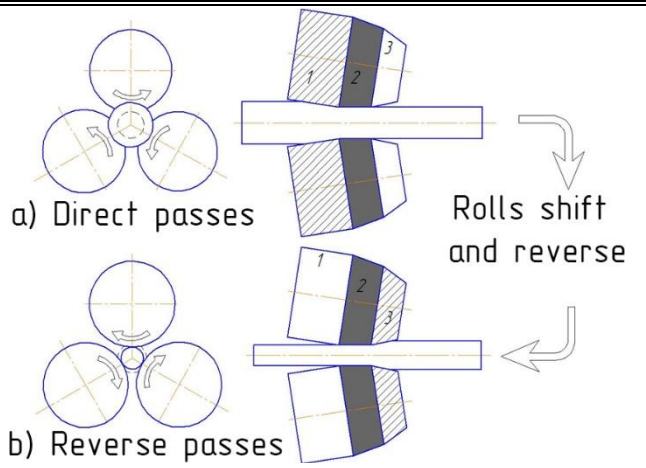

Fig. 1. *Scheme of reversible radial-shear rolling: 1 – crimping section for direct passes; 2 – calibration section for all passes; 3 - crimping section for reverse passes*

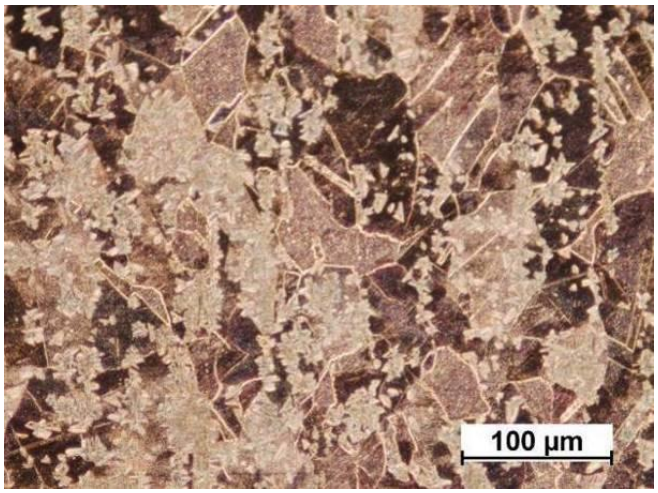

Fig. 2. *Initial structure of copper*

a)

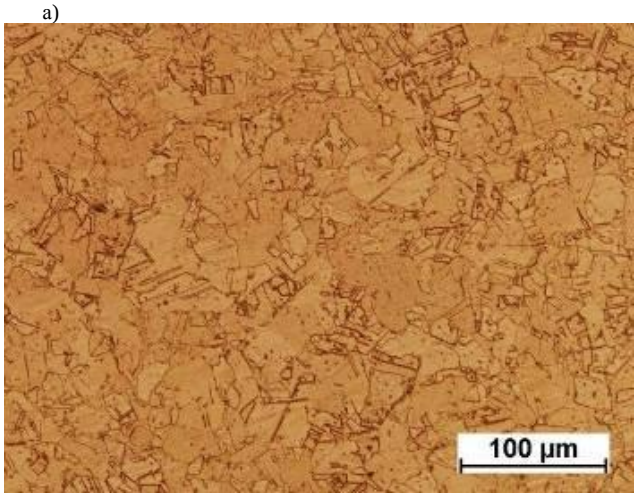

The microslips were prepared on a SAPHIR 520 grinding and polishing machine. To identify the microstructure , the polished surfaces of the samples were degreased with toluene and etched by wiping for 10-20 seconds with cotton wool with a solution of the following content: 75% saturated solution of $K_2Cr_2MnO_4$, 10% HHO_3, 10% HCL, 5% H_2SO_4. To increase the contrast, additional etching was carried out by immersion of the strip for 2-4 seconds in a solution of 10% HCL; 90% saturated $Cu_2(SO_4)_3$ [8].

Microstructure studies were carried out on a Leica DM optical microscope. Figure 2-3 shows optical photos of the microstructure before and after the 4th deformation cycle.

b)

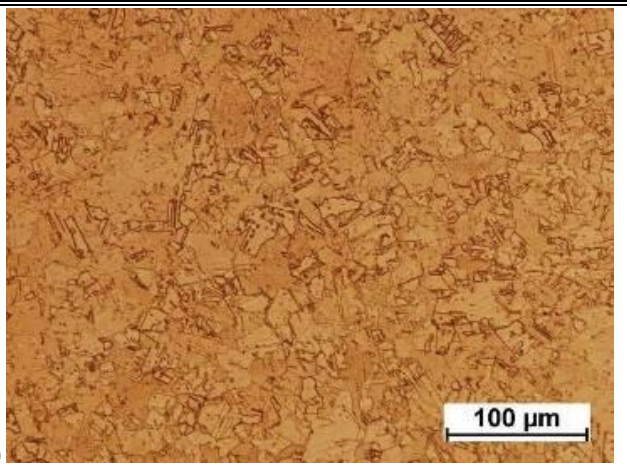

c)

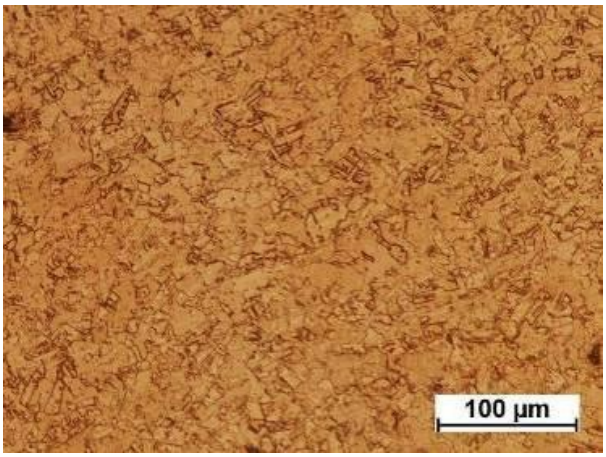

Fig. 3. *Microstructures of copper after 4 deformation passes on a radial-shear rolling mill at temperatures of 200°C (a), 100°C (b) and 20°C (c), respectively*

3. Results and discussion

Metallographic analysis of copper (Figure 3, 4) after radial-shear rolling showed that at all deformation temperatures, grain refinement occurs after each deformation pass. But at the same time, it has also been proved that when implementing radial-shear rolling at ambient temperature, the grain structure of copper rods is worked out more intensively. So at this temperature, the minimum average grain size after the fourth deformation pass on the radial-shear rolling machine was 6.0 microns, while the minimum grain size was 3.1 microns. The advantage of deforming copper samples on a radial-shear rolling mill at ambient temperature is primarily due to the fact that there are no dynamic return processes in this case.

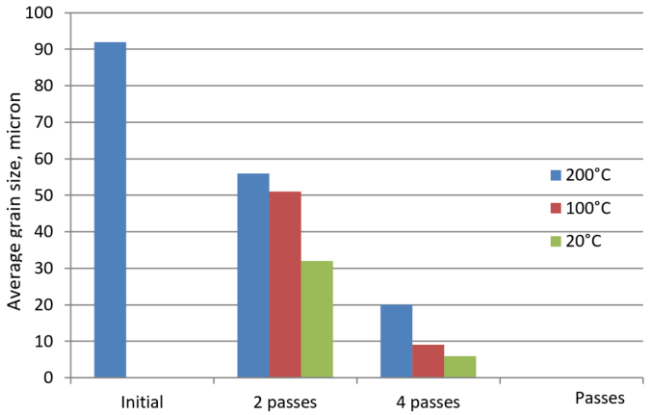

Fig. 4. *Average copper grain size by passes*

4. Conclusion

Based on the obtained results of metallographic studies, it can be concluded that the deformation temperature has a significant effect on the possibility of obtaining an ultrafine-grained structure in M1 grade copper when it is deformed on a radial shear rolling mill, which allows severe plastic deformation to be realized in the metal.

This research was funded by the Science Committee of the Ministry of Science and Higher Education of the Republic of Kazakhstan (Grant no. AP14869128).

References

1. Утяшев Ф.З., Рааб Г.И., Валитов В.А. Деформационное наноструктурирование металлов и сплавов. Монография. - СПб.: Наукоемкие технологии, 2020.

2. RU Patent № 2293619, A method of helical rolling, S.P. Galkin, 2007.

3. Galkin S.P. Radial shear rolling as an optimal technology for lean production// Steel in Translation. 2014. №44 (1). P. 61-64.

4. Демаков С.Л., Елкина О.А., Илларионов А.Г., Карабаналов М.С., Попов А.А., Семенова И.П., Саитова Л.Р., Щетников Н.В. Влияние условий деформации прокаткой на формирование ультрамелкозернистой структуры в двухфазном титановом сплаве, подвергнутом интенсивной пластической деформации. Физика металлов и металловедение, 2008, том 105, № 6. С. 638-646.

5. Дьяконов Г.С., Лопатин Н.В., Жеребцов С.В., Салищев Г.А. Исследование особенностей структурного состояния титанового сплава ВТ1-0 после комбинированной деформации при комнатной и повышенных температурах. Всероссийская школа семинар молодых ученых и преподавателей «Функциональные и конструкционные наноматериалы»: Сб. материалов. 2009. С. 99-102.

6. Найдёнкин Е.В., Иванов К. В., Голосов Е.В. Влияние криогенной прокатки на структуру и механические свойства никеля. Деформация и разрушение материалов. 2012. № 10. С. 33-37.

7. Мусабиров И.И., Сафаров И.М., Шарипов И.З., Нагимов М.И., Коледов В.В., Ховайло В.В., Мулюков Р.Р. Влияние температуры деформации осадкой на формирование мелкозернистой структуры литого сплава системы Ni−Mn−Ga. Физика твердого тела, 2017, том 59, вып. 8. С. 1547-1553.

8. Баранова Л.В., Демина Э.Л. Металлографическое травление металлов и сплавов. – М: Металлургия, 1986.

MAGMA 6.0 – toolkit and capabilities of the latest version Of the **MAGMASOFT** software package

Georgi Evt. Georgiev

Institute of Metal Science, Equipment and Technologies with Hydroaerodynamics Centre "Akad. A. Balevski",
Bulgarian Academy of Science,
evtimovg@abv.bg

Abstract: The possibilities for simulation and optimization of foundry technologies using the latest MAGMA6.0 version of the world-famous software package MAGMASOFT are presented. The capabilities of the software are illustrated both for the quick and efficient construction of the 3D geometric models and for the diagnosis of almost all possible defects in a wide range of casting methods. Special attention is paid to the possibilities for autonomous and automatic optimization of casting technologies in order to reduce defects and increase the profitability of castings.
KEYWORDS*: MATHEMATICAL MODELING, COMPUTER SIMULATION, OPTIMIZATION, FOUNDRY TECHNOLOGIES*

1. Introduction

MAGMASOFT is one of the world-famous software packages for computer simulation and optimization of a wide range of foundry technologies. It has long become an integral part of research, design and development activities related to the refinement and optimization of casting technologies, the creation of castings with high operational qualities, the reduction of metal consumption, the realization of energy savings, the sharp reduction of time for the design-implementation cycle, fast and accurate, qualitative and quantitative diagnosis of a wide range of possible defects [1].

Created by the company MAGMA Giessereitechnologie based in Aachen, Germany [2], the package is continuously developed and enriched by the company's employees, through the development of numerous scientific projects with various units of leading German institutes such as the Foundry Institute in Aachen, Max Planck Institute, etc. The mathematical models included in the program are constantly updated, reflecting most of the most important scientific developments in the field of materials science, whether they are the subject of doctoral dissertations or scientific publications. Both the mathematical models are being extended and improved, covering an ever-wider range of phenomena and processes, as well as the database, which allows the treatment of an ever-wider range of materials and alloys, as well as casting methods. It is a well-known fact that MAGMASOFT has no competition in terms of the built-in database in the package. In this way, it successfully competes with the most famous and powerful programs in the industry, such as ABBACUS, PROCAST, ANYCASTING, NOVACAST, 3D-FLOW, LM-FLOW, PATRAN, etc.

In our country and more precisely at the Institute of Metallurgy at the BAS "Acad. A. Balevski" (Imet-BAS) in Sofia has been using MAGMASOFT for more than 10 years. Since 2005, IMSTCHA-BAN is the exclusive and official distributor of MAGMA GmbH software products for Bulgaria and has their latest versions available. It is authorized both to sell licenses for the use of the programs and to conclude contracts for the provision of technological assistance and the realization of specific projects with simulations and optimizations of specific foundry technologies. This issue aims to present the latest capabilities of the latest version of MAGMA6.0 software for computer simulation and optimization of foundry technologies.

Every casting technology simulation and optimization project begins with geometric modelling of the product and casting equipment. That's why MAGMA pays special attention to the geometric modeler included in the software.

2. Geometry modelling in MAGMA6.0

The geometric modeler in this latest version of the software offers a full set of tools to quickly and easily build surfaces and bodies with complex geometry - Fig.1.

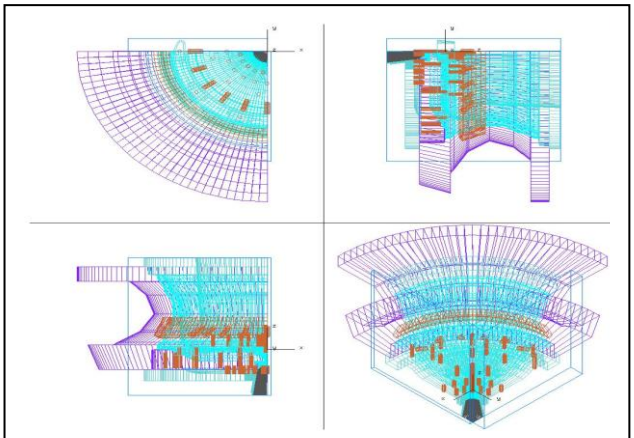

Fig.1.

The geometric modeler is equipped with all types of Boolean operations with 3D objects, enabling quick and easy construction and formation of new objects - Fig.2.

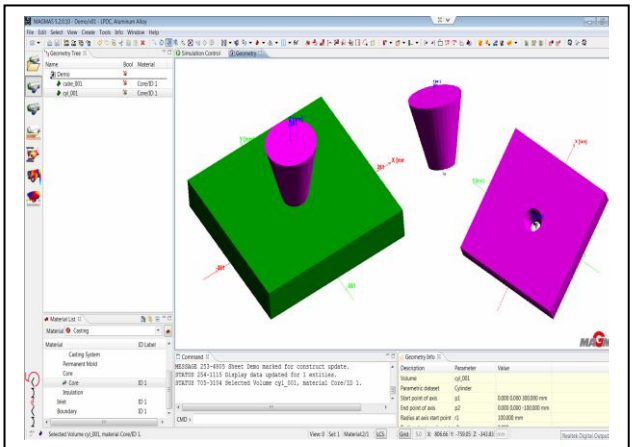

Fig.2.

In addition, MAGMA6.0 offers a full range of tools for building 3D bodies with complex geometry and it already supports almost all used formats for 3D design, as opportunities have been created to import geometric objects created with CAD products such as ProE, STEP, IDEAS, CATIA, NX, Solid Works, etc.

The software offers its own rich database of geometric elements such as feeders, runners, inlets, feeders, etc. while enabling customers to supplement this database with their own geometric elements – Fig.3.

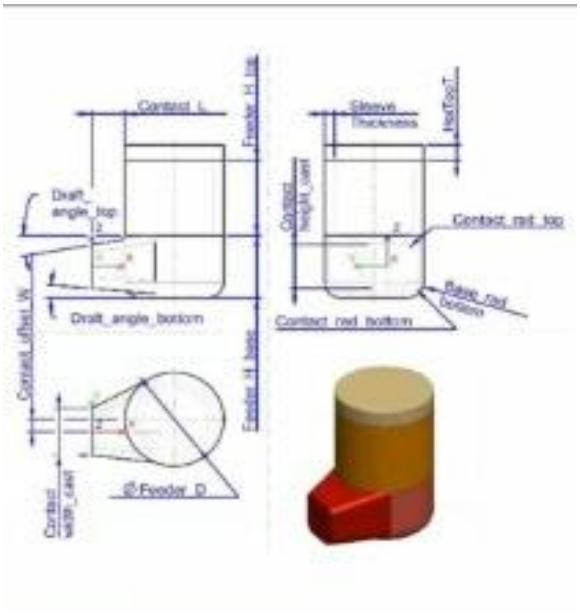

***Fig.3**. Geometry data base*

In addition, it also offers components and materials of world-famous databases such as FOSECO, ASK, GTP Schafer and CHEMEX.

The main advantages of the geometric modeler include:

- Visualization in the style of leading CAD programs;
- Ability to work with Boolean operations on geometric objects;
- Ability to read and export the geometric objects;
- The funnel system inlet boundary condition is generated along with the "Tracer" tool points automatically – Fig.4;
- Setting control points on a given plane;
- Ability to create your own geometric base of bodies and objects;
- Easy and convenient access to FOSECO's geometric databases;
- A rich set of tools for operating with geometric objects: rotations, extrusion, sections, multiplication and many others.
- Tooling disassembly check, geometric error indication and disassembly visualization – Fig.5

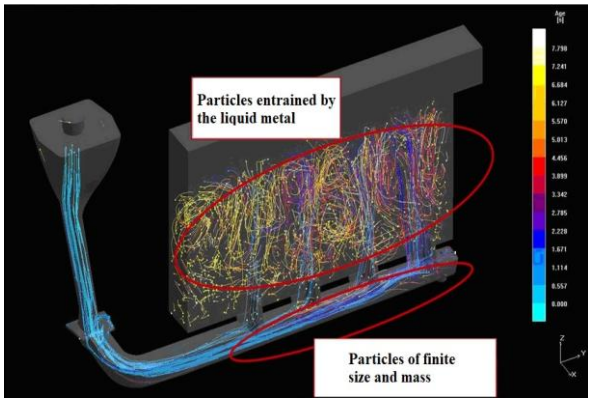

***Fig.4**. "Tracer" tool for particles of finite size and mass*

In the geometric modeler, some additional functions have been added, such as "shearing knife", object multiplication, vector or curve extruding, automatic "dressing" of differently oriented sections with a complex surface, separation and merging of objects, which make the modeler very useful.

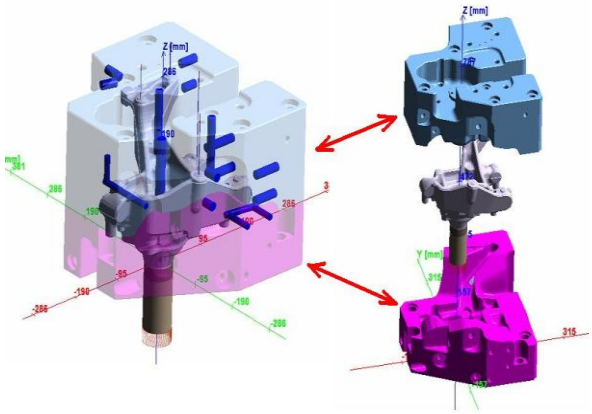

***Fig.5**. Disassembly visualization*

3. For the world of steel

Steel casting processes are characterized by:

- High pouring temperatures;
- Often large wall thicknesses;
- High levels of alloying elements.

For these reasons, the convective heat and mass transfer during cooling and solidification in many steel castings should not be neglected. It strongly influences the temperature distribution during the solidification process. Segregation of alloying elements exists at the grain or dendrite scale. Through the melt movement, these result in large concentration differences in the casting (macro-segregation).

At first, the local temperature differences in the melt are the driving force of the thermal convection. In Fig.6 you can see the thick-walled section of a casting in sectioned view. The warm and, thus, light material fractions shown in the center flow upwards, whereas the cold and heavy fractions at the edges flow downwards. This leads to the typical thermal convection movement.

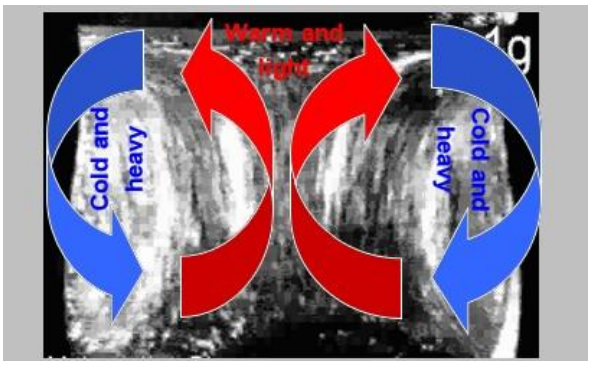

***Fig.6**. Thermal convection*

The flow motion is hindered by the progressive solidification. In the solidification interval, below the liquidus temperature, the liquid fractions increasingly convert to solid fractions. The resistance to the flow in the so-called 'mushy zone' is characterized by the permeability (Fig.7). It is stored in the material data set of the cast alloy according to the fraction solid.

If convection is considered for the solidification simulation of steel castings, the local values and directions of the velocity of the melt ('velocity') are additionally generated as simulation result. Similar to the flow occurring during the filling of the mold, also the flow movements caused by convection can be displayed by means of tracer particles. Particularly the

possibilities arising through tracer particles having both a size and a mass can be used to calculate, for instance, the movement of inclusions or slag particles with the convection. As in reality, particles in a "freezing" area are retained there and remain in the solidified casting.
The solver of MAGMA6.0 includes physical-mathematical model that realistically and adequately describe these phenomena.

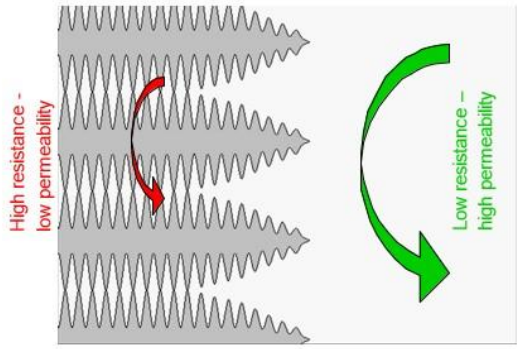

***Fig.7**. Resistance to the convective flow through growing dendrites: Permeability K*

***Fig.8**. Modelling of the thermo-solute convection*

MAGMA6.0 is also equipped with a model describing macro-segregation in castings. For every alloying element, the solubility both in the solid state and in the melt changes based on temperature. The resulting concentration differences in the solid state can only be balanced by means of diffusion processes, which requires a certain time. Cooling usually occurs so fast that this balance cannot be fully achieved.

Alloying elements not incorporated into the solid during solidification accumulate at the solid-liquid interface. The result is a concentration gradient in the solidified material. This so-called micro-segregation occurs at the crystal/ dendrite scale.
If it was possible to quickly balance the concentration differences in the crystal, a constant concentration would be reached here as well – namely, the equilibrium concentration. In reality, however, a balance of the concentration can only be achieved through the process of diffusion. This process is very slow, resulting in varying concentrations in the crystal based on the distance from the solid-liquid boundary. As solidification progresses, the solid-liquid boundary moves in the direction of the arrow.

Through the convection of the molten steel, the inhomogeneities existing in the crystal produce concentration differences, which are widely spread throughout the casting (macro-segregation). Fig.9 schematically shows the convection flow which entrains the segregated area of a solid-liquid interface. Fig.10 depicts the Cr concentration in a casting as a simulation result.

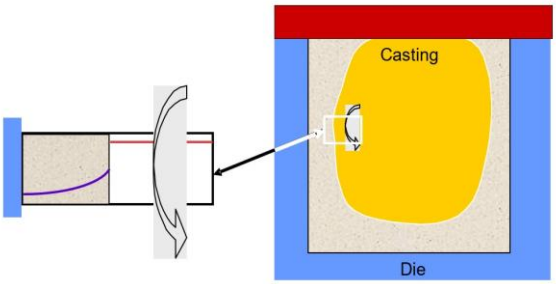

***Fig.9**. Through the convection in the casting, the micro-segregation (to the left) is widely spread and is converted to macro-segregation*

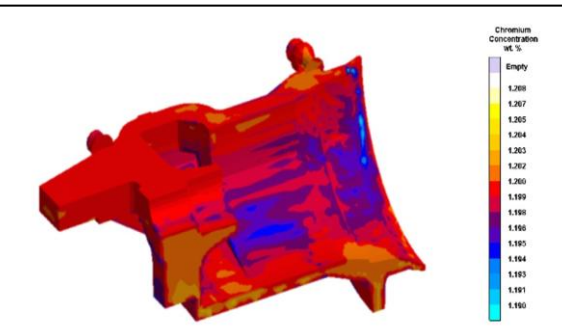

***Fig.10**. Macro-segregation shown using the example of the Cr concentration*

MAGMA6.0 calculates and visualizes also the distribution of austenitic gain size and steel microstructure - Fig.11.

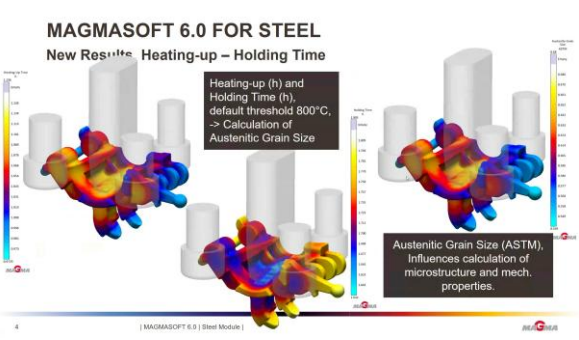

***Фиг.11**.*

Two new characteristic temperatures are also offered in the version -A3 and martensite start temperature, based of segregation calculations – Fig.12.

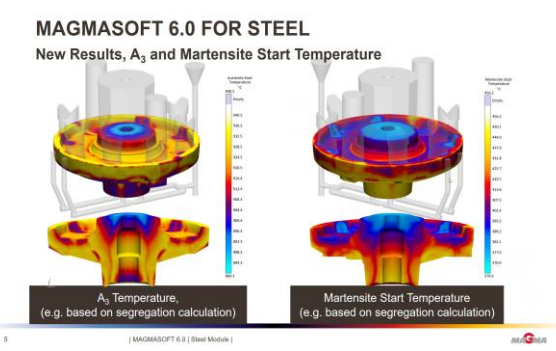

***Fig.12**.*

The software also offers a prediction of the hardness distribution in different units (Vickers, Rockwel and Brinell) of the formed casting at each of its points - Fig.13.

Fig.13.

Additional it give as a phase distribution based on CCT diagrams – Fig.14.

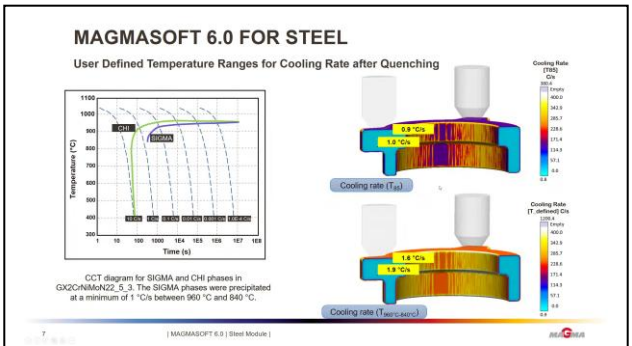

Fig.14.

4. Autonomous and automatic optimization

MAGMA is the first of the software products for the simulation of foundry technologies, offering, in addition to the classic approach for their optimization through an interactive - iterative computer-operator process, the implementation of automatic and autonomous optimization of the components of the casting-mold system, as well as of the technological parameters. An algorithm is build and followed for this purpose for optimization of the foundry technological process [3]. It starts with a heuristic version of the technology, goes through an internal cycle of automatic optimization, realizing goals set by the operator in advance, and is closed by an iterative circle, including the judgment of the specialist - technologist.

For the purposes of automatic optimization, the geometric objects are parameterized, which makes them useful to be vary these parameters in pre-set intervals. One such parameterization is presented in Fig.15 on the example of a simple feeder.

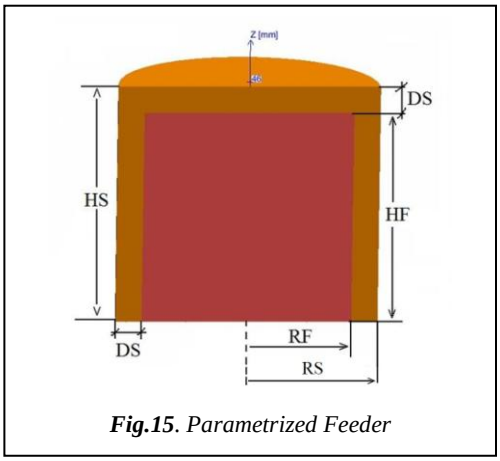

Fig.15. *Parametrized Feeder*

To select the optimal solution, a special toolkit is applied, one of its components being the diagram presented in Fig.16.

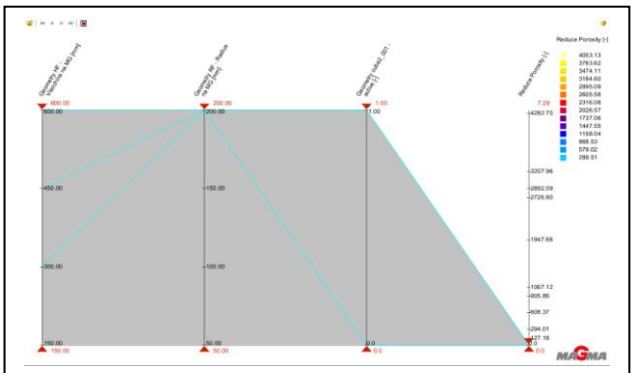

Fig.16.

4. New casting methods in software viewNew foundry technologies are

4.1. Continuous casting

From several years, MAGMA has been actively and successfully developing modules dealing with the formation of ingots under continuous casting conditions for aluminum and steel alloys. It is schematically presented in Fig.17.

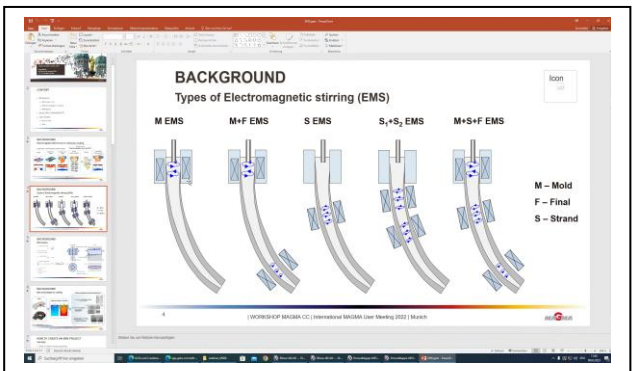

Fig.17.

In the latest version of the MAGMA6.0 software, the mathematical model is enriched with the possibility of electromagnetic stirring of the liquid phase along the length of the ingot - Fig.18 and Fig.19.

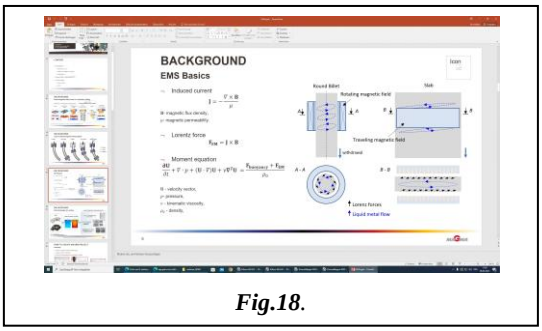

Fig.18.

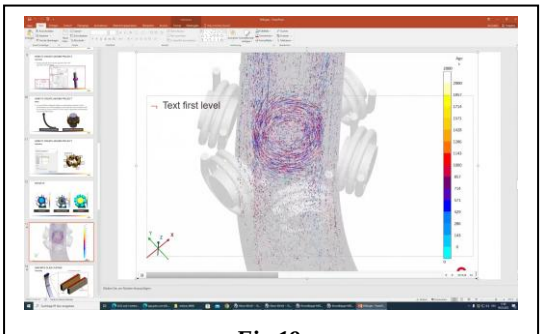

Fig.19.

4.2. MAGMA core – mold simulation

MAGMAc+m is a completely new simulation software designed to model the core production process. It makes core production predictable. Trial and error is replaced with knowledge. The program uses validated models for the multiphase flow during core shooting. It considers the curing kinetics during gassing and purging for the commonly used 'PU-Cold-Box' and also for the increasingly used inorganic binder systems. MAGMAc+m covers the complete core production process: core shooting and core curing. It is perfectly integrated into the MAGMA6.0 environment.

During core shooting, sand is rapidly forced into the core box by a sudden expansion of air. The real machine does not provide any insights into the processes taking place during core production. Little is known about how the processes work. In practice, the design of core boxes and the determination of suitable process parameters are done based on experience and, ultimately, by using trial and error. Core shooting is the most important process step. After shooting, the core sand must be compacted in all relevant core areas. Most of the optimization work is done when optimizing the core shooting process to ensure the required quality of the cores. Expanding air shoots sand through the shoot nozzles into the core box. The sand compacts in the core box and the air escapes through the core box vents (and possibly through the ejector gaps and via the parting line).

A typical scheme for the formation of sand cores by shooting is shown in Fig.20.

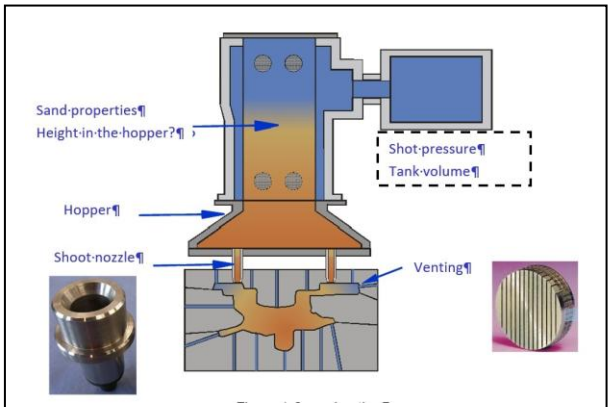

***Fig.20**. Core shooting*

The core curing process depends on the binder system used. For gas curing processes, different curing gas types are used that are either part of the chemical reaction or that are necessary to accelerate the curing through reaction catalysis. Its operation scheme is presented in Fig.21

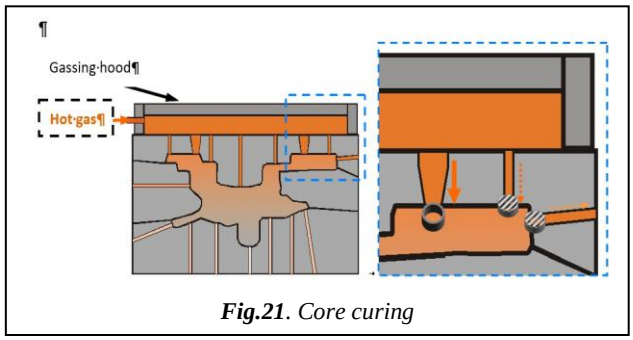

***Fig.21**. Core curing*

The hopper is replaced with a gassing hood. Usually, the complete "open area" at the top of the core box is used for "active" gassing. Hot gas is injected into the core box, and the core is cured. The curing physics and chemistry strongly depend on the binder type. The methodology is used for all common gassing procedures, for PU cold box systems as well as for inorganic binders.

Other systems such as hot box or croning systems are simply cured in a thermally controlled core boxes without additional gassing.

The follow image shows typical core production geometries in the Geometry Perspective's workspace of MAGMA6.0 – Fig.22.

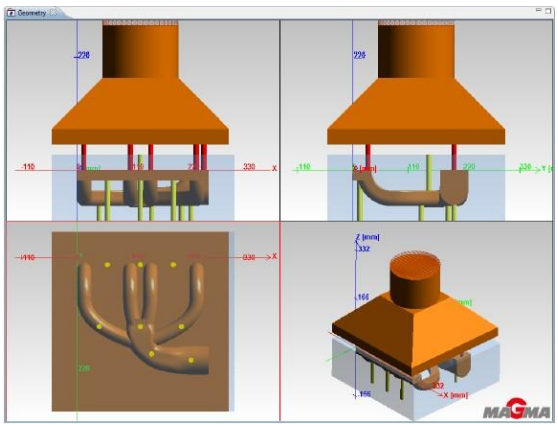

***Fig.22**. Geometry for core shooting wit hopper and inlet in four-view layout*

The simulation with MAGMA 6.0 of both processes leads to a reliable assessment of the quality of the formed core – Fig.23.

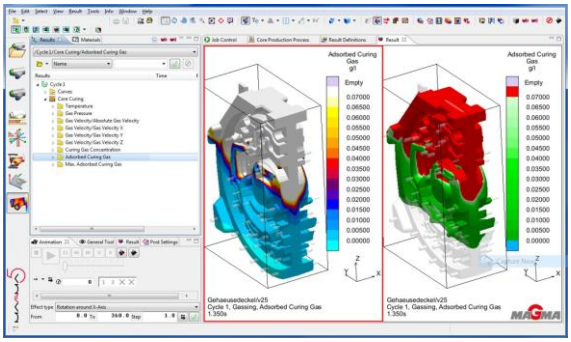

***Fig.23.** The concentration of the adsorbed curing gas constitutes an excellent criterion for the evaluation of core curing*

5. Conclusion

The MAGMA6.0 software package is based on state-of-the-art mathematical models of the physical processes involved in the formation of castings, making it an extremely useful tool for:

- formation of high-quality castings;
- forecasting the structure and mechanical properties of the products;
- optimization of a wide range of casting technologies;
- assessment and control of the quality of the manufactured products;
- increasing the economic efficiency of foundry technologies.

The author is convinced that the new generation of the software will be extremely useful in efforts to improve the efficiency of foundry technologies by forming high quality products with minimal material, energy and human resources.

6. References

1. Flemings, M.C., Solidification Processing, NY, Massachusetts Inst. of Technology,1974.
2. Sahm P. R., P. N. Hansen, Numerical Simulation and Modelling of Casting and Solidification Processes for Foundry and Cast-house", CH-8023, Zurich, CIATF, 1984.
3. Georgiev G. Evt., N. Tonchev, Iv. Georgiev, P. Petrov, V. Videv, Computer Optimization of a Technology for Forming a Steel Casting, Engineering Sciences, ISSN 1312-5702, LII, № 2, pp.73-80, 2015.

Hazards at the production of titanium alloys in the electric arc furnace

Prof. Dr Slokar Benić Lj.[1], Assist. Prof. Dr Ivec I.[1], Čačić K.[1]
University of Zagreb, Faculty of Metallurgy – Sisak, Croatia[1]
E-mail: slokar@simet.unizg.hr, iivec@simet.unizg.hr, katarinacacic07@gmail.com

Abstract: *This article describes the metal titanium, its characteristics and properties, and the types of titanium alloys with regard to its microstructure. It also describes the production processes, i.e. the melting and casting processes of titanium alloys. The focus is on the production of titanium alloys by the electric arc process, and possible hazards in the production of titanium in electric arc furnaces are also described. Suitable protective measures to be taken in the event of a particular hazard are also highlighted. Concerning the occurrence of possible accidents in the production of titanium, a calculation is also presented that shows how much needs to be invested in protection against possible accidents while maximising profit. Finally, the application and casting process of titanium alloys in dentistry is presented.*
Keywords*: TITANIUM, PRODUCTION OF TITANIUM ALLOYS, HAZARDS, ELECTRIC ARC FURNACE, COMPUTER PROCESSING, DENTISTRY*

1. Titanium and its alloys

Titanium is a hard, light and polymorphic metal that has numerous modifications of crystal structure. At room temperature, the hexagonal close-packed (hcp) lattice, known as α phase, is stable and at 882 °C transforms into a body-centred cubic (bcc) lattice, known as β phase. The alloying elements have a great influence on this transformation temperature. The elements that lower the temperature of alpha/beta transformation are called alpha stabilisers and include: Al, N, B, O, C. The elements that raise the temperature of the alpha/beta transformation are called beta stabilisers and include: Co, Cr, Cu, Mo, Ta, Nb, Ni, W, V. Therefore, titanium alloys can be divided into alpha and near-alpha alloys, beta alloys, alpha+beta alloys and unalloyed titanium. Due to this allotropic transformation, titanium alloys exhibit a wide variety of properties. Among them, excellent biocompatibility and corrosion resistance are the most important for use in dentistry, as is the modulus of elasticity. Titanium alloys of the β-type meet these requirements [1][2] [3] [4] [5] [6].

2. Methods of titanium alloys production

Titanium components are manufactured by casting, forging and powder metallurgy. The casting process results in homogeneous and pure alloys at a low price [7].

Of the various processes for melting titanium and its alloys, two are most commonly used commercially: arc melting in a vacuum and electron beam melting. However, research is continuing to develop other methods for better melt control and better utilisation of processing residues [8]. Vacuum melting processes are routinely used to manufacture products with the highest quality standards. However, the reactivity of titanium and the special conditions provide many opportunities for product defects to occur. Inclusions and porosity are particularly undesirable as they can serve as a cause of stress and failure due to material fatigue [9].

2.1. Electron beam melting

Electron beam melting (EB) is approved for the production of ingots of reactive metals such as titanium, niobium, tantalum and superalloys weighing up to 2.5 tons that can be accommodated in a single furnace. Electron beam melting is characterised by the following features: flexibility and the ability to control the process temperature, speed and reaction; the use of a wide range of raw materials in terms of material quality, size and shape [10].

Electron beam (EB) furnaces are attractive for remelting scrap into ingots and slabs. The clean, granulated, mixed raw material is introduced into the EB furnace through a vacuum system into the melting hearth, which is cooled with water. The metal is thoroughly degassed; high-density impurities sink and collect, and the liquid metal is continuously poured into a water-cooled mould. Electron beams strike the melting area and pour the metal into the crucible to ensure good melting and healthy ingots, which are slowly pulled out of the furnace [9].

The production of titanium castings in EB melting furnaces is not cost-effective because of the high vacuum required. However, it is economical if large quantities of castings of the same size and mass are involved and if a wide range of alloying agents can be used. Another advantage of EB melting is the ability to superheat the pool immediately before casting. However, controlling alloying elements such as aluminium, tin and chromium is very difficult as these alloying elements have high evaporation pressures [10][11].

2.2. Vacuum induction melting

Vacuum induction melting (VIM) can be used in many applications, especially for reactive titanium alloys and complex moulded parts. In vacuum induction melting, the primary conductor is el. current wound and generates secondary currents by electromagnetic induction, which develop heat inside the metal charge. Melting takes place under a vacuum or inert gas atmosphere by electromagnetic induction using coils. It enables rapid homogenisation of the melt by electromagnetic stirring. The advantage of this melting method is that the electromagnetic mixing of the melt ensures the homogeneity of the chemical composition of the alloys. Concerning the material of the crucible, a distinction is made between indirect and direct induction heating. The graphite crucible used for indirect heating should be preheated before the titanium is melted by the induced heat. However, a vacuum should be ensured to avoid contamination by the graphite. For direct melting, crucibles made only of CaO are used because of the strong affinity of titanium for oxygen. However, care should be taken when using CaO as it has high hygroscopy and low handling strength [7] [10].

2.3. Plasma arc melting

Plasma arc melting (PAM) uses the heat of thermal plasma in an argon atmosphere to produce materials. The furnaces operate under slight overpressure to prevent contamination with oxygen and nitrogen and the selective vaporisation of alloying elements. The PAM process uses copper crucibles cooled with water and porosity and flowability are retained [7] [9].

There are also advanced melting processes such as vacuum plasma spraying or selective laser melting that do not require crucibles and produce high-quality castings [7].

2.4. Casting of titanium

Titanium casting can be performed by static, centrifugal, vacuum die and countergravity casting.

Static casting is a simple method of casting titanium that requires no additional equipment. However, the pouring rate and superheating of the melt cannot be controlled, so it is very difficult to ensure the required flowability. In addition, there is an interfacial reaction between the metal and the mould.

Flowability is improved by centrifugal force in this method of casting. Centrifugal force can be applied horizontally or vertically. The vertical method produces porous castings due to turbulent melt flow. The advantage of horizontal casting is that the centrifugal

force does not occur in the mould, but the melt itself pours into the mould under the influence of the centrifugal force.

Vacuum die-casting is a cost-effective alternative to mould casting. Higher productivity rates are achieved with this casting process. However, the porosity caused by the turbulent flow of the melt cannot be avoided due to the application of pressure. An even bigger problem with vacuum-die casting is the lack of suitable materials for making moulds for titanium castings. Therefore, only titanium alloys with a low melting point can be cast in this way.

The CLV process allows for better mould filling, better casting, less mould erosion and fewer oxide inclusions. The disadvantage of this process is that a ceramic crucible and mould are required for casting, so there is the contamination of the titanium castings by the materials of the crucible and mould [10].

3. Hazards in the production of titanium alloys in the electric arc furnaces

Arc melting (AM) is the melting of an alloy by means of an arc generated between an electrode and a water-cooled casting mould, usually of copper, in a vacuum or inert gas atmosphere. The electrode may be consumable, i.e. made of titanium or a titanium alloy, or non-consumable, e.g. made of tungsten. If a consumable titanium electrode is used for melting, the process is called vacuum arc melting (VAM). Arc melting produces ingots of the highest purity. The disadvantage of the process is that the ingots are not homogeneous and have to be remelted several times. Therefore, this melting process is mainly used in laboratories [7] [13].

The commercial production of titanium began around 1950. Earlier safety problems resulted from a lack of knowledge about the construction of the furnaces and possible explosions. The knowledge at that time was based on steel technology, so hydrogen explosions were a completely new problem. When molten titanium reacts with water, it decomposes, binding oxygen and releasing hydrogen, and an explosion occurs. The next problems that challenged the industry were sponge fires and explosions. The third problem was the operator's entry into the work area, where there is not enough oxygen to breathe, but gases such as argon, nitrogen and other inert gases are prevalent. To solve these problems, safety committees were formed, safety procedures were developed and the safe operation of the plants was ensured. The melting of titanium in a water-cooled furnace with copper crucibles naturally involves risks. Namely, water leakage can occur, which is why everything is done to avoid this. The problem arises when water comes into contact with molten titanium because then the water turns into steam. Titanium has such an affinity for oxygen that it decomposes water, absorbs oxygen and releases hydrogen. Under these circumstances, both steam and hydrogen explosions are possible. The aim is therefore to develop equipment, processes and facilities that function safely. If a problem occurs, equipment and procedures must be developed to ensure the safety of all involved, even under the worst conditions. When water enters the furnace, it causes an explosion, which occurs in two stages. The first is a steam explosion, followed by a hydrogen explosion. In one of the first industrial explosions, it was calculated that the combined explosion was equivalent to a bomb with an explosive force of 100 to 200 TNT, which is obviously not good in a melt. The first industry-wide safety committee was established in the late 1950s and operated until 1965. They produced guidelines for plant operation and design that were accepted by the industry and are still widely used today. The main outcomes were improvements in the design of furnaces, the relocation of melting areas to sheltered areas and the relocation of operators out of the working area. Since then, there have been a significant number of explosions in the industry, but the number of tragic deaths has been reduced to a minimum. The most common accidents that occurred were fires. The most common cause of the fire was poor maintenance and operator inexperience. Examples from 2000 show how expensive such fires can be, when there were five fires that cost the titanium industry around $ 1 million. Therefore, in the following, we calculate how much needs to be invested in protecting against potential accidents while maximising profit [14].

First, for the sake of simplicity, we will assume that there is only one possible accident and that N is the value of material damage from that accident, and with $o(x)$ we will denote the danger (in percentages, so $o(x) \in [0,1]$) that the accident will occur in some fixed time interval (e.g. annually). At the same time, x is the amount of money that we invest in protection with which we want to prevent an accident from happening. In doing so, it is logical to assume that it is always necessary to invest the same amount y to halve the risk. Therefore, we assume that if by investing a monetary amount y we reduce the risk from, for example, 20% to 10%, by investing an additional amount y we will reduce the risk from 10% to 5%. This is logical to assume because this is exactly how nature works in various processes. Let us recall, for example, radioactive decay. If, after T years, the amount of radioactive substance decreases, for example, from 2 kg to 1 kg, then after additional T years the amount will decrease from 1 kg to 0.5 kg (T is exactly what physicists call the half-life). If we now remember the famous saying "time = money", the comparison is complete.

So we assume that

$$o(x+y) = \frac{o(x)}{2}.$$

If we apply that formula several times, we get:

$$o(x+ny) = \frac{o(x+(n-1)y)}{2} = \frac{o(x+(n-2)y)}{4} = \cdots = \frac{o(x)}{2^n}.$$

If we now put $x = 0$, we get $o(ny) = o(0) \cdot 2^{-n}$, and after the substitution $x = ny$ we can write that formula in the form

$$o(x) = o(0) \cdot 2^{-\frac{1}{y}x}.$$

For simplicity of calculation, we will write this formula below in the form of an exponential function with a natural base:

$$o(x) = A \cdot e^{-ax}. \qquad (1)$$

Here we have $A = o(0)$ and $a = \ln\left(2^{1/y}\right)$. Of course, A and a are generally unknown parameters that can only be estimated empirically for the corresponding type of danger. Nevertheless, a quality assessment of these parameters is necessary for the successful application of this model.

If we denote by P the expected profit from business in the observed period, the actual average profit for that period is in fact

$$p(x) = P - x - N \cdot o(x), \qquad (2)$$

i.e. the profit from the business should be reduced by the costs of accident protection and potential costs if an accident occurs. Namely, over m periods we expect $m \cdot o(x)$ accidents with total material damage $N \cdot m \cdot o(x)$, i.e. the average expected damage per period is exactly $N \cdot o(x)$.

If we substitute (1) in (2) we get

$$p(x) = P - x - N \cdot A \cdot e^{-ax},$$

and we expect the maximum profit at the zero point of the first derivative:

$$p'(x) = -1 + N \cdot A \cdot a \cdot e^{-ax}.$$

We can see that it is really a maximum from the fact that the second derivative is negative:

$$p''(x) = -N \cdot A \cdot a^2 \cdot e^{-ax} < 0.$$

By solving the equation $p'(x) = 0$ we get

$$x = \frac{\ln(N \cdot A \cdot a)}{a}, \qquad (3)$$

i.e. formula (3) determines how much money should be invested in accident protection to maximise profit (over a long period). Here, N is something that we can estimate more easily because it is the value of the material damage that the accident would cause, while the parameters of the model A and a are more difficult to estimate. We can only estimate them based on experience, i.e. by studying data on previous accidents and previous investments in protection.

If we are threatened with several possible accidents, the situation is even more complicated. Let us assume that we have d possible accidents with potential material damages $N_1, N_2, \cdots, N_d$ and with $x_1, x_2, \cdots, x_d$ denote the monetary amounts that we will invest in protection against each accident. If these investments are independent, i.e. if protection from one accident does not contribute to protection from another, then formula (3) can be applied to each accident, i.e. for each $i \in \{1,2, \cdots, d\}$ it holds

$$x_i = \frac{\ln(N_i \cdot A_i \cdot a_i)}{a_i},$$

i.e. for each potential accident, its model parameters A_i and a_i should be determined empirically.

The situation is most complex if protection against one accident also contributes to protection against another accident, but we will not deal with that in this paper.

3.1. Hazards of the explosions

To understand the danger of a steam explosion, one must know the cooling technology in the electric arc furnace and its development. Older electric arc furnaces were fitted with refractory linings so that the furnace could withstand extremely high temperatures. Although the linings did not melt, they tended to disintegrate when the furnaces were operated at higher capacities with much higher temperatures and pressures. The solution was to protect the arc furnace covers and other components with a system of tubular plates through which high-pressure water was pumped to ensure cooling. Although water under pressure is an effective coolant, it becomes a problem when cracks occur, which is relatively common in highly loaded furnaces. Most cracks are small cracks caused by thermal fatigue, which is characteristic of heavily welded structures. Cracks can also occur when an irregular arc strike or mechanical penetration causes holes during operation, allowing water to enter the furnace even faster under very high pressure and in possibly large quantities. Water poured into the furnace does not cause an explosion by itself when it stands on the molten mass. The problem occurs if the surface wobbles or tilts when the melt is poured. This can cause the sloshing molten metal to envelop the water and immediately turn it into steam. The steam then expands to 1,700 times its original volume, causing a violent explosion that can lift off the roof of the furnace and release steam, melt and debris over long distances from the furnace, putting people and equipment at risk.
The most important approach to preventing explosions in piping systems is to install an electronic monitoring system that measures the water content of the exhaust gas and detects irregularities [15].

3.2. Hazards at the entry in the limited area and inert gases

Problems in the industry are often caused by misjudgement. For example, by entering a confined space where there is not enough oxygen. A confined space is defined as an area that is restricted or has limited entrances and exits, but is large enough for workers to enter to perform their work. The main gases used in titanium production are argon, helium, nitrogen, chlorine and titanium tetrachloride. Every worker must be trained before being assigned to work that requires entering an enclosed space. Training is required if the work changes to an enclosed space and this poses a risk to the worker. Before entering the confined space, the nature of the work must be explained and access worked out in detail, and everyone must know how and in what way to behave in the event of a hazard. Care must be taken to ensure that all devices, such as supply and ventilation connections or similar, are switched off or mechanically locked. All mechanical devices that may endanger the safety of workers shall be locked and marked. The atmosphere shall be tested for the presence of oxygen and the lower flammability limit. The internal atmosphere shall be tested for toxic substances if they are suspected. The oxygen content shall be greater than 19.5% and less than 23.5%. Testing for the presence of residual toxic substances must be carried out if such substances are suspected. After carrying out the previous procedures when entering an enclosed space, the following guidelines must be followed. Ensure that the gas level is monitored while the worker is in the room. A person is required to constantly monitor the development of the situation and to wear appropriate protective equipment to be protected in the event of a hazard. The worker must wear a protective belt for the whole body when working in an enclosed space. Adequate ventilation must be established and maintained until the work is completed. There must be no steam, chemicals or other hazardous substances or flammable liquids in the enclosed space. All flammable materials should be stored outside the enclosed space [14].

3.3. Hazards for employees in the titanium alloys production

In the metalworking industry, every piece of equipment or tool poses a potential danger to the worker. An even greater hazard is posed if protective equipment that complies with the relevant regulations, standards or measures is not used at work. Hazardous places are places and spaces where the following can occur due to dangerous movements: Entrapment, cuts, entrapment by rotating parts, cuts, electric shocks, harmful effects of hazardous substances, etc. Hazardous movements are defined as movements of tools, shafts, power transmissions, etc. that can create hazardous places or spaces. A hazardous area is defined as a specific place or space where injuries may occur if certain parts of the body or clothing are caught by the moving parts of the equipment [16].

3.4. Hazards from electrical current

The danger of electric current is imminent when a person is connected to an electric circuit during which a current of a certain strength flows through his body. The extent of the consequences depends on the strength of the current and the duration of its passage through the body. The passage of electric current through the human body causes burns, which may be external or internal, destruction of blood plasma, muscle spasms, nervous system disorders and, in the worst case, death. Electrical hazards arise from direct contact with or proximity to live parts. Hazards to the worker are also possible due to a defect in, for example, the insulation or the passage of current through the earthing devices, or due to the occurrence of an electric arc. Such hazards most frequently occur at switches, electrical cables, plug-in devices and electrical mobile consumers.

Therefore, protective measures against electric shock must be taken in accordance with existing regulations and standards. This refers to protective measures on all electrical installations, equipment and apparatus, regardless of the type of premises or room in which they are installed. This is achieved by using suitable equipment and materials for electrical installations and by applying rules of conduct in accordance with the standards and regulations [16].

3.5. Technical measures of protection

At work, all machinery, equipment, devices and other tools used must be fitted with a protective device to protect workers who handle or come into contact with them from possible injury. This is because the guard protects the worker's hand during work, i.e. the guard protects the hand from possible breakage, spillage, splashing,

fire, corrosion, poisoning, hazardous radiation, etc. The guards are built into the tool and set to stop the drive in the event of a malfunction, thus preventing possible injury to the worker. If the safety risk cannot be sufficiently prevented or reduced by collective protective measures or technical measures and organisational measures and procedures, measures relating to the worker are used. These measures enable the worker to control hazards through instruction in the safe operation of machinery or work equipment, vocational training and the use of personal protective equipment [16].

3.5.1. Personal protection equipment

Personal protective equipment is used by workers at work when it is not possible to eliminate risks to safety and health and when the employer cannot sufficiently reduce the risks by applying the basic rules of safety at work or by an appropriate work organisation. Personal protective equipment is divided into protective equipment for the head, eyes and face, hearing, respiratory organs, hands (protective gloves protect hands from possible mechanical, thermal, chemical and other hazards), legs (to protect against cold, against heavy objects falling on legs, against punctures and cuts, against slipping, against oils, greases and chemicals, e.g. safety shoes, safety boots). There is also equipment to protect against ionising radiation, falls from height/depth and adverse climatic conditions [16].

4. Casting of titanium alloys for use in dentistry

In dentistry, titanium is used to make crowns and bridges. It does not cause allergic reactions, is fracture-resistant and has pronounced biocompatibility. Titanium alloys are being introduced in dentistry as an alternative to gold alloys after the price of gold has risen considerably [17] [18].

There are still no titanium alloys exclusively for casting, nor is there a single aggregate for casting. Titanium casting can be improved by adding chromium (Cr) or palladium (Pd), which reduce the melting interval. There are ten different titanium casting processes: Pressure/vacuum casting in separate melting and casting chambers, pressure/vacuum casting in one chamber and centrifugal casting in a vacuum, in an argon atmosphere or in a combination of two atmospheric media: argon and vacuum. Most often, casting is done in an atmosphere of protective argon gas. Pure argon prevents contamination of the molten alloy, does not cause porosity and does not change the microstructural appearance of the casting, but it does contribute to better mechanical properties and thus to clinical applications. The purity of the argon does not influence the microhardness of the titanium casting and its alloy. Pure titanium is also used in dentistry due to its high corrosion resistance, excellent biocompatibility and good mechanical properties. The contamination of titanium with oxygen, hydrogen and nitrogen during the casting process leads to a change in its physical and mechanical properties. Its reactivity with oxygen at high temperatures and its low density complicates the casting process. The surface of titanium castings has a layered structure as a result of the reaction with the moulding materials. In order to obtain high-quality dental casting, the difference between the dimensional accuracy and the surface reaction of pure titanium should not be too great. Relatively high temperatures of the investment casting mould can cause sufficient thermal expansion, but can also lead to considerable oxidation of the surface. Porosity, casting contraction and surface roughness are often the result of casting. Contamination of titanium and its alloys with oxides, hydroxides and nitrites during casting changes their properties. Tensile strength and stiffness increase, while ductility decreases. In terms of dynamic resistance, the increase in tensile strength is positive, but the decrease in elongation and the resulting microcracks have a negative effect [18].

5. Conclusion

Titanium alloys have many good properties, but also some shortcomings. They can be produced by an electric arc melting and casting. During this process, hazards can occur that endanger the production process itself and the safety of those involved in the titanium alloy production process. Possible hazards are fire, explosion, lack of oxygen, etc. To prevent these hazards, it is necessary to invest in equipment and new technologies, train employees, etc. Because of the expected increase in the use of titanium alloys, especially in dentistry, it is necessary to comply with the relevant regulations during production to avoid undesirable consequences.

6. References

[1] C. Leyens; Manfred Peter, *Titanium and Titanium Alloys*. (*WILEY-VCH Verlag GmbH & Co. KGaA, Weinheim, 2003*)

[2] F. A. Anene, C. N. Aiza Jaafar, I. Zainol, M. A. Azmah Hanim, M. T. Suraya, Proc. Inst. Mech. Eng. Part C J. Mech. Eng. Sci. 235, 19 (2021)

[3] G. Senopati, R. A. Rahman Rashid, I. Kartika, S. Palanisamy, Metals, 13, 2 (2023).

[4] M. R. Akbarpour, H. M. Mirabad, A. Hemmati, H. S. Kim, Prog. Mater. Sci., 127 (2021)

[5] R. Chávez-Vásconez, S. Lascano, S. Sauceda, M. reyes-Valenzuela, C. Salvo, R. V. Mangalaraja, F. J. Gotor, C. Arévalo, Y. Torres, Materials, 15, 1 (2022)

[6] J. A. Ballor, T. Li, F. Prima, C. J. Boehlert, A. Devaraj, Int. Mater. Rev. (2022)

[7] S. Fashu, M. Lototskyy, M. W. Davids, L. Pickering, V. Linkov, S. Tai, T. Renheng, X. Fangming, P. V. Fursikov, B. P. Tarasov, Mater. Des. 186 (2020)

[8] R. L. Saha, K. T. Jacob, Def. Sci. J. 36, 2 (1986)

[9] K. Suzuki, Met. Mater. Int. 7, 6, (2001)

[10] S. Y. Sung, Y. J. Kim, Mater. Sci. Forum 539–543 (2007)

[11] H. Agripa, I. Botef, *Modern Production Methods for Titanium Alloys: A Review* (IntechOpen, Amsterdam, 2019)

[12] Y. Y. K. Takanashi, Nippon STEEL Tech. Rep., no. 128, (2022)

[13] B. Xue, L. Yang, Y. Guo, F. Chen, S. Wang, F.Zheng, Z. Yang, Metals 11, 5 (2021)

[14] E. Poulsen, Jom 52, 5 (2000)

[15] S. Ferguson, N. Zsamboky, Iron Steel Technol. 14, 1 (2017)

[16] L. Protulipac, O*pasnosti i mjere zaštite u metalnoj industriji* (Veleučilište u Karlovcu, Karlovac, 2015)

[17] Lj. Slokar, J. Pranjić, A. Carek, Holist. Approach to Environ. 7, (2017)

[18] C. C. Hung, P. L. Lai, C. C. Tsai, T. K. Huang, Y. Y. Liao, Mater. Sci. Eng. A 454–455 (2007)

Optimization of the distribution of spherical granules at the formation of composite structures

Georgi Evt. Georgiev*, Lyuben Lakov, Krasimira Toncheva, Bojidar Jivov

Bulgarian Academy of Sciences, Institute of Metal Science, Equipment and Technologies with Hydro- and Aerodynamics Centre "Acad. Angel Balevski", 67 "Shipchenski prohod" Blvd., 1574 Sofia, Bulgaria, e-mail: evtimovg@abv.bg

Abstract:
On the basis of separate fractions of granular foam glass and inorganic binders, various modifications of heat-insulating composite material have been developed. A promising opportunity for potential application of the material is the preparation of composite elements and profiles suitable for installation around doors and windows during the construction or reconstruction of buildings. In connection with the study of the possibilities for optimal distribution of the granules, various options for their arrangement have been analyzed and evaluated. The mathematical tools of stereometry and 3D computer modeling were used. Visualizations of the obtained structures are presented and their compactness is evaluated. Recommendations are made for the ratio between the sizes and quantities of the granules used in order to achieve maximum density.

***KEYWORDS**: COMPOSITE MATERIALS, GRANULAR STRUCTURES, MATHEMATICAL MODELING, COMPUTER SIMULATION*

Introduction

With the intensive development of industrialization and increased consumer activity, the generated quantities of industrial and household waste materials are growing significantly [1-3]. At the same time, the presence of various waste products of different origins inevitably provokes the emergence of a number of environmental, organizational and infrastructural problems related to their collection, temporary storage, transportation and long-term disposal, together with the regulatory requirements [4]. Significant difficulties are created by waste materials that are practically non-degradable in a natural environment within a long period [2,4]. A current and cost-effective approach to partially overcome the existing problems is the use of waste products as raw materials in the production of various products [5-12]. Due to its specific physicochemical and mechanical characteristics [5,13-17], considerable durability and chemical resistance, vitreous waste materials (mainly silicate glass) are considered as a full-fledged production raw material. Main sources for providing the necessary quantities of waste glass are the existing quantities of household waste (mainly standard glass packaging and others) or production waste from regular production of the glass industry [16]. Effective technological solutions have been developed for the recycling of vitreous waste raw materials [5,16,18-22] and the production of foam glass materials in the form of various products (panels, profiles, foam glass gravel, granules, etc.). Products made of monolithic foam glass [16] are applicable for heat and sound insulation of residential, public and industrial buildings and thermal insulation of pipelines, various facilities, production units and others. Foam glass gravel is used in landscape architecture and in the implementation of road construction activities. Different fractions of foamed glass granules [23] are applicable in stabilizing soil layers, building drainage systems, forming insulating layers from light loose foam silicate aggregates and others. A promising alternative for the potential use of foam silicate granules [24] is their application as substitutes for some traditional lightweight additive materials in the preparation of heat-insulating and structural-heat-insulating lightweight concretes.

On the basis of granular foam glass (with a cellular structure) and inorganic binders (Portland cement), various modifications of an innovative non-flammable and waterproof composite material [25-27], applicable for the preparation of various heat and sound insulation boards, profiles and other products. An experimental methodology was created for the preparation of trial samples [25] by applying a series of technological stages: preparation of cement solution, introduction of separate fractions of foam granules to the cement solution and homogenization, placement of the resulting mixture in formwork forms, technological downtime, release of the blanks from formwork, etc.

Due to the norms existing in modern construction to ensure energy efficiency [28-35], sound insulation and fire safety, it is of interest to further modify the developed composite and adapt its characteristics to the requirements for materials applicable for installation around doors and windows in the implementation of construction and repair activities. The main possibility for the potential application of the material is the molding of various composite elements and profiles, meeting the construction and technical rules and norms for ensuring safety in case of fire.

With the development of the development and the further specification of the technological parameters of the used methodology for the preparation of experimental prototypes, there is a need for a more precise selection of the individual granule fractions. The controlled and more expedient distribution of foam glass aggregates in the material allows the production of final products with pre-planned operational characteristics and an appropriate structure, consistent with the intended functional role of the products.

The present study aims to visualize and evaluate the compactness of possible composite material structures by applying the mathematical tools of stereometry and 3D computer modeling. Recommendations are proposed for the optimal ratio between the sizes and quantities of the foam silicate granules used in order to optimally distribute the volume of the samples and achieve maximum density. The obtained results allow further specification of the developed technological approach and are directly applicable when creating a detailed technological regulation for the production of products in the conditions of a semi-industrial experiment.

2. Mathematical approach

Initially, we will consider the possible structures formed by spheres of the same size.

2.1. Evaluation of structures with equal volume spheres

In the beginning, we will consider the simplest possible arrangement structure of spherical granules. One of its structural cells is shown in Fig.1.

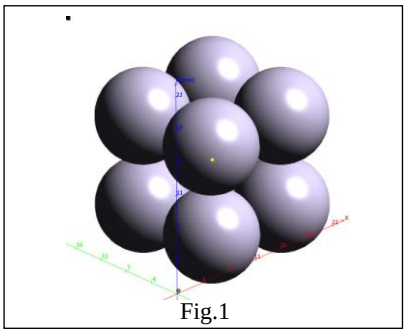

Fig.1

Fig.2 shows a structure obtained by multiplication of such a unit cell into a cube "C" with side size a =10d.

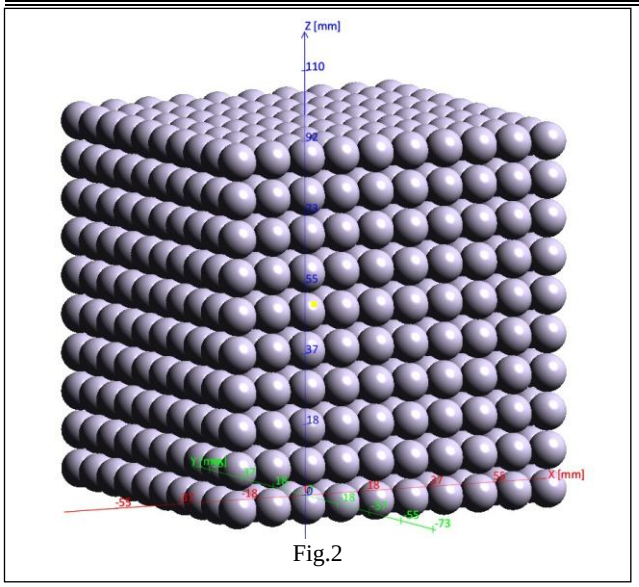

Fig.2

The ratio of the total volume of the spheres into the volume V of "C" ($V = 10^3 d^3$) is calculated to be K= 0.516 or about 52%.
The number of spheres in "C" is N_r = 1000. Closer packing could be obtained if the base cell of the first layer is chosen to be as in Fig.4.

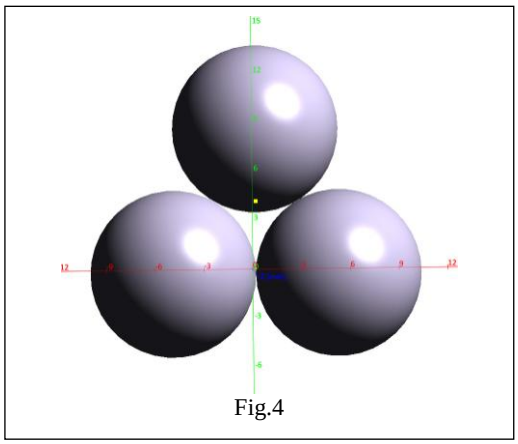
Fig.4

Multiplied in the first layer of the cube "C", it looks like the arrangement in Fig.5.

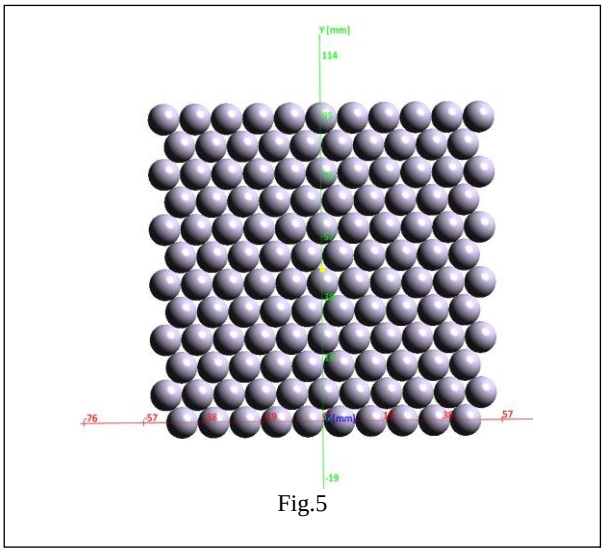

Fig.5

By translating this layer along the vertical axis, we get the structure in the entire cube "C" - Fig.6

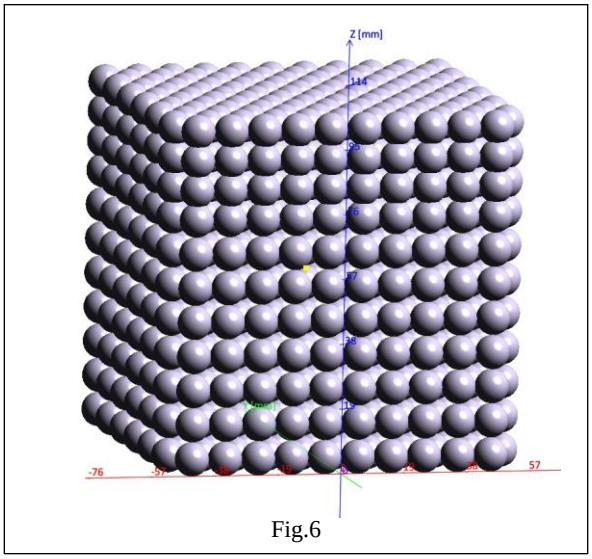

Fig.6

With this way of packing, the ratio of the total volume of the spheres to the volume of "C" results in K= 0.608 or about 61%, i.e. an increase of about 9% was found compared to the previous structure. The number of spheres here is N_r = 1161.

Maximum density using spheres of the same size can be achieved if a simple 3D structural cell of the type shown in Fig.7 is used.

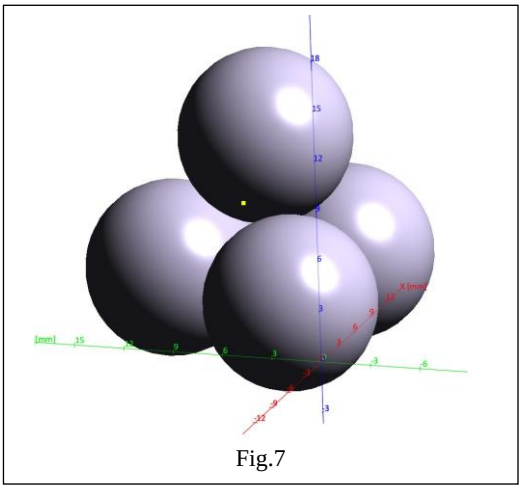
Fig.7

Multiplied in the "C" cube, this arrangement looks like that in Fig.8.

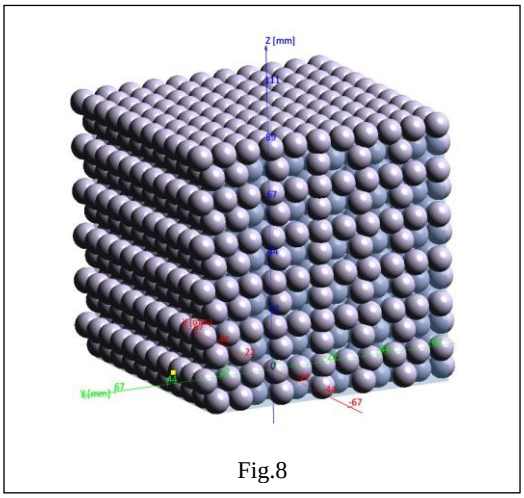

Fig.8

Its packing density is characterized by the coefficient K=0.632 or 63%. With this result, an increase in the density of the granule was

found by about 2% compared to the previous one. The number of spheres in "C" is 1207.

2.2. Evaluation of structures with different spheres

A higher density compared to the structures discussed above could be achieved by adding smaller radius spheres. Thus, for example, for the structure of the type of Fig. 2 one could find the largest second-order sphere that can fill the spaces between the main spheres of radius r. The centers of the spheres of its structural cell are located at the vertices of a cube presented in Fig.9.

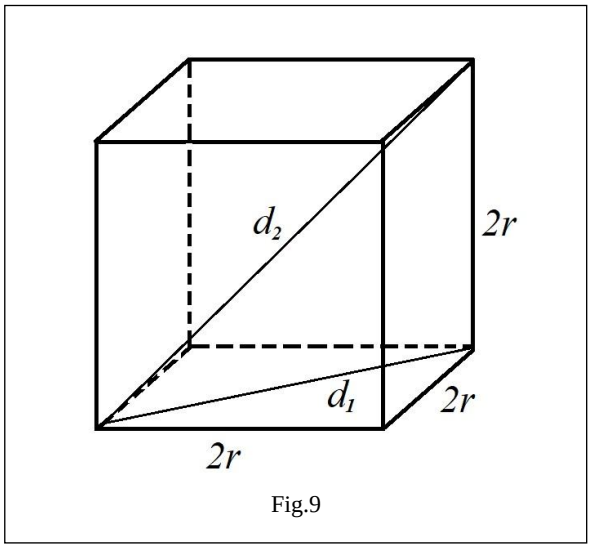

Fig.9

The sphere simultaneously touching the four spheres of the cell is the largest that can be implanted in free space, and its radius can be found as follows:

For the diameter at the base of the cube we have

$$d_1 = \sqrt{4r^2 + 4r^2} = 2r\sqrt{2}, \quad (1)$$

and for the diameter the cube

$$d_2 = \sqrt{d_1^2 + 4r^2} = 2r\sqrt{3} \quad (2)$$

then for the diameter of the maximum sphere touching the main spheres we obtain

$$D = 2r\sqrt{3} - 2r = 2r(\sqrt{3} - 1) \quad (3)$$

and respectively for the radius

$$R = r\left(\sqrt{3} - 1\right) = 0.732r. \quad (4)$$

Or about 73% of the radius of the main sphere. This sphere in 3D is depicted in Fig.10.

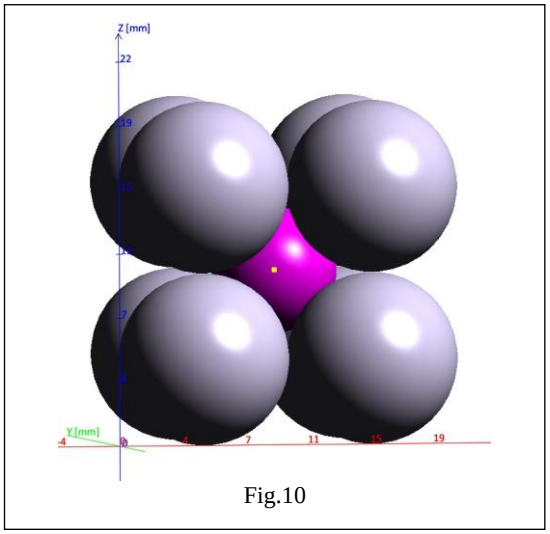

Fig.10

Multiplying this cell into the volume of the cube "C" results in the structure depicted in Fig.11.

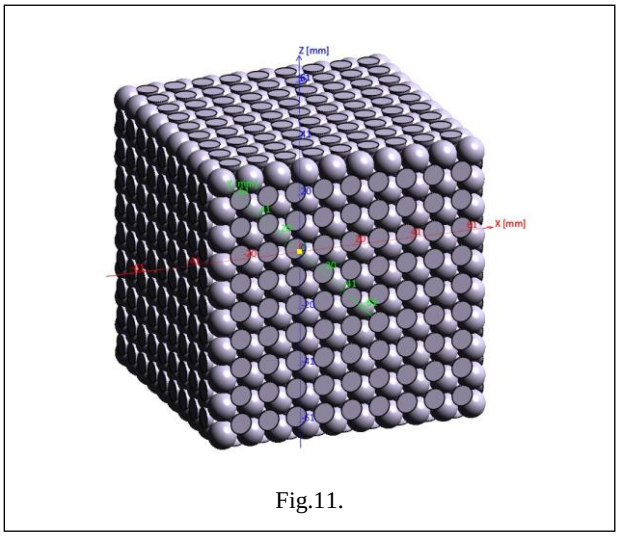

Fig.11.

Here the ratio of the volume of the granules to the volume of the cube "C" is already K= 0.712 or 71%. This is about 8% higher density than the super-compact structure with identical spheres. In this case R/r = 0.732 and N_r = 964, N_R = 1000, N_r/N_R = 0.964.

An analogous approach could be applied to the structure of Fig. 4, Fig. 5 and Fig. 6. In it, the main spatial structural cell consists of six main spheres, shown in Fig.12.

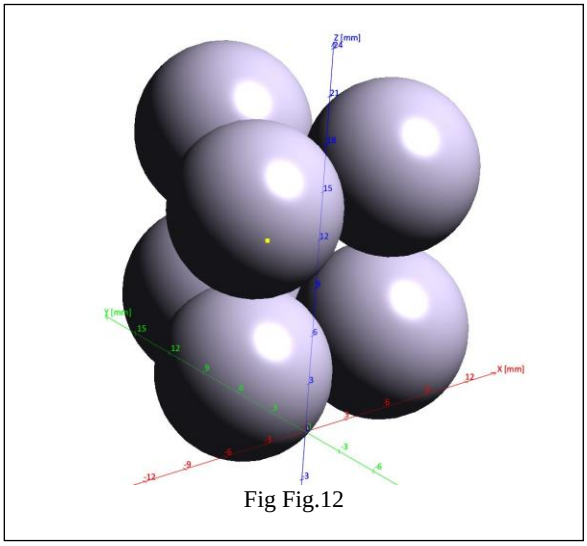

Fig Fig.12

The centers of these spheres form a regular triangular prism shown in Fig.13.

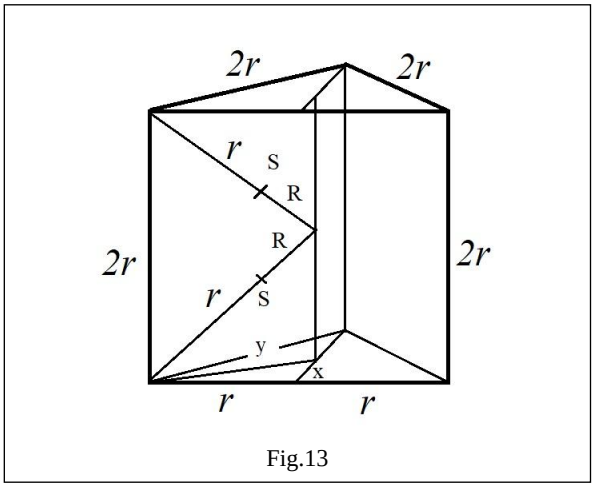

Fig.13

The radius R of the tangent sphere to the six spheres can be calculated by the following algorithm

$$x = r\frac{\sqrt{3}}{3}, \qquad y = 2x = 2r\frac{\sqrt{3}}{3} \tag{5}$$

$$s = r + R = \sqrt{r^2 + y^2} = r\sqrt{\frac{7}{3}} \tag{6}$$

therefore

$$R = s - r = r(\sqrt{\frac{7}{3}} - 1). \tag{7}$$

The result obtained for the radius according to the last formula for the structure of Fig. 4, Fig. 5 and Fig.6 is illustrated in Fig.14.

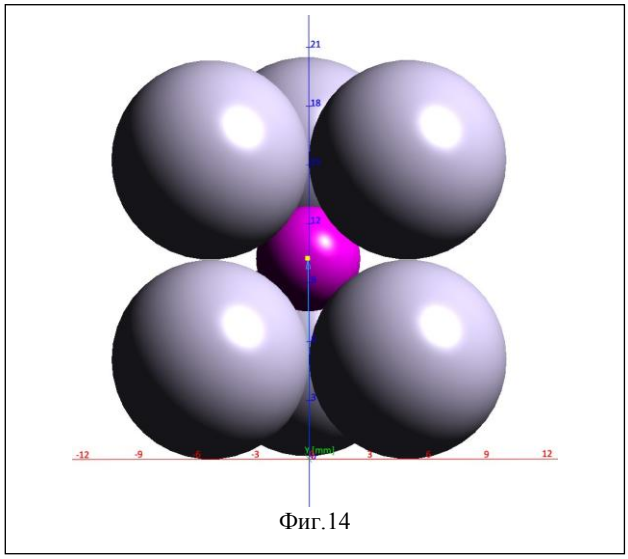

Фиг.14

From the last formula, the ratio of the radii is R/r=√(7/3)-1 = 0.528 or 53%. Fig. 15 shows one layer of this structure, and Fig. 16 shows the same structure in 3D.

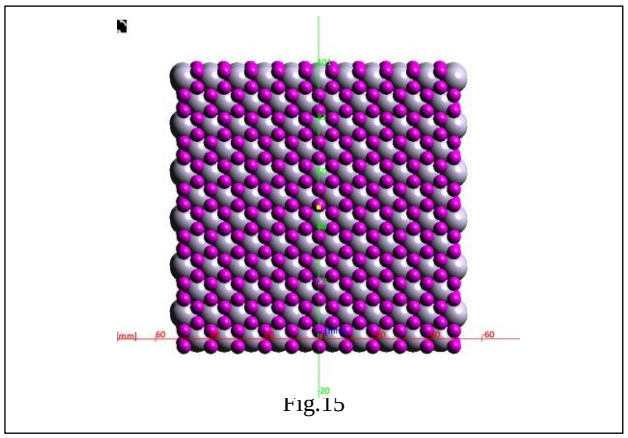

Fig.15

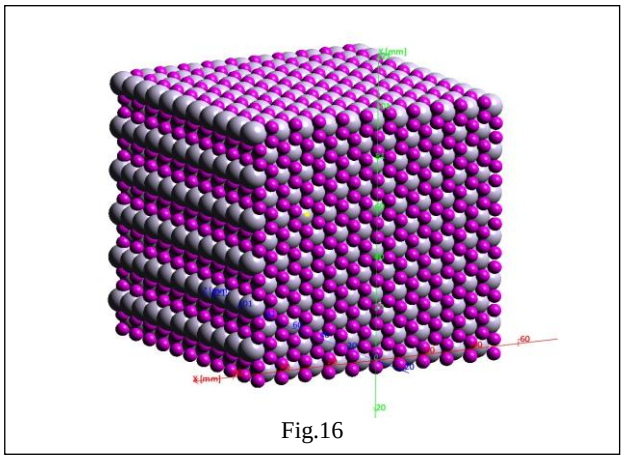

Fig.16

For the ratio of volumes in this variant, K = 0.773 or 77% is obtained. Comparison with the previous version shows a 6% increase in density. N_R = 2465, N_r = 1207, N_R/N_r = 2.042.

Next, we will investigate the possibility of compaction of the variant from Fig. 7 and Fig. 8, which showed the highest density with the same granules. For this purpose, we consider the tetrahedron with the centers of the spheres from the unit cell (Fig.7) of this structure. It is depicted in Fig.17.

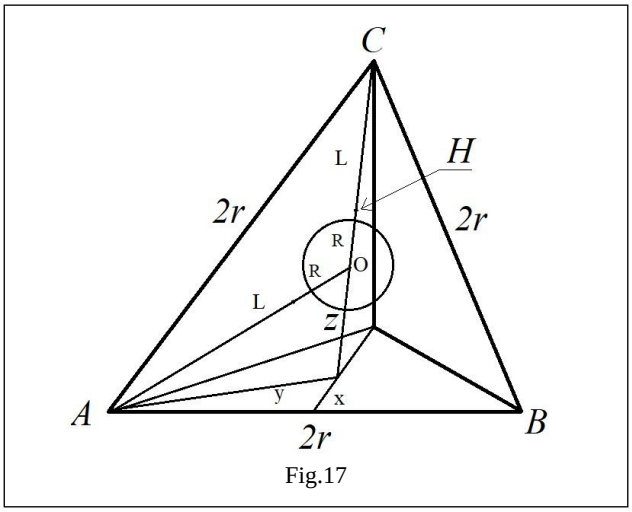

Fig.17

According to the relations in stereometry, we have

$$x = r\frac{\sqrt{3}}{3} \tag{8}$$

$$y = 2x = 2r\frac{\sqrt{3}}{3} \tag{9}$$

For the distance between between the tetrahedron center “O” and its vertices the follow equation holds

$$L^2 = y^2 + z^2 = (H - z)^2 \tag{10}$$

From where for z we obtain

$$z = \frac{1}{\sqrt{6}} \tag{11}$$

From (9), (10) and (11) for the radius of the inscribed sphere R we get

$$R = L - r = r(2\sqrt{\frac{2}{3}} - \frac{1}{\sqrt{6}} - 1) \tag{12}$$

An image of this sphere in the unit cell of the structure is shown in Fig. 18.

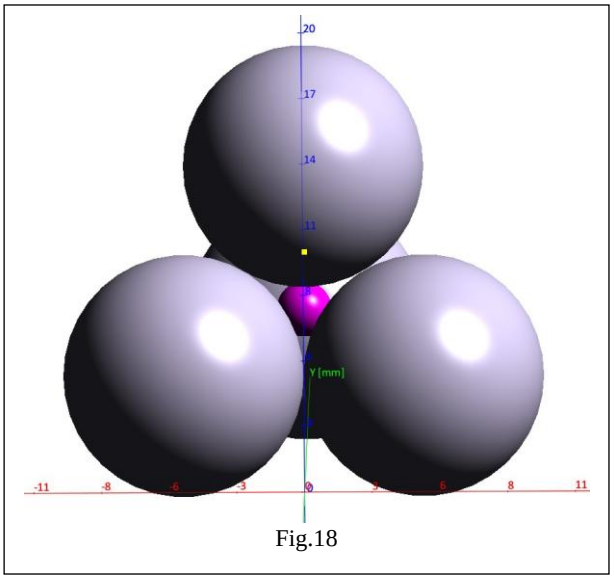

Fig.18

Its radius is in the ratio $\frac{R}{r} = 2\sqrt{\frac{2}{3}} - \frac{1}{\sqrt{6}} - 1 = 0.225$ or 22.5% to that of the main sphere. A single layer of the structure is presented in Fig.19, and as 3D in Fig.20.

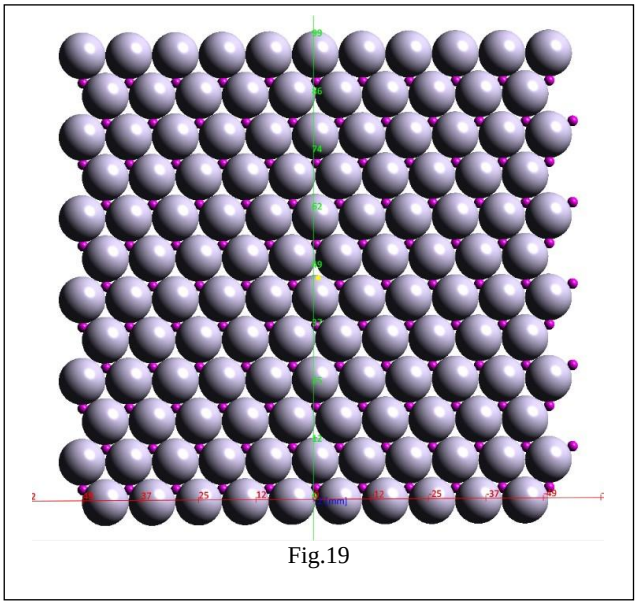

Fig.19

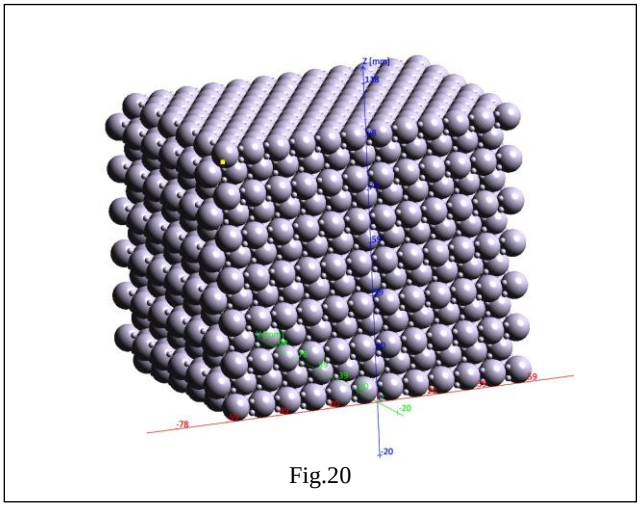

Fig.20

For the coefficient K in this case the value of 0.738 or 74% is obtained. Comparison with the same arrangement with identical spheres in Fig.8 shows an increase in density of 11%. In this case R/r = 0.225 and N_r = 1207, N_R = 9014, N_R/N_r = 7.468.

Conclusion

The obtained results for the compactness of granular structures formed by spherical granules indicate a logical increase in the density of the structure with a more compact arrangement of the spheres. The logical increase in density when filling the voids with spheres of smaller sizes is also observed. It should be noted that the results were obtained for the maximum possible sizes of the embedded spheres. The structure with the highest density of 77% was found. It has been established that it is not reached with the most compact arrangement of the main spheres (Fig. 8), but in that like in Fig. 16 with a ratio of the radius of the embedded to the main spheres of 53%.

The authors hope that the obtained results will be useful in the optimization of composite materials based on spheroidal granules developed for the various practical applications.

Acknowledgments

The authors express their gratitude to the National Innovation Fund and the Bulgarian Small and Medium Enterprises Promotion Agency at the Ministry of Economy of the Republic of Bulgaria for financing a scientific-applied project / Contract No. 13 ИФ-02-21/12.12.2022 between the contracting authority BSMEPA and contractors - beneficiary "MAG" LTD with partner IMSETHA "Acad. A. Balevski" - BAS.

References

1. R. Basu, "Solid Waste Management-A Model Study", Sies Journal of Management, 6, 2009, pp. 20-24.

2. L. Giusti, "A review of waste management practices and their impact on human health", Waste Management, 29(8), 2009, pp. 2227-2239.

3. A. Demirbas, "Waste management, waste resource facilities and waste conversion processes", Energy Conversion & Management, 52(2), 2011, pp. 1280-1287.

4. E. Amasuomo, J. Baird, "The Concept of Waste and Waste Management", Journal of Management and Sustainability; Vol. 6, No. 4; 2016, pp. 88-96.

5. L. Lakov, K. Toncheva, A. Staneva, T. Simeonova, Z. Ilcheva, "Composition, synthesis and properties of insulation foam glass obtained from packing glass waste", Journal University of Chemical Technology and Metallurgy 48, 2, 2013, pp. 125–129.

6. A. P. M. Velenturf, P. Purnell, "Resource Recovery from Waste: Restoring the Balance between Resource Scarcity and Waste Overload", Sustainability, 2017, 9, 1603, pp. 1-17.

7. G. Degli Antoni, G. Vittucci Marzetti, "Recycling and waste generation: an estimate of the source reduction effect of recycling programs", Ecol. Econ., 161, 2019, pp. 321–329.

8. A. Trinca, V. Segneri, T. Mpouras, N. Libardi, G. Vilardi, "Recovery of Solid Waste in Industrial and Environmental Processes", Energies, 2022, 15, 7418, pp. 1-5.

9. F. Medici, "Recovery of Waste Materials: Technological Research and Industrial Scale-Up", Materials, 2022, 15, 685, pp. 1-3

10. M. Aleksandrova, V. Petkov**,** V. P. Korzhov, I. S. Zheltyakova. "Study the influence of immersion in the synthesis of thin layers on a composite substrate". International Scientific Journal INDUSTRY 4.0, VII, 6, 2022, pp. 226-228.

11. V. Petkov, M. Aleksandrova, R. Valov, G. Mutafchieva, B. Krastev, "Investigation of microstructure of chromium coating with nanodiamonds deposited on 316L steel", International Journal "NDT Days", v. 5, № 4, 2022, pp. 211-218.

12. G. Mutafchieva, "Technological development of lighting fixtures in the field of silicate design", Collection reports, Design & applied arts - Sofia, NAA, 2018, pp. 138-144.

13. N. Rivier, "Theory of Glass", Revista Brasileira de Flsica, Vd. 15, No 4 (1985) 311-378.

14. L. O. Hedges, R. L. Jack, J. P. Garrahan, D. Chandler, "Dynamic Order-Disorder in Atomistic Models of Structural Glass Formers", *Science*, vol. 323, Issue 5919, 2009, pp. 1309-1313.

15. I. M. Kalogeras, H. E. Hagg Lobland, "The nature of the glassy state: Structure and glass transitions", Journal of Materials Education, vol. 34/3-4, 2012, pp. 69-94.

16. K. Toncheva, „Creation and research of a blowing section of a system for obtaining a continuous strip of foam glass", PhD Dissertation for the award of the educational and scientific degree "Doctor", Specialty: "Technologies, machines and systems of foundry production", code 02.01.18, Sofia, 2014, p. 168.

17. A. Takada, R. Conradt, P. Richet, "Residual entropy and structural disorder in glass: A review of history and an attempt to resolve two apparently conflicting views", J. Non-Cryst. Solids, 429, 2015, pp. 33–44.

18. Research project, Contract for financial assistance BG161PO003-1.1.06-0094- C001/07.12.2012 with beneficiary "Promstroyproekt" LTD and partner IMSETHA "Acad. A. Balevski" - BAS, "Creation and research of a new technology and horizontal model for the production of composite thermal insulation

materials in the form of pieces (large granules) of foam glass from glass waste", Project status - completed.
19. I. Chorbov, K. Toncheva, L. Lakov, "Device for obtaining foam glass granules", Patent № 66666 / 06.06.2012. Status-Valid, Place of application Bulgaria.
20. L. Lakov, K. Toncheva "Device for obtaining foam glass", Patent № 66903 B1, 2019, Status - Valid, Place of application Bulgaria.
21. I. Chorbov, L. Lakov, K. Toncheva, L. Drenchev, N. Guo, H. Shi, "Device for obtaining foamed granules from composite material", Patent application № BG /P/2020/113247 dated 21.10.2020, Status - in examination, Place of application Bulgaria.
22. I. Chorbov, L. Lakov, K. Toncheva, L. Drenchev, N. Guo, H. Shi, "Device for obtaining a continuous plane of foamed composite material", Patent application № BG/P/2020/113248 dated 21.10.2020, Status - in examination, Place of application Bulgaria.
23. M. Marinov, L. Lakov, K. Toncheva, "Granulated foam glass. Production. Physical and mechanical characteristics", *Proceedings of the* XIII Scientific congress on machines, technologies and materials 2016, 14-17 September, 2016, Varna, Bulgaria, Part II, 2016, pp. 56-58.
24. L. Lakov, B. Jivov, Y. Ivanova, S. Yordanov, K. Toncheva, "Alternative possibilities for application of foamed silicate materials", International Scientific Journal "Machines. Technologies. Materials" Issue 1/2021, pp. 25-27.
25. L. Lakov, B. Jivov, M. Aleksandrova, Y. Ivanova, K. Toncheva, „An innovative composite material based on sintered glass foam granules", Journal of Chemical Technology and Metallurgy, 53, 6, 2018, pp. 1081-1086.
26. Y. Ivanova, T. Partalin, L. Lakov, B. Jivov, "Airborne sound insulation of new composite wall structures", MATEC Web of Conferences 145, 2018, 05013, NCTAM.
27. L. Lakov, L. Drenchev, D. Nazarski, "Composite thermal insulation material", Patent № 66960 B1, 2019, Status-valid, Place of application Bulgaria.
28 .D. Nazarski, "Building Insulations", Publishing House "St. Naum ", Sofia, 2004.
29 .R. Savov, D. Nazarski, "Energy Efficiency, Thermal insulation systems of buildings, Publishing house", "ABC Technic", Sofia, 2006.
30. B. P. Jelle, "Traditional, state-of-the-art and future thermal building insulation materials and solutions - Properties, requirements and possibilities", Energy and Buildings, Vol. 43, Issue 10, 2011, pp. 2549-2563.
31. N. Pargana, M. D. Pinheiro, J. D. Silvestre, J. Brito, "Comparative environmental life cycle assessment of thermal insulation materials of buildings", Energy and Buildings, Vol. 82, 2014, pp. 466-481.
32. S. Schiavoni, F. Dʹ Alessandro, F. Bianchi, F. Asdrubali, "Insulation materials for the building sector: A review and comparative analysis", Renewable and Sustainable Energy Reviews, Volume 62, 2016, pp. 988-1011.
33. L. Aditya, T. M. I. Mahlia, B. Rismanchi, H. M. Ng, M. H. Hasan, H. S. C. Metselaar, Oki Muraza, H. B. Aditiya, "A review on insulation materials for energy conservation in buildings', Renewable and Sustainable Energy Reviews, Vol. 73, 2017, pp. 1352-1365.
34. B. Orlik-Kożdoń, "Assessment of the application efficiency of recycling materials in thermal insulations'', Construction and Building Materials, Vol. 156, 2017, pp. 476-485.
35. C. Hill, A. Norton, J. Dibdiakova, "A comparison of the environmental impacts of different categories of insulation materials", Energy and Buildings, Vol. 162, 2018, pp. 12-20.

Abrasive wear of aluminum alloys produced without and with foaming

Angel Velikov[1], Mara Kandeva[2], Boyko Krastev[1], Valentin Manolov[1]

[1]Institute of Metalscience, Equipment and Technologies with Center of Hydro- and Aerodynamics "Acad. A. Balevski" - Bulgarian Academy of Sciences, Sofia, Bulgaria
[2]Technical University - Sofia

Abstract: A methodology has been developed for obtaining of porous castings from Al and aluminum A356 alloy. The methodology includes introduction of Ca into the melt for viscosity increasing and homogenization by mechanical stirring. This is followed by addition of TiH_2, homogenization, subsequent formation of the porous structure and crystallization. Tests were carried out on specimens of the castings involving abrasive wearing under dry friction conditions on a surface with hard-attached abrasive particles.

1. Introduction

The production of aluminum and aluminum alloys of high porosity, or so called foams, is the subject of the work of a number of researchers. These materials have a low density with a large amount of distributed pores. They are used for thermal insulation and fire protection, as well as sound insulation and liquid filtration.

The porous castings have been obtained from melt of aluminum or A356 alloy by a method, involving melting of metal ingot in a crucible resistance furnace,, at T=953 K. 1 wt % Ca is introduced into the alloy and mechanical stirring is carried out. Following, pouring the melt into a heated thin-walled metal mold, introducing of 1.6 wt % oxidized TiH_2, intensive mechanical stirring, foaming and cooling of the foam material [1]. On Fig. 1 and Fig. 2 are shown photographs of samples, foamed to the above mentioned manner of pure aluminum and A356 alloy. The foamed aluminum has a porosity of 89.19%, and the A356 alloy - with 88.3%.

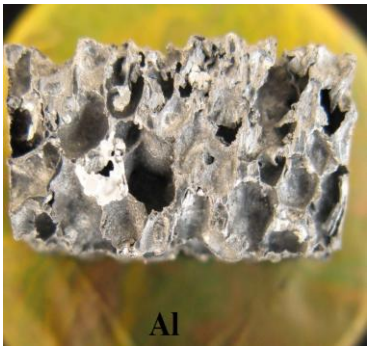

***Fig.** 1. Specimen of pure aluminum*

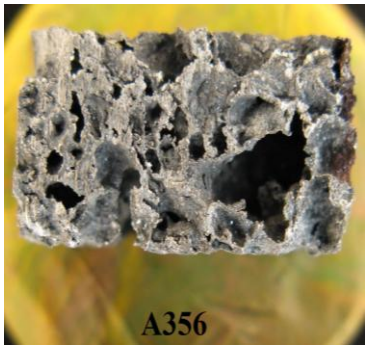

***Fig. 2**. Specimen of A356 alloy*

Studies on tribological properties, evaluated by dry and lubricated sliding wear tests are known [2]. In another study [3], dolomite CaMg $(CO_3)_2$ was used for foaming. The obtained specimens were tested by means of a pin-on-disk test, which essentially represents a simple movement of the tested sample on a disk [3].

The aim of the present work is to investigate the wear characteristics of pure aluminum and aluminum alloys produced without and with foaming under conditions of dry friction on a surface with firmly attached abrasive particles.

2. Materials and technology

Four types materials, united in two series: A and B have been studied. Series A contains two types of materials obtained by foaming: pure aluminum with foaming (Al - P) and alloy with foaming (AlSi7Mg - P). The letter P marks the presence of pores in the alloy, obtained during the foaming of the melt. The second series B includes the same materials, but obtained without foaming. The numbering of the specimens and their designation are shown in Table 1.

Table 1: Designation of the tested materials

Series	Number of the specimen	Designation of the materials	Description
A	1	AlSi7Mg - P	Alloy obtained by foaming of the melt
	2	Al - P	Pure aluminum obtained by foaming of the melt
B	3	AlSi7Mg	Alloy obtained without foaming of the melt
	4	Al	Pure aluminum without foaming of the melt

3. Experimental procedures

The study of the abrasive wear parameters of the coatings is carried out in dry friction conditions by sliding on a surface with firmly attached abrasive particles with a "Thumb-disk" tribotester. The functional scheme of the device is shown in Fig.3.

The coated test specimen 1 is fixed in the holder 2 of the loading head 8, so that its front surface forms a planar contact with the abrasive surface 3 fixed firmly on a horizontal disk 4. All the specimens are of have the same dimensions of 10x10x25 mm.

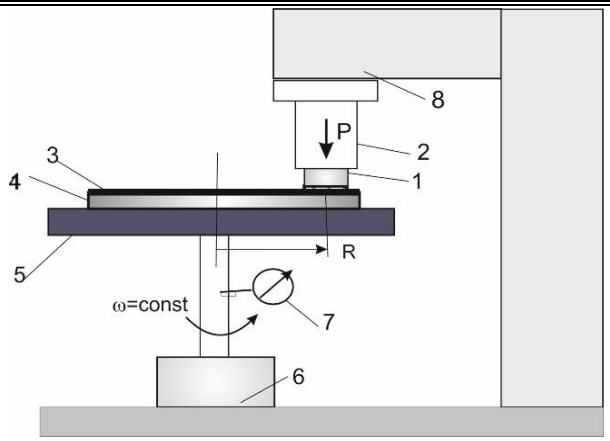

Fig. 3. Schematic diagram of abrasive wear testing on pin-disc tribometer

The disc 4 is driven by an electric motor 6 and rotates around its vertical central axis at a constant angular velocity. The normal load P is set at the center of the contact area between the specimen and the abrasive surface by means of a lever system. The friction path in number of cycles (N) is set and read by the help of tachometer 7. The abrasive surface 3 is modeled with impregnated corundum P320 with a hardness of 9.0 on the Mohs scale, thus complying with the requirement of the standard for a minimum of 60% higher hardness of abrasive than that of the coating. The investigation of all coatings was carried out under the following constant parameters of the friction mode: normal load P = 4.51 N, nominal contact area 1.0 cm^2, sliding speed 0.155 m/s; type of abrasive surface - Corundum P 320, ambient temperature 21 ^{o}C.

The methodology of the investigation consists in measuring the mass wear of the test sample through a certain friction path (number of cycles) under set constant conditions – sliding speed, load, type of abrasive surface, ambient temperature. Mass wear (m) is defined as the difference between the initial mass of the specimen and the mass of the specimen after a certain friction path, which is measured with an electronic balance WPS 180/C/2 with an accuracy of 0.1 mg. Before each mass measurement, the sample is cleaned of mechanical and organic particles, dried with ethyl alcohol to prevent the electrostatic effect. For each trial, the abrasive surface of each sample is replaced. After measuring the mass wear, the remaining wear characteristics are calculated: linear wear, wear intensity, absolute and relative wear resistance.

The intensity of abrasive wear i_a is defined as mass wear per unit path of friction L, i.e.

$$i_a = \frac{m}{L} \quad (1)$$

The intensity of abrasive wear i_a has dimension mg/m.

Path of sliding is calculated by the formula:

$$L = 2\pi RN \quad (2)$$

where R is the distance from the center of the contact pad to the axis of the disk (Fig.3).

The absolute wear resistance I_r is presented as the reciprocal value of the wear intensity, i.e.

$$I_r = \frac{1}{i_a} = \frac{L}{m} \quad (3)$$

It is a numbe, which indicates how many meters path of friction the specimen will pass, in which a mass of 1 milligram will be destroyed from the surface layer of the specimen.

Relative wear resistance $R_{i,j}$ is a dimensionless number and represents a ratio between the wear resistance of the test specimen I_r^i and the wear resistance of a specimen accepted as a standard - I_r^j, which are determined under the same friction conditions, i.e.:

$$R_{i,j} = \frac{I_r^i}{I_{r,}^j} \quad (4)$$

4. Experimental results and discussion

With the described device and methodology, tests were conducted and results were obtained for the wear parameters - mass wear, wear intensity, absolute and relative wear resistance at different number of cycles - 400, 600, 800, 1000, respectively different sliding path - 75.4 m, 112.8 m, 150.8 m, 188 m. The results for each specimen are presented in Tables 2, 3, 4 and 5.

Table 2: Mass loss, wear rate and wear resistance of the tested materials AlSi7Mg-P

Specimen № 1 - AlSi7Mg-P				
Number of cycles (N)	400	600	800	1000
Sliding distance, m	75.4	112.8	150.8	188.0
Mass loss, mg	8.5	17.4	19.8	21.4
Wear rate, mg/m	0.11	0.15	0.13	0.11
Wear resistance, m/mg	9.1	6.7	7.7	9.1

Table 3: Mass loss, wear rate and wear resistance of the tested materials Al-P

Specimen № 2 - Al-P				
Number of cycles (N)	400	600	800	1000
Sliding distance, m	75.4	112.8	150.8	188.0
Mass loss, mg	23.5	35.7	45.6	54.4
Wear rate, mg/m	0.31	0.32	0.30	0.29
Wear resistance, m/mg	3.2	3.2	3.3	3.5

Table 4: Mass loss, wear rate and wear resistance of the tested materials AlSi7Mg

Specimen № 3 - AlSi7Mg				
Number of cycles (N)	400	600	800	1000
Sliding distance, m	75.4	112.8	150.8	188.0
Mass loss, mg	6.8	8.2	10.6	11.8
Wear rate, mg/m	0.09	0.07	0.07	0.06
Wear resistance, m/mg	11.1	13.8	13.8	15.9

Table 5: Mass loss, wear rate and wear resistance of the tested materials Al

Specimen № 4 - Al				
Number of cycles (N)	400	600	800	1000
Sliding distance, m	75.4	112.8	150.8	188.0
Mass loss, mg	50.3	56.0	58.0	59.7
Wear rate, mg/m	0.67	0.5	0.38	0.32
Wear resistance, m/mg	1.5	2.0	2.6	3.2

In accordance with the data from Tables 2, 3, 4 and 5, dependences of mass wear have been constructed for all tested materials, which are presented in Fig. 4, 5, 6 and 7. On each graph are presented only linear regression equations of mass wear in dependence of path of friction $m = m(L)$.

.

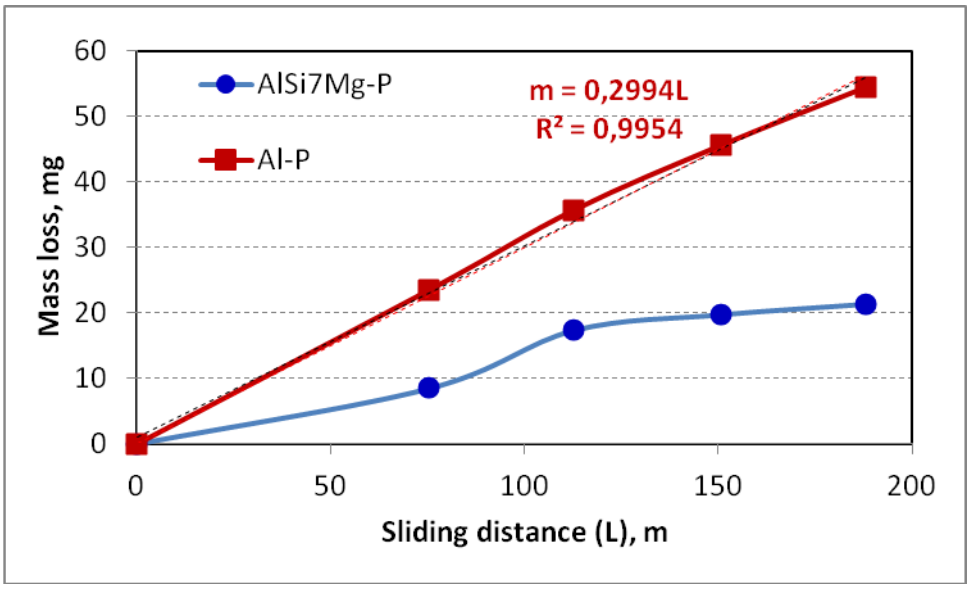

Fig.4. Dependence of the mass wear on sliding path for foamed materials

It can be seen that linearity is not unambiguously characteristic of all materials. In the case of porous materials, it appears for pure aluminum (Fig. 4), and in dense alloys it is characteristic for the aluminum alloy - (Fig. 5).

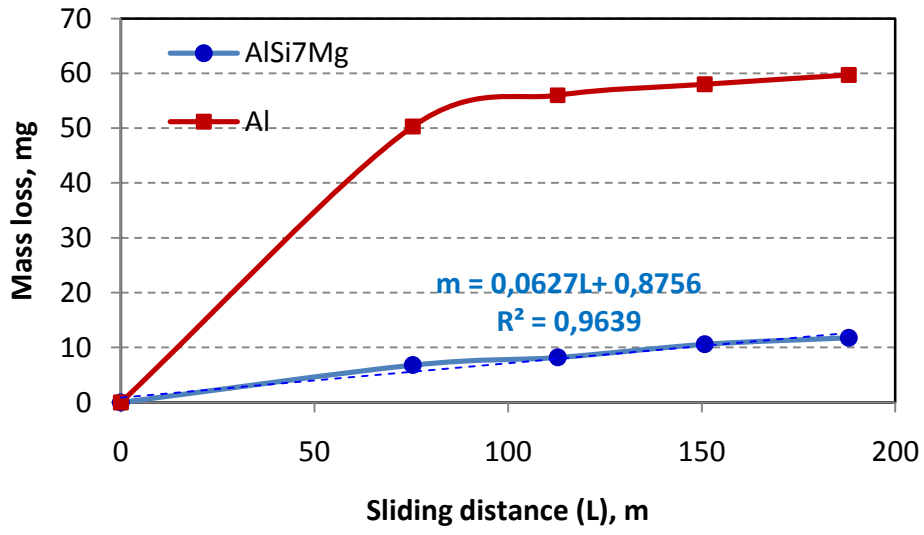

Fig.5. Dependence of the mass wear on sliding path for materials without foaming

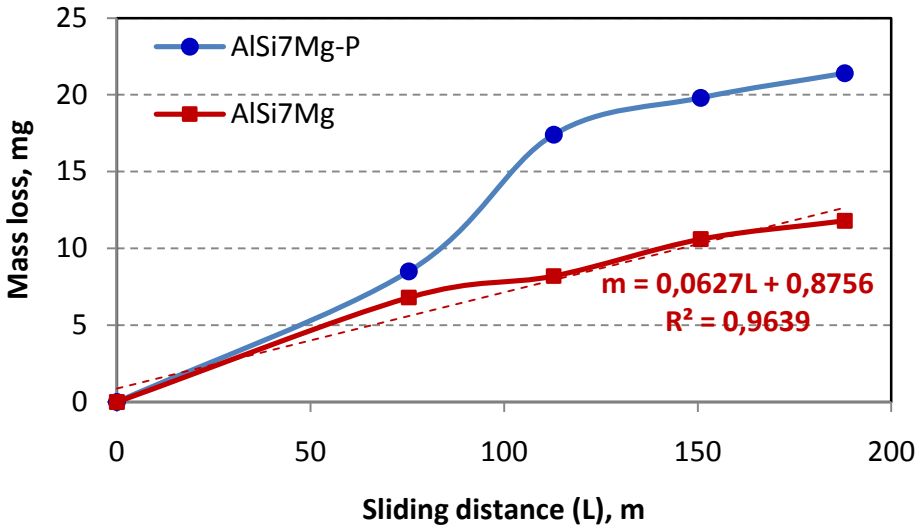

Fig.6. Dependence of the mass wear on sliding path for AlSiMg alloys, obtained without foaming

On Fig. 6 and 7 are presented the kinetic curves, respectively, of alloys without and with foaming (Fig. 6) and of solid and porous pure aluminum (Fig. 7). In the case of the first , the stable /stationary/ period of wear, i.e. linearity occurs after a friction path of 100 meters, i.e. a tempering stage is observed in contrast to the porous alloy produced by foaming (Fig.6).

The presence of a transient mode in abrasive friction without a lubricant is associated with the presence of external and internal pores. The bigger values of porous alloys compared to dense alloys is due to the smaller actual contact area of touching and the occurrence of a higher contact pressure under the same normal load P. The presence of a lubricant could change the nature of the dependence, because the presence of of pores and oil pockets, which lead to an increase in the size of the contact gap.

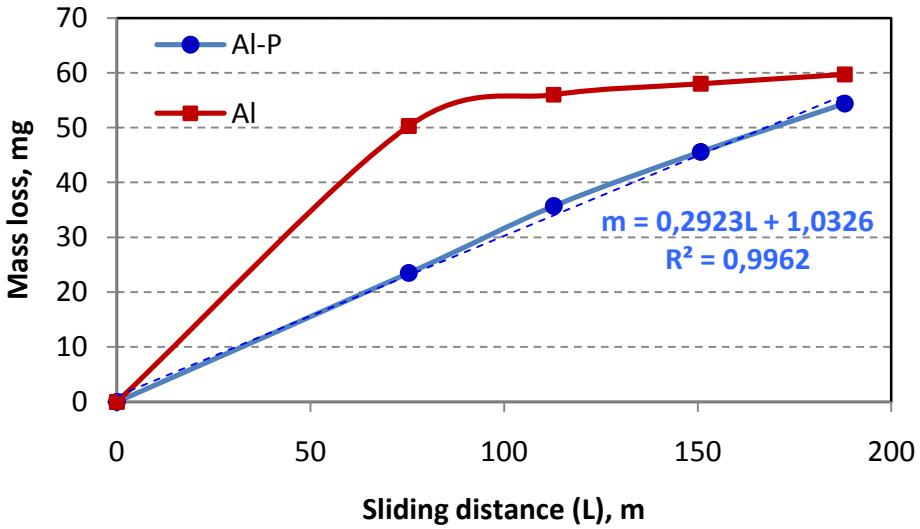

Fig.7. Dependence of the mass wear on sliding path for pure Al, obtained without and with foaming

The higher wear of solid pure aluminum can be attributed to the action of a mechanism of intense plastic deformation in dry abrasion at the larger frictional contact area. The presence of pores leads to a discrete nature of the process of plastic deformation and, accordingly, less wear.

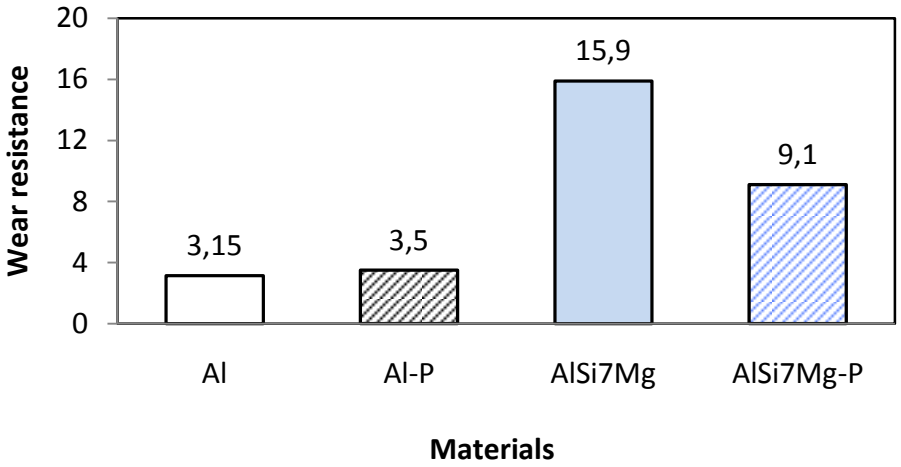

Fig. 8. Diagram of the wear resistance of tested materials

On Fig. 8 is presented a diagram of the absolute abrasive wear resistance of all tested materials. It can be seen that the wear resistance of the dense and porous alloys is higher than the wear resistance of pure aluminum. The highest is the wear resistance of dense AlSi7Mg alloy– 15.9 m/mg, and the lowest – of the dense pure Al – 3.15 m/mg.

Table 6 presents data on the relative wear resistance of the tested materials. The influence of alloying and porosity is considered for dense and porous materials.

Based on the data from Table 6, diagrams of relative wear resistance were constructed, shown in Fig. 9 and 10.

Table 6: Relative wear resistance of the tested materials

Specimen	Designation	Wear resistance for a friction path of 1000 m	Relative wear resistance	
			Influence of alloying	Influence of porosity
1	AlSi7Mg - P	9.1 m/mg	$R_{11} = 1$	$R_{13} = 0.58$
2	Al - P	3.5 m/mg	$R_{12} = 2.6$	$R_{24} = 1.11$
3	AlSi7Mg	15.9 m/mg	$R_{33} = 1$	$R_{33} = 1$
4	Al	3.15 m/mg	$R_{43} = 5.1$	$R_{44} = 1$

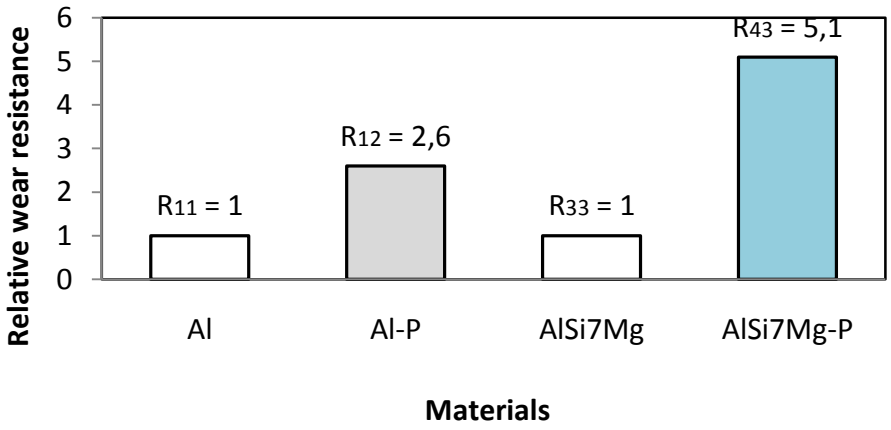

Fig.9. Influence of the alloying on the wear resistance of dense and porous materials.

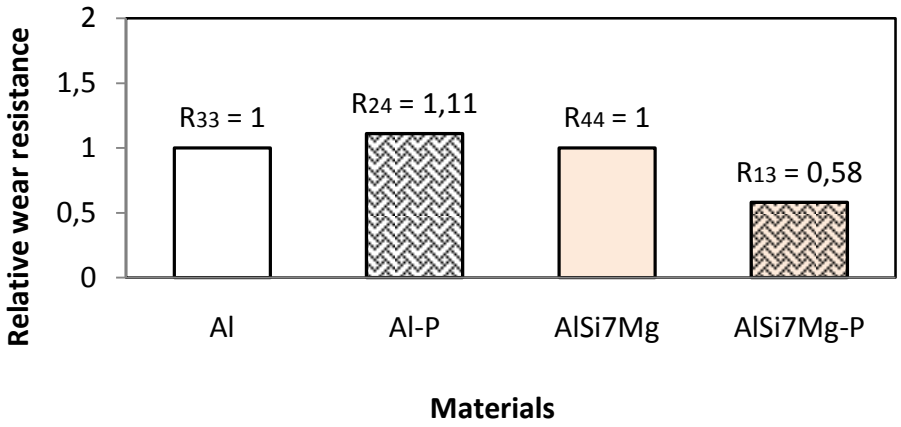

Fig.10. The influence of porosity on the wear resistance of dense and porous materials.

5. Conclusions

1. The mass wear is measured, and through it the other wear characteristics are calculated: linear wear, wear intensity, absolute and relative wear resistance.
2. The greater wear of dense pure aluminum is due to the action of a mechanism of intense plastic deformation during dry abrasion at the larger contact area of friction.
3. The presence of pores leads to a discrete nature of the process of plastic deformation and, accordingly, less wear.
4. It can be seen that the wear resistance of the dense and porous alloys is higher than the wear resistance of pure aluminum.

6 . References

1. Velikov A., B. Krastev, R. Dimitrova, V. Petkov, S. Stanev, V. Manolov. Development of technology for obtaining of porous castings from aluminum and aluminum A356 alloy. V, 2/12, VI INTERNAZIONAL SCIENTIFIC CONFERENCE – WINTER SESSION INDUSTRY 4.0. V, Volume 2/12, 2021, ISSN: ISSN (Print) -2535-0153, ISSN (Online)-2535-0161, 178-180.
2. Bhavik Ajaykumar Mehta. Mechanical and Tribological Properties of Aluminium Matrix Syntactic Foams Manufactured with Recycled Aluminium Smelter Waste .University of Liverpool for the Degree of Doctor in Philosophy. June 2020.
3. Prakash Manoharan, Milon Dennison, Karuppasamy Ramasamy, Balakumar. Wear Test on Aluminum Foam Prepared from Aluminum (LM0) as Base Metal and Dolomite (CaMg (Co3)2) as Foaming Agent, Coimbatore-641021, INDIA. International Research Journal of Engineering and Technology.March 2018.

The work is supported by a project under contract №. КП-06-Н47/12 / dated 03.12.2020, financed by the Fund “Scientific Research”, Republic of Bulgaria. Part of the equipment used in this work was financed by the European Regional Development Fund within the OP "Science and Education for Intelligent Growth 2014 - 2020", CE project "National Center for Mechatronics and Clean Technologies", № BG05M2OP001-1.001-0008-C08

Synthesis and characterization of 2D $NbSe_2$

Dimitre Dimitrov[1,2*], Vera Marinova[2], Irnik Dionisiev[2]
Institute of Solid State Physics, Bulgarian Academy of Sciences, 72 "Tzarigradsko Chaussee" Blvd, 1784 Sofia, Bulgaria[1]
Institute of Optical Materials and Technologies, Bulgarian Academy of Sciences, Bl.109 "Acad. G. Bonchev Str., 1113 Sofia, Bulgaria[2]
dzdimitrov@issp.bas.bg

Abstract: *Two-dimensional van der Waals (vdW) materials possess novel physical properties and promising applications. A wide range of 2D vdW materials having been obtained via the chemical vapor transport (CVT) method. In this work, we develop the controllable growth meyhod of 2H-$NbSe_2$ single crystals via the CVT method. The quality of fabricated crystals was characterized by X-ray diffraction, and electron dispersive spectrometry (EDS) measurements. Crystals of the best quality were successfully grown under selected temperature/time schedule.*

Keywords*: TDMC, CVT (CHEMICAL VAPOR TRANSPORT), NBSE2, SINGLE CRYSTAL, STRUCTURE*

1. Introduction

In recent years, interest in the synthesis and applications of transition metal dichalcogenides MX_2 (M: Mo, W, X = S, Se, Te) nanomaterials has steadily grown because of their unique structure and superior properties [1]. Transition metal dichalcogenides have a sandwich interlayer structure formed by the stacking of the X–M–X layers, which are loosely bound to each other only by van der Waals forces and are easily cleaved. Moreover, MX_2 exhibits unique physical, optical and electrical properties correlated with their layered structure. In addition, their electronic structure is such that band-edge excitation corresponds largely to a metal centered d-d transition. Owing to these features, TMDCs materials have numerous applications such as sensors, detectors, solid lubricants, catalysis, electrocatalysis, high-density batteries and optoelectronic devices [2].

Niobium diselenide ($NbSe_2$) is transition metal dichalcogenide layered compound, and it is exceptionally attractive because of its super conductivity and the formation of a charge-density-wave (CDW) state [3]. 2H-phase niobium diselenide (2H-$NbSe_2$) is a superconducting vdW (Van der Waals) crystal with charge density wave (CDW) and Weyl semimetal properties. It has a superconducting critical temperature of ~7.8K and charge density wave behavior at ~34K. It has layered structure (lamellar) with weak interlayer coupling. $NbSe_2$ displays metallic and superconducting behavior.

2. Experimental details

Chemical vapour transport (CVT), a technique / process where a condensed phase, typically a solid is volatilized in the presence of a gaseous reactant (transport agent) and deposited elsewhere in the form of crystals. Typical transport agents include halogens and halogen compounds. The setup consists of a 2-zone furnace, the reactant and transport agent sealed in an ampoule. The various parameters that must be optimized for a successful CVT are growth temperature, transport direction, rate of the mass transport, choice of the transport agent and the free energy of the reaction.

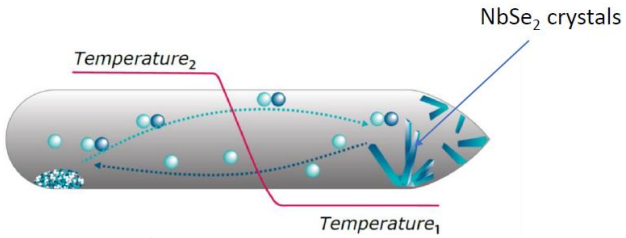

Fig. 1 *Schematic of the experimental setup.*

Single crystals of $NbSe_2$ were grown by a chemical vapour transport technique using iodine as transporting agent. A 5 gm mixture of Nb (purity: 99.95 %, Alfa Aeser, Germany) and Se (purity: 99.99 %, Alfa Aeser, Germany) was filled in a dried ampoule. Iodine of the quantity 5-6 mg/cc of the ampoule volume was sealed in the thin capillary and placed in the ampoule as transporting agent. Then the ampoule was sealed at the pressure of 10^{-5} torr. The sealed ampoule was introduced into a two-zone furnace at constant reaction temperatures to obtain the charge of $NbSe_2$. The charge so prepared was rigorously shaken to ensure proper mixing of the constituents and kept in the furnace again, under appropriate condition to obtain single crystals of $NbSe_2$. The experimental conditions for crystals growth are shown in Table 1.

Table 1: *Growth parameters for $NbSe_2$ single crystals using chemical vapor transport technique.*

	Length (mm)	ID (mm)
Ampoule dimensions	300	25
	Hot zone (K)	Cold zone (K)
Temperatures	1123	1053
	Time (hours)	
Growth time	240	

Powder X-ray diffraction (XRD) patterns were gathered within the 2Θ range from 20 to 80° with a constant step 0.02° on a Bruker D8 Advance diffractometer with a Cu Kα radiation and LynxEye detector. Phase identification was performed with the Diffracplus EVA using the ICDD-PDF2 Database.

3. Results and discussions

$NbSe_2$ is Molybdenite-like structured and crystallizes in the hexagonal $P6_3$ /mmc space group. The structure is two-dimensional and consists of two $NbSe_2$ sheets oriented in the (0, 0, 1) direction. Nb^{4+} is bonded to six equivalent Se^{2-} atoms to form distorted edge-sharing $NbSe_6$ pentagonal pyramids. All Nb–Se bond lengths are 2.62 Å. Se^{2-} is bonded in a 3-coordinate geometry to three equivalent Nb^{4+} atoms.

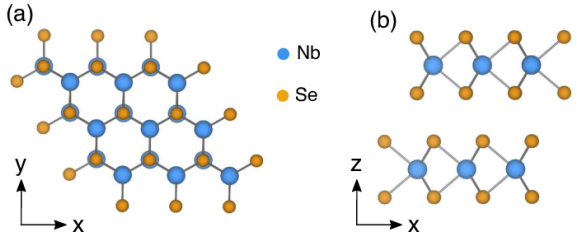

Fig.2 *(a) Crystal structure of bulk $NbSe_2$ illustrating the (a) top view and (b) side view of the structure. The x, y and z axes denote the cartesian axes*

Many methods have been developed to improve the crystalline quality of superconducting $NbSe_2$, for example: (a) exfoliation from bulk single-crystal $NbSe_2$ by the electrochemical exfoliation method [4]; (b) growth by salt-assisted CVD [5]; (c) growth by molecular beam epitaxy (MBE) under ultra-high vacuum [6]; and (d) growth of a wafer-scale $NbSe_2$ film in oxygen-free conditions by a two-step vapor deposition method [7]. However, most of the above preparations of $NbSe_2$ have either a lot of point defects or a small grain size, which reduces its environmental stability or Tc. Therefore, it is still challenging to develop a reliable strategy to

grow 2D $NbSe_2$ with a large area, high crystalline quality, and high repeatability.

The CVT single crystals growth was chosen due to the advantages of bulk single crystals as large crystals to measure basic properties: structural, optical, electrical; nearly-perfect state of material: purity, no grain boundaries, less structural defects, stress, etc. The tunability of bulk properties: control of phase stoichiometry, doping level, alloy composition is readily obtained. The layered crystals as $NbSe_2$ are easily of exfoliation and stacking of heterostructures. In the CVT process, metallic niobium (Nb) and selenium (Se) are mixed together with a small amount of a halogen gas in a sealed quartz tube. The mixture is heated to high temperatures, typically between 800-1100°C, causing the halogen gas to vaporize and transport the Se from the hot zone to a cooler region in the tube. The Se reacts with the Nb to form $NbSe_2$, which deposits on a cooler surface in the tube. The halogen gas also plays a crucial role in preventing the formation of impurities and defects in the $NbSe_2$ crystal.

The overall reaction can be written as:

$$Nb + Se + X_2\ (X=Br \text{ or } I) \rightarrow NbSe_2 + X_2\ (transport) \qquad (1)$$

The use of halogen gas as a transport agent in CVT synthesis allows for the growth of high-quality, single crystals of NbSe2 with controlled stoichiometry and low defect density.

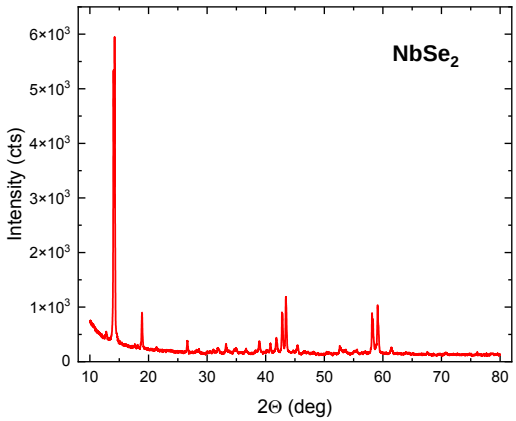

Fig.3 *XRD patterns of $NbSe_2$ single crystal*

The crystallinity, structure, and phase purity of the prepared samples were confirmed by XRD and EDS. As shown in Fig. 1a, all observed diffraction peaks can be exactly indexed to the hexagonal phase of $NbSe_2$ with lattice constants a = 3.445 Å and c = 12.55 Å (PDF No. 65-7464). No characteristic peaks were observed, and the sharp diffraction peaks imply a good crystallinity of the obtained $NbSe_2$ products under current synthesis conditions. The Energy-dispersive X-ray Spectrometry (EDS) result demonstrates that the samples are consisted of elements Nb and Se, while no other elements were observed. Photoluminescence spectra are presented at Fig.4. Broad response around 2.5 eV was observed.

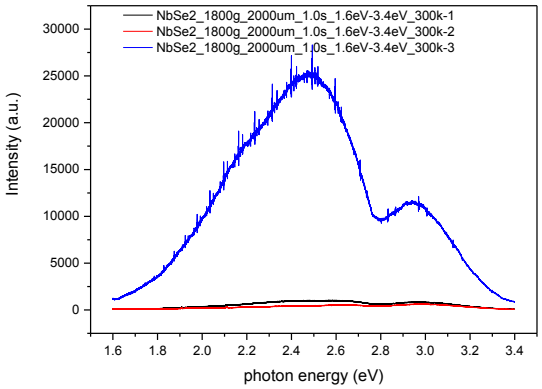

Fig.4 *Photoluminescence spectra of $NbSe_2$*

4. Acknowledgements

We are grateful for the financial support from Bulgarian Science Fund project number КП-06-КОСТ/13 and COST Action CA17123 - Ultrafast opto-magneto-electronics for non-dissipative information technology (MAGNETOFON)

5. References

1. S. Manzeli, D. Ovchinnikov, D. Pasquier, O. V. Yazyev & A. Kis, Nature Reviews Materials, volume 2, article number: 17033 (2017)
2. A. A. Tedstone, D. J. Lewis, and P. O'Brien, Chem. Mater., 28, 7, 1965–1974 (2016)
3. Z. Li, X. Xi, B. Ding, H. Li, E. Liu, Yuan Yao, and W. Wang, Cryst. Growth Des., 20, 2, 706–712 (2020)
4. Z. Zeng, T. Sun, J. Zhu, X. Huang, Z. Yin, G. Lu, Z. Fan, Q. Yan, H.H. Hung, H. Zhang, Angew. Chem. Int. Ed., 51, 9052–9056 (2012)
5. H. Wang, X. Huang, Lin, J.; Cui, J.; Chen, Y.; Zhu, C.; Liu, F.; Zeng, Q.; Zhou, J.; Yu, P., Nat. Commun., 8, 394 (2017)
6. T. Hotta, T. Tokuda, S. Zhao, K. Watanabe, T. Taniguchi, H. Shinohara, R. Kitaura, Appl. Phys. Lett., 109, 133101 (2016)
7. H. Lin, Q. Zhu, D. Shu, D. Lin, Xu, J.; Huang, X.; Shi, W.; Xi, X.; J. Wang, L. Gao, Nat. Mater., 18, 602–607 (2019)

Studying the composition and properties of white eco-cement

Lev Chernyak [1], Nataliia Dorogan [2], Liubov Melnyk [3], Petro Varshavets.[4], Victoria Pakhomova [5]
National Technical University of Ukraine" Igor Sikorsky Kyiv Polytechnic Institute"
Kyiv, Ukraine
lpchernyak@ukr.net

Abstract: *The possibility to produce white Eco-cement with the use of a dry method under low-temperature firing of a raw material mixture based on the CaO – SiO2 – Al_2O_3 – MgO system is shown. Computer calculations were performed and an analysis of the dependence of the characteristics of cement clinker on the quantitative ratio of raw components was carried out. A new composition of the raw material mixture with a decrease of 19 wt. % amount of the carbonate component and, accordingly, CO_2 emissions during combustion was determined. The peculiarities of phase transformations in the material during firing with a maximum temperature of 1100 °C when microtalcum was introduced into the initial mixture with the formation of pericloze, ockermanite and merwinite as a factor in the structure and properties of cement clinker were noted.*

Keywords*: ECO-CEMENT,RAW MATERIAL MIXTURE, MICROTALC, FIRING, PHASE COMPOSITION, PROPERTIES.*

1. Introduction

The production of the most common mineral binder, Portland cement, is characterized by significant energy costs by high-temperature firing (1400-1500 °C) of clinker as well as by its grinding with additives to a highly dispersed state [1-3]. At the same time, the physical and chemical transformations of rock-forming minerals into carbonate components, which make up the majority (75-80 wt. %) of the composition of the raw material mixtures, cause significant emissions of CO_2 into the atmosphere [4].

It is noted that cement clinker kilns account for about 5% of total CO_2 emissions into the atmosphere. The problem lies in cement's chemistry, which is a sort of double-whammy of CO_2 production. To turn Portland cement's key ingredient, calcium carbonate—found in limestone or chalk—into a finished product called alite, the minerals must be broken down in kilns heated to more than 1400 ºC. The heating process uses tremendous amounts of energy, which is typically generated using gas or coal, the most carbon-intensive fossil fuel. Then, the ensuing chemical process releases a second wallop of CO_2 as a byproduct of turning calcium carbonate into calcium oxide. In total, producing 1 ton of cement releases 770 kilograms of CO_2 into the atmosphere.

When solving the specified problems of resource conservation and environmental safety of cement production, considerable attention is given to the Eco-cement technology using raw material mixtures with a lower content of carbonate components [5-8] and the use of industrial waste [9,10].

The production of white Eco-cement is complicated by special requirements regarding the chemical composition of raw materials with the minimization of the content of colored oxides [11-13]. The solution of this scientific and technical problem requires the development of new compositions of raw material mixtures, the analysis of the features of phase formation and the properties of white hydraulic mineral binder under the conditions of low-temperature firing, which became the goal of the presented work.

2. Results and discussion

The selection of research objects in this work was carried out in accordance with the main goal – to obtain a white mineral binding material during low-temperature firing with a decrease in the content of the carbonate component in the initial mixture. In accordance with the above, raw materials must have:

- increased reactivity, ensuring the intensification of physical and chemical reactions in the silicate system during firing with a decrease in the maximum temperature;
- minimum content of color oxides to increase the degree of whiteness of the final product.

Materials of natural and industrial origin were used for the production of the raw material mixture:

- chalk of the Zdolbuniv deposit of the Rivne region;
- aluminum hydroxide – a product of processing bauxite into alumina;
- pyloquartz - a product of enrichment and fractionation of quartz sand;
- microtalc – a product of enrichment and fractionation of talc powder.

According to the chemical composition, among the studied raw materials, the sample of Zdolbuniv chalk is characterized by a high content of CaO, the sample of aluminum hydroxide - the largest amount of aluminum oxide, the sample of pyloquartz - the largest amount of silica, the sample of microtalc - a high content of magnesium oxide with a quantitative ratio of SiO_2:CaO:MgO = 11:1: 5 (Table 1).

The raw mixtures have been prepared by dispensing the components by mass, mixing and homogenizing in a ball mill, firing and milling of the final product in accordance with the modern dry technology of cement production.

Table 1: *Chemical composition of raw materials*

Samples	Content of oxides, wt. %									
	SiO_2	Al_2O_3	Fe_2O_3	TiO_2	CaO	MgO	SO_3	Na_2O	K_2O	LOI
chalk	0,77	0,25	0,13	-	55,0	0,25	0,08	-	-	43,49
hydrate of aluminium oxide	-	65,0	-	-	-	-	-	-	-	35,0
pyloquartz	99,16	0,16	0,06	-	-	-	-	-	-	0,12
microtalc	61,32	0,26	0,10	-	5,39	27,40	-	-	-	5,53

The samples were fired for 15 hours at a maximum temperature of 1100 °C with a holding time of 1.5 hours. All samples of the mixtures compared were fired simultaneously and together to exclude differences in the degree of heat treatment.

The properties of the binding material were determined according to standardized methods.

Methods of physical - chemical analysis of silicate raw materials and testing of properties of astringent substances which were used in this work included:

- chemical composition analysis using standardized procedures;
- X-ray diffraction analysis (powder - like preparations) using a diffractometer DRON-3M (radiation CuKα 1-2, voltage 40 kV, current 20 mA, speed 2 degrees/min);

- determination of the whiteness of materials using a leukometer Carl Zeiss JENA.

The analysis of mineralogical composition of raw material showed:

- the basic rock-forming mineral of chalk is calcite (97,6 mass.%) with the admixtures of dolomite, quartz and kaolinite;
- hydrate of aluminium oxide is characterized by the presence of hydrargillite (gibbsite), diaspore, boehmite with the insignificant admixture of ilmenite;
- the main rock-forming mineral of pyloquartz is β-quartz;
- the main rock-forming mineral of microtalc is talc with quartz impurities.

It is obvious that by the calcination of the specified raw materials during the destruction of lattices of the main rock-forming minerals, chalk and aluminum hydroxide will become a source of CaO and Al_2O_3 oxides, pyloquartz - a source of SiO_2, and microtalc - SiO_2 and MgO oxides in the process of phase formation of cement clinker [14-16].

Results and Discussion

The composition of the initial 3-component raw material mixtures basedon the chalk-aluminum hydroxide- pyloquartz and chalk-aluminum hydroxide-microtalc systems was determined according to known recommendations regarding low-temperature firing cement technology in the range of values of the hydraulic modulus HM=1.1–1.7 using a specially created program for computer calculations [17].

It was established that in the specified HM interval, the quantitative ratio of the system components changes significantly, while along with the dependence of the concentration of the components on the hydraulic modulus, a significant change in the values of the silica modulus is observed.

It was determined that at the minimum aluminum hydroxide concentration for the studied systems of 10 wt. % in the range of values of HM=1.1-1.7, the possible content of the carbonate component is 68.3-73.5 wt. % when using pyloquartz and 54.5-62.8 wt. % when using a microtad (Fig. 1). At the same time, there is a directly proportional relationship between the concentration of the carbonate component and the values of the hydraulic modulus of the binder.

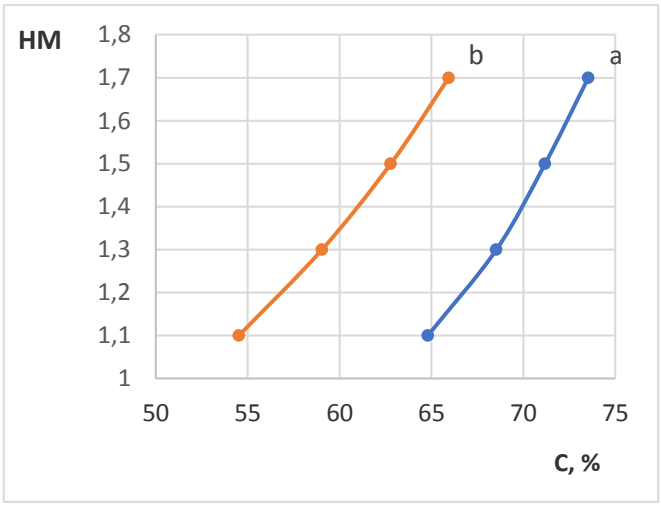

1

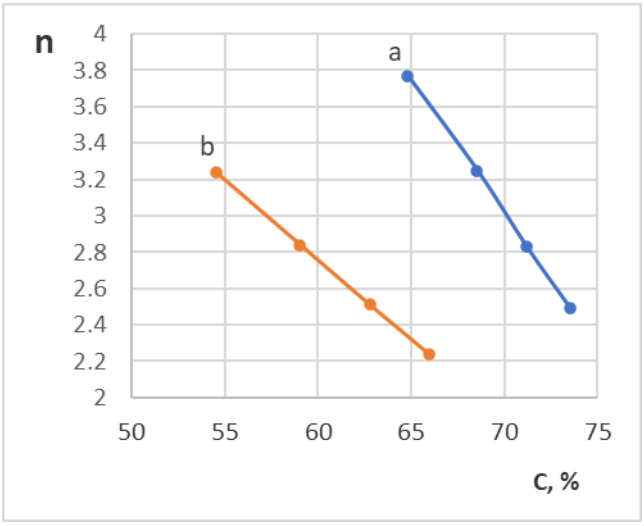

2

Fig. 1 *Dependence of the hydraulic (1) and silica (2) moduli on the concentration of the carbonate component when using pyloquartz (a) and microtalc (b)*

As for the cement modulus n of the binder, there is an inversely proportional dependence of its values on the concentration of the carbonate component: in the ranges of 2.5-3.8 for systems with pyloquartz and 2.2-3.2 for systems with microtalc.

The raw material mixtures chosen for the production of mineral binding material with the same amount of aluminum hydroxide differ significantly in the content of the carbonate component - chalk (Table 2).

Table 2**:** *Composition of raw mixtures*

Code of mixture	Quantity of components, mass %			
	chalk	hydrate of aluminium oxide	pyloquartz	microtalc
K9	73,5	10,0	16,5	-
K12	54,5	10,0	-	35,5

According to the chemical composition, the investigated raw material mixtures are characterized by the same amount of aluminum and iron oxides, but they differ significantly in the content and quantitative ratios of other oxides, which determine a potential for phase formation during firing (Table 3).

Table 3: *Chemical composition of raw mixtures*

Sample code	Content of oxides, wt. %						
	SiO_2	Al_2O_3	Fe_2O_3	CaO	MgO	SO_3	LOI.
K9	16,99	6,71	0,11	40,45	0,18	0,06	35,50
K12	22,18	6,73	0,11	31,91	9,86	0,04	29,17

Thus sample K12 differs from K9 by:

• a smaller amount of calcium oxides, a much higher content of magnesium oxide with a quantitative ratio of CaO : MgO = 3.2;

• quantitative ratios of CaO : SiO_2 = 1.4 versus 2.4 and CaO : $A_{l2}O_3$ = 4.7 versus 6.0.

The analysis of the chemical composition of cement clinker from experimental mixtures (Table 4) indicates that at low values of the saturation coefficient SF= 0.35-0.64, the formation of crystalline phases C_2S and C_3A is most likely when the amount of iron-containing compounds is minimized.

Table 4: *Chemical composition of clinker*

Sample code	Content of oxides, wt. %					
	SiO_2	Al_2O_3	Fe_2O_3	CaO	MgO	SO_3
K9	26,34	10,40	0,17	62,72	0,28	0,09
K12	31,31	9,51	0,15	45,03	13,92	0,06

The results of the X-ray phase analysis obtained in this work indicate on certain peculiarities in the physical and chemical transformations during firing of the studied mixtures with a maximum temperature of 1100 °C (Fig. 2, 3).

Thus, after firing to the maximum temperature of 1100 °C with approximately the same development of the C_2S and CA crystalline phases, sample K12 differs from sample K9 by:

- a significantly smaller amount of free CaO (1.69; 2.38 Å) and quartz (3.835; 4.25 Å);
- formation of periclase (2.10; 1.48 Å), ockermanite $2CaO•MgO•2SiO_2$ (2.87 Å) and merwinite $3CaO•MgO•2SiO_2$ (2.66 Å);
- greater development of C_2AS hellenite (2.86 Å);
- a smaller groove of the crystalline phases of wollastonite CS (2.97; 3.48 Å) and mayenite $C_{12}A_7$ (4.90 Å).

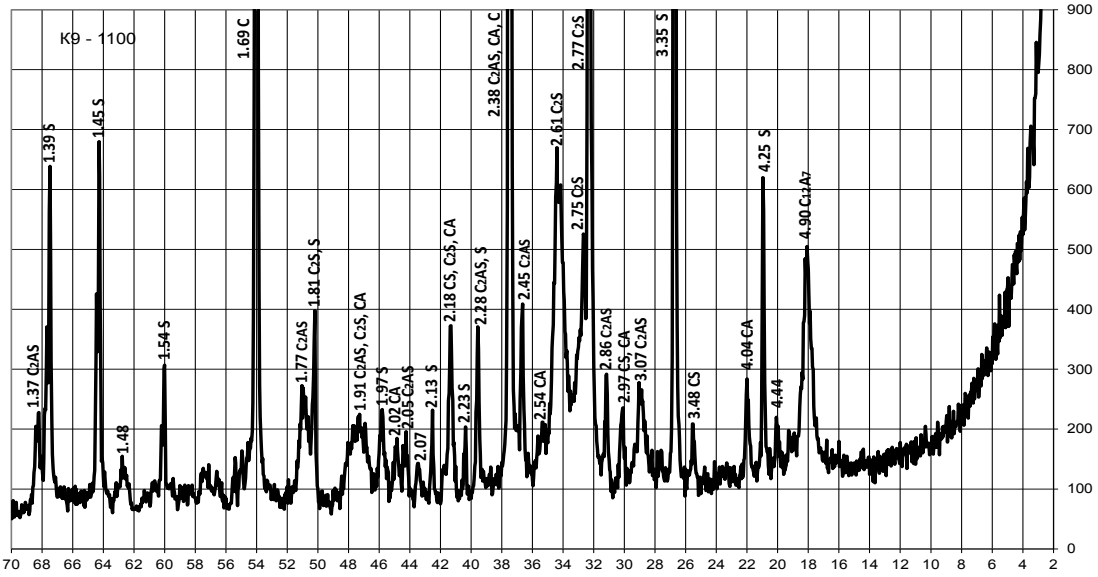

Fig. 2 *X-ray diffraction of sample K9 (1100 ºC).*

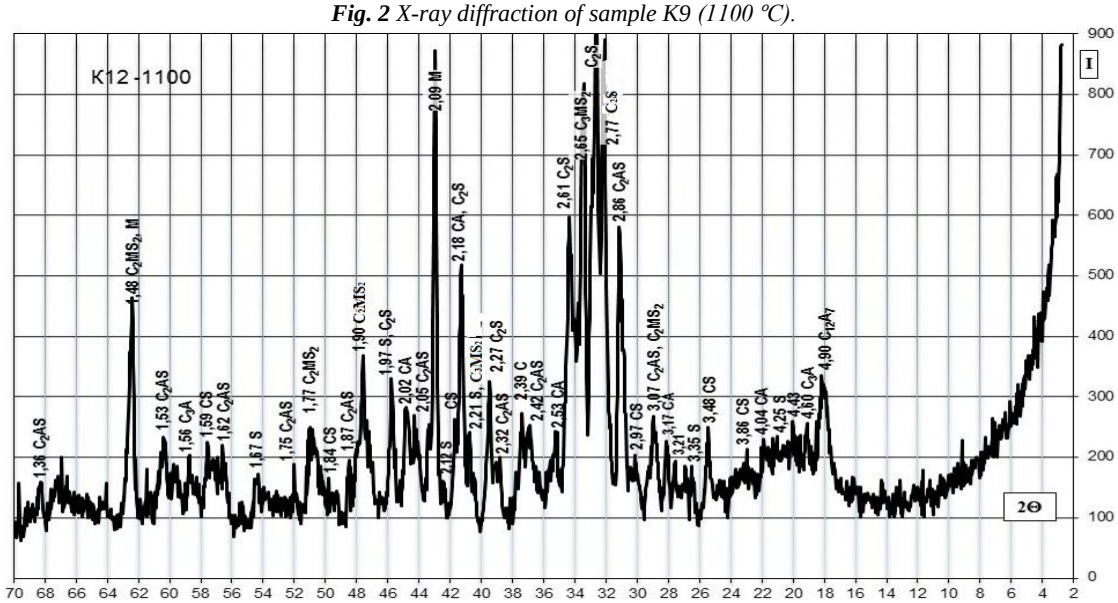

Fig. 3 *X-ray diffraction of sample K12 (1100 ºC).*

The results of the testing of the studied samples of the binder indicate differences in the influence of the composition on the property indicators (Table 5). Thus, according to the classification of DSTU B V.27-91-99 [18], when fired at a maximum temperature of 1100 °C, the binder from the K9 mixture belongs to the group of ultra-fast hardeners (starting time no later than 15 min.), which is considered typical for expanding and tensioning cement. The sample K12 belongs to a fast-hardening one (time of onset from 15 to 45 min.), which is considered typical for anhydrite and alumina cement. At the same time, the sample K12 differs from K9 in the general slowing down of the hardening process.

Table 5: *Properties of mineral astringent material*

Characteristics	Sample code	
	K9	K12
Finess of grinding, sieve residue no. 008, mass. %	7	7
Initial setting time, min	10	30
Final setting time, min	25	60
Compressive strength, MPa	32	34,5
Whiteness, %	88	90

According to the specified standard, the samples of the binder produced belong to the group of medium strength (from 30 to 50 MPa per compression). From the point of view of the purpose of this work, it is important to achieve high whiteness indicators in accordance with the requirements of the standard for white Portland cement [19,20].

Conclusions

1. The development and practical use of mineral binders of the Eco-cement type with a reduction in the content of the carbonate component of the raw material mixture contributes to the comprehensive solution of the issues of ecology, resource conservation and chemical technology for the production of silicate materials.

2. The possibility of producing white Eco-cement by a dry method at a maximum firing temperature of 1100 °C based on the chalk-aluminum hydroxide-microtalc system with a decrease in the content of the carbonate component and, accordingly, CO_2 emissions into the atmosphere by 19-20% compared to known compositions, was determined:

3. The peculiarities of phase formation during low-temperature firing of white Eco-cement clinker, manifested in the formation of crystalline phases of periclase and calcium-magnesium silicates - ockermanite $2CaO•MgO•2SiO_2$ and mervinite $3CaO•MgO•2SiO_2$, were established.

Here are some examples:

1. Duda W. Cement Data Book, Volume 3: Raw Material for Cement Production - French & European Pubns, 1988. – 188 p.
2.Ghosh S. Advances in Cement Technology: Chemistry, Manufacture and Testing / Taylor & Francis, 2003. – 828 p.
3.Anjan K. Cement Production Technology. Principles and Practice // CRC Press, 2018. – 439 p.
4. Andrew R. Research, CICERO Center for International Climate. Global CO_2 emissions from cement production // Journal of Earth Syst. Sci. Data (2017)
5. Hanehara S. ECO-CEMENT AND ECO-CONCRETE Environmentally Compatible Cement and Concrete Technology // Conference: JCI/KCI International Joint Seminar, 2001. – Vol.1.
6. Scrivener K. Eco-efficient cements: Potential economically viable solutions for a low-CO_2 cement-based materials industry // Cement and Concrete Researchl, 2018. – Vol. 114. – p. 2-26, (Scrivener K., Vanderley M., Gartner E.).
7. Schneider M. The cement industry on the way to a low-carbon future // Cement and Concrete Research, 2019. – Vol. 124(3).
8. Low Carbon Cement Production Issue Paper // https://www.climateactionreserve.org/wp-content/uploads/2022/10/Low-Carbon-Cement-Issue-Paper-05-20-2022_final.pdf
9. Uchikawa H. Eco-cement-frontier of Recycling of Urban Composite Waste, World Cement, 1995, pp. 33-36, (Uchikawa H., Obana H.).
10. Shimoda T. Eco-cement: A New Portland Cement to Solve Municipal and Industrial Waste Problems, Modern Concrete Materials, Proceedings of the International Conference 'Creating with Concrete', Dundee(UK), 1999, pp. 17-30, (Shimoda T., Yokoyama S.).
11. Zubekhin A. White Portland Cement // Rostov on/D,: Universitet, 2004. – 263 p., (Zubekhin A., Golovanova S., Kirsanov P.).
12. Moresová K. White cement - Properties, manufacture, prospects // Ceramics Silikaty, 2001. – Vol. 45(4). – pp.158-163, (Moresová K., Škvára F.).
13. Dorogan N. White Portland Cement – Kyiv: «Polytechnica», 2018. – 204 p., (Dorogan N., Sviderskyy V., Chernyak L.).
14. Taylor H. Cement Chemistry – London: Thomas Telford Publishing; 2 edition, 1997 – 459 p.
15. Bogye R. The Chemistry of Portland cement. – New York: 1995. – 326 p.
16. Kurdowski W. Chemia cement - Warzawa: PWN, 1991. – 478 s.
17. Sviderskyy V. The software for technology of low-temperature binder materials // Bulding materials and products, 2017. - № 1-2 (93). – P. 22 – 24., (Sviderskyy V., Chernyak L., Sanginova O., Dorogan N., Tsybenko M.).
18.DSTU B V.2.7-91-99. Astringent mineral. Classification.– K.: Cerzhbud of Ukraine,1999.
19.DSTU B V.2.7-257:2011. White Portland Cement. Technical Date. – K.: Minregion of Ukraine,2012.
20. ASTM C150-07. Standard Specification for Portland Cement.